

# AGN

National Aeronautics and Space Administration  
George C. Marshall Space Flight Center

METEOROID IMPACT SIMULATION

BY

MAGNETIC GRADIENT PARTICLE ACCELERATION TECHNIQUES

Final Technical Report  
NAS 8-11174

AN-1490

May 1966

GPO PRICE \$ \_\_\_\_\_  
CFSTI PRICE(S) \$ \$3.00  
Hard copy (HC) 1.50  
Microfiche (MF) \_\_\_\_\_  
ff 653 July 65

N66 26875  
(ACCESSION NUMBER)  
156  
(PAGES)  
CR-75284  
(NASA CR OR TMX OR AD NUMBER)  
(THRU)  
(CODE)  
32  
(CATEGORY)



METEOROID IMPACT SIMULATION  
BY  
MAGNETIC GRADIENT PARTICLE ACCELERATION TECHNIQUES

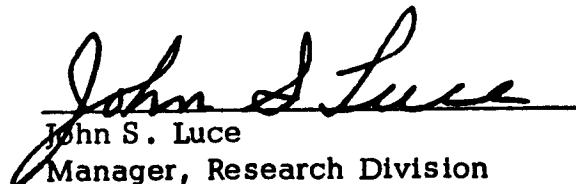
Contract NAS 8-11174

George C. Marshall Space Flight Center  
National Aeronautics and Space Administration  
Huntsville, Alabama

FINAL TECHNICAL REPORT  
1 July 1964 through 15 April 1966

Robert L. Chapman

Reviewed and Approved:

  
John S. Luce  
Manager, Research Division

## TABLE OF CONTENTS

	<u>Page</u>
I. <u>OBJECTIVE</u>	1
II. <u>SUMMARY</u>	2
III. <u>THEORY</u>	5
A. MAGNETIC FIELD DIFFUSION INTO THE PROJECTILE AND PROJECTILE HEATING	5
1. Introduction	5
2. Linear Analysis	6
a. General Considerations	6
b. Magnetic Diffusion into a Sphere	9
c. Ohmic Heating Due to Magnetic Diffusion	19
d. The Numerical Solution of the Magnetic Diffusion into a Sphere	26
e. Results and Conclusions	32
3. Non-Linear Analysis	33
a. Statement of Problem	33
b. Method of Calculation	34
c. Results	39
4. Correction for High Magnetic Field Effects	39
a. Description	39
b. Results	46

TABLE OF CONTENTS  
(Continued)

	<u>Page</u>
B. FLUX CONCENTRATOR HYDRODYNAMICS	55
1. Introduction	55
2. Statement of Problem	55
3. Method of Calculation	55
4. Results	64
IV. <u>REDESIGN AND IMPROVEMENT OF</u> <u>SYSTEM PERFORMANCE</u>	78
A. EXPLOSIVE SYSTEM	78
1. Multiple Detonator Initiation System	78
2. Armature Considerations	83
3. End Confinement of the Main Explosive Charge	83
B. MAGNETIC FIELD SYSTEM	86
1. Capacitor Bank Magnet System	86
2. Attractive Coil Motion	92
V. <u>SPECIAL INSTRUMENTATION</u>	94
A. FLASH X-RAY	94
B. PROJECTILE FLIGHT CHAMBER	95
C. INTERNAL PROJECTILE OBSERVATION	95



TABLE OF CONTENTS  
(Continued)

	<u>Page</u>
VI. <u>EXPERIMENTS</u>	101
A. PERIPHERAL TESTS	101
1. End Plate Confinement	101
2. Detonator Firing Simultaneity	102
3. Shaped Charge Jets	102
4. Fast-Acting Shutter	107
B. MGA DEVICE DEVELOPMENT	108
1. Description of Test Device	110
2. Description of Experiments	110
3. Conclusions	113
C. PROJECTILE EXPERIMENTS	116
1. Description of Test Devices	116
2. Discussion of Experiments	121
a. Flight Chamber Experiments	123
b. Projectile Observation Experiments	132
c. Conclusions	143
VII. <u>CONCLUSION</u>	145

## LIST OF ILLUSTRATIONS

	<u>Page</u>
1. Simulated Drive Field for Diffusion and Heating Calculations (applied in outer computation zone)	40
2. Magnetic Field Diffusion into 1-mm Diameter Aluminum Cylinder, $\eta = a + bT$	41
3. Magnetic Field Diffusion into 2-mm Diameter Aluminum Cylinder, $\eta = a + bT$	42
4. Magnetic Heating of 1-mm Diameter Aluminum Cylinder, $\eta = a + bT$	43
5. Magnetic Heating of 2-mm Diameter Aluminum Cylinder, $\eta = a + bT$	44
6. Magnetic Field Diffusion into 1.5-mm Diameter Aluminum Cylinder, $\eta = a + bT$	47
7. Magnetic Field Diffusion into 1.5-mm Diameter Aluminum Cylinder, $\eta = a + (b/33) T$	48
8. Magnetic Field Diffusion into 1.5-mm Diameter Aluminum Cylinder, $\eta = a + bT/1 + 32B$	49
9. Magnetic Field Diffusion into 1.5-mm Diameter Aluminum Cylinder, $\eta = a + bT/1 + 32B^2$	50
10. Magnetic Heating of 1.5-mm Diameter Aluminum Cylinder, $\eta = a + bT$	51
11. Magnetic Heating of 1.5-mm Diameter Aluminum Cylinder, $\eta = a + (b/33) T$	52
12. Magnetic Heating of 1.5-mm Diameter Aluminum Cylinder, $\eta = a + bT/1 + 32B$	53
13. Magnetic Heating of 1.5-mm Diameter Aluminum Cylinder, $\eta = a + bT/1 + 32B^2$	54
14. Configuration for Flux Concentrator Hydrodynamic Calculations	56

LIST OF ILLUSTRATIONS  
(Continued)

	<u>Page</u>
15. Flux Concentrator Inner and Outer Radii vs Time, Cases 1, 2, 3	65
16. Flux Concentrator Inner and Outer Radii vs Time, Cases 4, 5, 6	66
17. Flux Concentrator Inner and Outer Radii vs Time, Cases 7, 8, 9	67
18. Flux Concentrator Inner and Outer Radii vs Time, Cases 10, 11, 12	68
19. Magnetic Field Strength vs Time, Cases 1, 2, 3,	69
20. Magnetic Field Strength vs Time, Cases 4, 5, 6	70
21. Magnetic Field Strength vs Time, Cases 7, 8, 9	71
22. Magnetic Field Strength vs Time, Cases 10, 11, 12	72
23. Magnetic Field Strength vs Time at End of Compression, Cases 1, 2, 3	73
24. Magnetic Field Strength vs Time at End of Compression, Cases 4, 5, 6	74
25. Magnetic Field Strength vs Time at End of Compression, Cases 7, 8, 9	75
26. Magnetic Field Strength vs Time at End of Compression, Cases 10, 11, 12	76
27. Multiple Detonator Firing System--Slave Unit	81
28. Schematic Diagram of Multiple Detonator Firing System	82
29. Explosive End Confinement Test Results	85
30. Characteristics of Capacitor-Driven Magnets for Initial Magnetic Field Production	88

LIST OF ILLUSTRATIONS  
(Continued)

	<u>Page</u>
31. Cross Section of Capacitor Driven Coil	91
32. Chamber for External Projectile Diagnostics	96
33. Optical Arrangement for Observing Projectile During Magnetic Compression	98
34. Shaped Charge Construction	104
35. Selected Frames from Shaped Charge Jet Test of Projectile Flight Chamber and Lucite Target Block (1 $\mu$ sec/frame)	106
36. Fast-Acting Blast Shutter	109
37. General Details of Test Device for Development Experiments	111
38. MGA Instrumented for Design Performance Experiment	114
39. Circular Symmetry of Detonation, Shot MGA-11	115
40. Final Design of MGA as Used in Direct Projectile Observation Experiments	118
41. Details of Flux Concentrators	119
42. Completed Segments of 5-cm Long, Double-Ended Short Inside Taper Flux Concentrator, and Search Coil	120
43. Magnetic Field Measurements from Shot MGA-15	125
44. Selected Frames from Shot MGA-18, Interframe Time 1 $\mu$ sec	128
45. Selected Frames from Shot MGA-20, Interframe Time 1 $\mu$ sec	130
46. Schematic Diagram of Direct Projectile Observation Experiments	133
47. Selected Frames from Internal Projectile Observation Experiment, MGA-28. Interframe Time 0.5 $\mu$ sec	135
48. Framing Camera Sequence from Shot MGA-29, Inter- frame Time 0.3 $\mu$ sec	138

## LIST OF TABLES

	<u>Page</u>
I Equation of State Constants	62
II Parameters and Materials	63
III Detonator Time Variation with Standard 200-Joule Firing Unit	79
IV Computed Attractive Forces Between the MGA Magnet Coils	92
V Explosive End Confinement Tests	102
VI Multiple Detonator Simultaneity Tests	103
VII Shaped Charge Jet Tests	105
VIII Fast Acting Shutter Tests	108
IX MGA Device Development Experiments	112
X MGA Projectile Experiments	122

## I. OBJECTIVE

The objective of this program was to determine the feasibility of using strong magnetic field gradients to accelerate small metallic projectiles to velocities suitable for simulating micrometeoroid impacts. The ultimate goal of the program was to develop a laboratory material testing tool that can impart to discrete particles of known size, shape and mass, velocities of approximately 30 km/sec (which corresponds to the velocities of micrometeoroids encountered by space vehicles).

## II. SUMMARY

The Magnetic Gradient Accelerator (MGA)<sup>1</sup> is a device for accelerating small metallic projectiles to hypervelocities. The acceleration arises from the force of the strong magnetic field gradient on a diamagnetic sphere. The strong field is produced by explosively compressing an initial magnetic field to megagauss values.

This report concerns the second contract supporting this program. The first, NAS8-5266, was a preliminary feasibility study. During that contract the basic acceleration theory was worked out and experiments were conducted to test the applicability of explosive magnetic field compression to this problem. The results of the initial feasibility study indicated that a metallic vapor was being ejected from the MGA. Also, it was apparent that improved magnetic and hydrodynamic performance of the experimental system would be required for further work. The first part of the work reported here, therefore, was concerned with theoretical analysis of magnetic effects on the projectile and redesign and improvement of system performance.

Both linear and non-linear analyses of the magnetic field diffusion into the projectile and heating of its surface were attempted. The linear analysis was done in an attempt to find an approximate general solution to the problem. Computer runs were made which qualitatively indicated only that surface material was being vaporized and that the problem should be treated as non-linear. The non-linear analysis required

---

<sup>1</sup>R. L. Chapman, Meteoroid Impact Simulation by Magnetic Gradient Particle Acceleration Techniques, NAS8-5266 Technical Summary Report, AN-1098, November 1963.

iterative computer solutions of relatively basic equations developed for the purpose. Although certain assumptions were required, useful quantitative data were obtained. This too showed only surface vaporization of the projectile. Some crude corrections were also made based on the high magnetic field conductivity anomaly recently observed. These computations showed considerably less vaporization.

The improvement of system performance involved increasing the circular symmetry of explosive main charge detonation and increasing the initial magnetic field strength. At the same time, the test device was considerably simplified both from a design and test operations point of view. Although the flying cone cylindrical wave initiator previously used gave the desired simultaneous surface initiation of the explosive, facility limitations precluded any improvement of its circular symmetry. Therefore, a multiple detonator initiation system was developed. This used a ring of 24 high precision detonators spaced evenly about the center plane of the cylindrical main charge. A special firing system for assuring minimum detonator jitter was also developed. The resultant average asymmetry was 0.02 to 0.03  $\mu$ sec.

The magnetic system was changed from a battery discharge to a capacitor discharge in order to increase the initial magnetic field. The primary problem was to make the rise time long enough to allow diffusion of the flux lines to the armature interior prior to the explosive collapse. A combination of parameters was found which would give a fairly efficient system with an acceptably uniform field within the armature. The increased initial field and better explosive system resulted in the desired improvement of magnetic compression performance. Peak field strengths up to 7 Mgauss were generated.

After the improvements in MGA design and performance, work commenced on projectile acceleration experiments. These experiments



posed a special instrumentation problem because of the small projectile size, its potentially high velocity, and the transient and destructive nature of the tests. Of the many techniques considered, high speed photography was chosen. Two separate approaches were used. The first approach was a flight chamber-target block arrangement to observe the projectile's impact on a lucite block. This was done by examining the induced shock wave characteristics. The second approach used an arrangement of lenses and a special, high-intensity point source of light to photograph the projectile and flux concentrator throat during the 3.4- $\mu$ sec magnetic compression.

The projectile flight chamber experiments yielded data which indicate that metallic material from the surface of the projectile was being accelerated. No impact indicative of a solid projectile was ever seen in the lucite target, however. Direct observation inside the evacuated MGA showed luminous material coming off the inner flux concentrator surface. A self-luminous region, probably a plasma sheath, was seen to be swept in by the imploding armature. The projectile was intact shortly after the time the peak magnetic field strength was reached. It also appeared to be moving with a velocity in the low tens of km/sec range. At this point the field of view was filled with bright light which prevented further data acquisition.

These internal observation experiments were preliminary. Any future work could utilize this technique to conclusively determine if the projectile is trapped inside the MGA.

### III. THEORY

#### A. MAGNETIC FIELD DIFFUSION INTO THE PROJECTILE AND PROJECTILE HEATING

##### 1. Introduction

In the magnetic gradient accelerator multi-megagauss magnetic field strengths are experienced by the projectile. Since the rise time of the field occurs on a microsecond time scale, there will be partial penetration of the field and its associated current into the surface of the projectile. The magnitude of this is sufficient to cause heating beyond the vaporization temperature. It was necessary, therefore, to theoretically analyze this problem in order to determine projectile survivability.

This type of analysis is necessarily complex. Fundamental factors such as specific heat, electrical conductivity, and rate of magnetic field diffusion are dependent on the time history of the field and its peak value. A rigorous solution to the problem is therefore an inherently non-linear process. At the beginning of this work in July 1964, an approximate linear solution was obtained. This approach confirmed the non-linear nature of the problem, and gave a qualitative indication of the degree of field penetration.

Later on in the project, AGN acquired a computer program which could solve non-linear magnetic diffusion problems. This program yielded usable results, although the specific heat and electrical conductivity inputs were not well known above the melting point of the

projectile material. Also, it was known that very high magnetic field strengths have a pronounced effect on conductivity, but no correction was provided for this at first. Later, work on high magnetic field-conductivity effects at the Sandia Corporation was brought to the attention of project personnel. The problem was then modified to include an approximate correction for this effect and rerun. Because several functions could not be determined accurately, a precise solution was not possible. However, the problem was arranged to yield conservative answers. Nevertheless, the results were optimistic.

## 2. Linear Analysis

The detailed theoretical analysis which follows is principally due to Dr. J. E. Faulkner.

### a. General Considerations

Let us look at Maxwell's equations in rationalized units:

$$\nabla \cdot \underline{D} = \rho \quad (1)$$

$$\nabla \cdot \underline{B} = 0 \quad (2)$$

$$\nabla \times \underline{E} = -\dot{\underline{B}} \quad (3)$$

$$\nabla \times \underline{H} = \underline{J} + \dot{\underline{D}} \quad (4)$$

In addition, we have

$$\underline{D} = \epsilon_0 \underline{E} + \underline{P} \quad (5)$$

$$\underline{H} = \left( \frac{B}{\mu_0} \right) - \underline{M} \quad (6)$$

where  $\underline{P}$  is the electric polarization vector and  $\underline{M}$  is the intensity of magnetization vector. Let

$$\rho^* = \rho - \nabla \cdot \underline{P} \quad (7)$$

$$\underline{I}^* = \underline{J} + \nabla \times \underline{M} + \dot{\underline{P}} \quad (8)$$

Substituting (5) and (6) into (1) and (4) and using (7) and (8), we have

$$\nabla \cdot \underline{E} = \rho^*/\epsilon_0 \quad (9)$$

$$\nabla \times \underline{B} = \mu_0 \underline{J}^* + \mu_0 \epsilon_0 \dot{\underline{E}} \quad (10)$$

From (2) we may write

$$\underline{B} = \nabla \times \underline{A} . \quad (11)$$

Substitute (11) into (3) and get that

$$\nabla \times (\underline{E} + \dot{\underline{A}}) = 0 \quad (12)$$

This means that

$$\underline{E} = -\dot{\underline{A}} - \nabla\varphi . \quad (13)$$

The quantities  $\underline{A}$  and  $\varphi$  are called respectively the vector and scalar potential. They are not uniquely determined by their definition. Let  $\Lambda$  be a scalar and let

$$\varphi^* = \varphi + \dot{\Lambda} \quad (14)$$

$$\underline{A}^* = \underline{A} - \nabla\Lambda . \quad (15)$$

Then

$$\underline{B} = \nabla \times \underline{A}^* \quad (16)$$

$$\underline{E} = -\dot{\underline{A}}^* - \nabla\varphi^* \quad (17)$$

Thus  $\underline{A}^*$  and  $\varphi^*$  give the same  $\underline{B}$  and  $\underline{E}$  as  $\underline{A}$  and  $\varphi$ .

Equations (14) and (15) are called a gauge transformation. Substitute Eqs. (11) and (13) into Eq. (10).

$$\nabla(\nabla \cdot \underline{A}) - \nabla^2 \underline{A} = \mu_0 \underline{J}^* + \mu_0 \epsilon_0 \left[ -\ddot{\underline{A}} - \nabla \dot{\phi} \right]. \quad (18)$$

Since, as we have seen,  $\underline{A}$  and  $\phi$  are somewhat arbitrary, we may subject them to an auxiliary condition

$$\nabla \cdot \underline{A} + \mu_0 \epsilon_0 \dot{\phi} = 0. \quad (19)$$

Equation (19) is called the Lorentz condition. From Eqs. (18) and (19), we see that

$$-\nabla^2 \underline{A} + \mu_0 \epsilon_0 \ddot{\underline{A}} = \mu_0 \underline{J}^*. \quad (20)$$

From (9), (13), and (19) we get

$$-\nabla^2 \phi + \mu_0 \epsilon_0 \ddot{\phi} = \rho^* / \epsilon_0. \quad (21)$$

The solutions of Eqs. (20) and (21) for  $\underline{A}$  and  $\phi$  in terms of  $\rho^*$  and  $\underline{J}^*$  may be written

$$\underline{A}(\underline{r}, t) = \frac{\mu_0}{4\pi} \int \frac{\underline{J}^*(\underline{r}', t^*) d^3 r'}{|\underline{r} - \underline{r}'|} \quad (22)$$

$$\phi(\underline{r}, t) = \frac{1}{4\pi \epsilon_0} \int \frac{\rho^*(\underline{r}', t^*) d^3 r'}{|\underline{r} - \underline{r}'|} \quad (23)$$

where

$$t^* = t - \frac{|\underline{r} - \underline{r}'|}{\sqrt{\mu_0 \epsilon_0}} \quad (24)$$

The quantity  $t^*$  is called the retarded time.

Now let us look at the solution of Maxwell's equations in the diffusion approximation. Let us also assume that  $\rho^* = 0$ , so that  $\phi = 0$ . We are neglecting  $\dot{\underline{E}}$  in Eq. (10).

Assume Ohm's law

$$\underline{J}^* = \sigma \underline{E} \quad (25)$$

then

$$\underline{J}^* = -\sigma \dot{\underline{A}}. \quad (26)$$

From (11), (26) and (10) without  $\dot{\underline{E}}$  we get

$$\nabla^2 \underline{A} = \mu_0 \sigma \dot{\underline{A}} \quad (27)$$

Since Eq. (27) forms the basis of subsequent work, it is well to review the assumptions. First, Eq. (27) is valid only in a system which moves with the material. This means that if there is hydrodynamic motion Eq. (27) is valid in the Lagrangian system rather than the Eulerian system. We usually write  $\underline{J} = \sigma \underline{E}$  rather than  $\underline{J}^* = \sigma \underline{E}$ . If we take the first form and assume  $B = \mu H$ , where  $\mu$  is a constant in space, then Eq. (27) becomes  $\nabla^2 \underline{A} = \mu \sigma \dot{\underline{A}}$ . If  $\mu$  is not constant in space, Eq. (27) is even more complicated. Finally, we assume the fields move around by diffusion rather than radiation so that the vacuum speed of light is infinite.

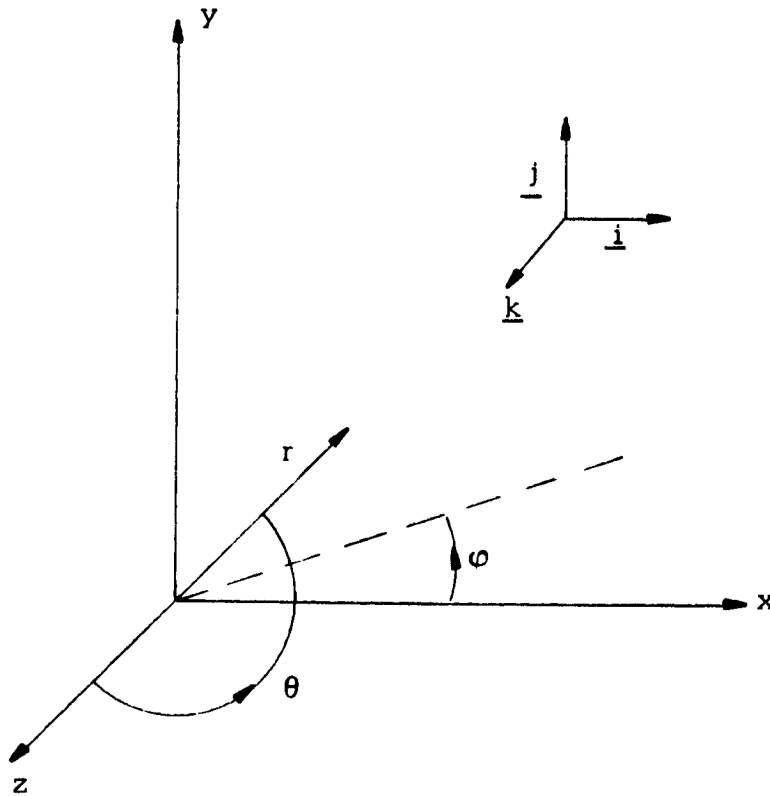
#### b. Magnetic Diffusion Into a Sphere

A sphere of conductivity  $\sigma$  is placed in a magnetic field  $B$ . We wish to find the current distribution in the sphere as a function of time. Both  $B$  and  $\sigma$  may be time dependent.

Let us start with Eq. (27).

$$\nabla^2 \underline{A} = \mu_0 \sigma \dot{\underline{A}} \quad (27)$$

Let us solve this equation first with constant  $B$  and  $\sigma$ . Let the radius of the sphere be  $r_0$ . The coordinate system is shown below.



$x, y, z$  form a right-handed coordinate system. The radius vector is  $r$ . The angle that  $r$  makes with the  $z$  axis is  $\theta$ . The angle that the projection of  $r$  in the  $x, y$  plane makes with the  $x$  axis is  $\phi$ .  $\underline{i}, \underline{j}$ , and  $\underline{k}$  are unit vectors parallel respectively to the  $x, y$ , and  $z$  axes, respectively. The volume element is

$$d^3\underline{r} = r^2 dr \sin \theta d\theta d\phi. \quad (28)$$

The sphere is at the origin. The external magnetic field not from the sphere eddy current is given by

$$\underline{B} = \underline{k}B. \quad (29)$$

The initial vector potential with the eddy currents is given by

$$\begin{aligned} \underline{A}|_{t=0} &= \frac{B}{2} \sin \theta (-i \sin \varphi + j \cos \varphi) \left( r - r_o^3/r^2 \right) & (r \geq r_o) \\ &= 0 & (r \leq r_o) \end{aligned} \quad (30)$$

Note that  $\underline{A}|_{t=0}$  vanishes on the sphere as it should since there is no flux inside the sphere. The  $r^{-2}$  dependence represents the field from the eddy currents while the  $r$  dependence is from the field of the external source.

Let us construct a solution of (27) in the form

$$\underline{A}_n^i(\underline{r}, t) = \underline{a}_n(\underline{r}) e^{-\alpha_n t} \quad (31)$$

The reason for the subscript  $n$  and the superscript  $i$  will be clear later. Putting (31) into (27) gives

$$\nabla^2 \underline{a}_n(\underline{r}) = \mu_o \sigma \alpha_n \underline{a}_n(\underline{r}). \quad (32)$$

Now write

$$\underline{a}_n(\underline{r}) = a_n(r) \sin \theta (-i \sin \varphi + j \cos \varphi). \quad (33)$$

Note that

$$|\underline{a}_n(\underline{r})| = |\sin \theta| |a_n(r)|. \quad (34)$$

If  $U(\underline{r})$  is any spatial function then

$$\nabla^2 U = \frac{1}{r^2} \frac{\partial}{\partial r} \left( r^2 \frac{\partial U}{\partial r} \right) + \frac{1}{r^2 \sin \theta} \frac{\partial}{\partial \theta} \left[ \sin \theta \frac{\partial U}{\partial \theta} \right] + \frac{1}{r^2 \sin^2 \theta} \frac{\partial^2 U}{\partial \varphi^2} \quad (35)$$



From (32), (33), and (35), we get

$$\frac{1}{r^2} \frac{d}{dr} \left( r^2 \frac{da_n}{dr} \right) - 2a_n / r^2 = -\mu_0 \sigma \alpha_n a_n. \quad (36)$$

Now let

$$\rho_n = r \sqrt{\mu_0 \sigma \alpha_n}. \quad (37)$$

Then

$$\rho_n^2 \frac{d^2 a_n}{d\rho_n^2} + 2\rho_n \frac{da_n}{d\rho_n} + (\rho_n^2 - 2) a_n = 0. \quad (38)$$

The solution to (38), which is not singular at  $\rho_n = 0$ , is

$$a_n = \frac{\sin \rho_n}{\rho_n^2} - \frac{\cos \rho_n}{\rho_n}. \quad (39)$$

Note that

$$a_n = \left( \frac{\pi}{2} \right)^{1/2} \rho_n^{-1/2} J_{3/2}(\rho_n) \quad (40)$$

where  $J_{3/2}(\rho_n)$  is a Bessel function of argument  $\rho_n$ .

Combining (31), (33), and (39), we have the internal vector potential

$$\underline{A}_n^i = e^{-\alpha_n t} \sin \theta (-\underline{i} \sin \varphi + \underline{j} \cos \varphi) \left( \frac{\sin \rho_n}{\rho_n^2} - \frac{\cos \rho_n}{\rho_n} \right). \quad (41)$$

From Eq. (26)

$$\underline{J} = -\sigma \dot{\underline{A}}. \quad (42)$$

Thus, the current density  $\underline{J}_n$  from  $\underline{A}_n^i$  is given by

$$\underline{J}_n = \alpha_n \sigma e^{-\alpha_n t} \sin \theta (-\underline{i} \sin \varphi + \underline{j} \cos \varphi) \left( \frac{\sin \rho_n}{\rho_n^2} - \frac{\cos \rho_n}{\rho_n} \right) \quad (43)$$

Let  $\underline{A}_n^O$  be the external vector potential caused by  $\underline{J}_n$ . Formula (22) gives

$$\underline{A}_n^O = \frac{\mu_o}{4\pi} \int \frac{\underline{J}_n d^3 r'}{|\underline{r} - \underline{r}'|} \quad (44)$$

In (44) we expand  $|\underline{r} - \underline{r}'|^{-1}$  in spherical harmonics. Clearly, the only relevant ones are for  $\ell = 1$ ,  $m = \pm 1$ . Thus

$$|\underline{r} - \underline{r}'|^{-1} = \frac{r'}{r^2} \sin \theta \sin \theta' (\cos \varphi \cos \varphi' + \sin \varphi \sin \varphi') \quad (45)$$

+ irrelevant terms.

From (28) and (37)

$$d^3 r' = (r')^2 dr' \sin \theta' d\theta' d\varphi' = (\mu_o \sigma \alpha_n)^{-3/2} (\rho_n')^2 d\rho_n' \sin \theta' d\theta' d\varphi' \quad (46)$$

Combining (43), (44), (45) and (46) gives

$$\begin{aligned} \underline{A}_n^O &= (4\pi \alpha_n \mu_o \sigma^2)^{-1} \int_0^\pi \sin \theta' d\theta' \int_0^{2\pi} d\varphi' \sin \theta \sin \theta' (\cos \varphi \cos \varphi' + \sin \varphi \sin \varphi') \\ &\quad \sin \theta' (-\underline{i} \sin \varphi' + \underline{j} \cos \varphi') \\ &\quad \times \int_0^{\rho_{on}} (\rho_n')^3 \left[ \frac{\sin \rho_n'}{(\rho_n')^2} - \frac{\cos \rho_n'}{\rho_n'} \right] d\rho_n' \end{aligned} \quad (47)$$

where

$$\rho_{on} = r_o \sqrt{\alpha_n \mu_o \sigma} . \quad (48)$$

From the relationship

$$\int_0^{\pi} \sin^3 \theta' d\theta' = 4/3 \quad (49)$$

$$\int_0^{2\pi} \sin^2 \varphi' d\varphi' = \int_0^{2\pi} \cos^2 \varphi' d\varphi' = \pi \quad (50)$$

$$\int_0^{2\pi} \sin \varphi' \cos \varphi' d\varphi' = 0 \quad (51)$$

$$\begin{aligned} \int_0^{\rho_{on}} (\rho'_n)^3 \left[ \frac{\sin \rho'_n}{(\rho'_n)^2} - \frac{\cos \rho'_n}{\rho'_n} \right] d\rho'_n &= \left[ -(\rho'_n)^2 \sin \rho'_n - 3\rho'_n \cos \rho'_n + 3 \sin \rho'_n \right]_0^{\rho_{on}} \\ &= -\rho_{on}^2 \sin \rho_{on} - 3\rho_{on} \cos \rho_{on} + 3 \sin \rho_{on} . \end{aligned} \quad (52)$$

We have

$$\underline{A}_n^O = \frac{e^{-\alpha_n t} \sin \theta (-j \sin \varphi + j \cos \varphi)}{3\alpha_n \mu_o \sigma r^2} \left[ -\rho_{on}^2 \sin \rho_{on} - 3\rho_{on} \cos \rho_{on} + 3 \sin \rho_{on} \right] \quad (53)$$

Note that

$$\nabla^2 \underline{A}_n^O = 0 . \quad (54)$$

Equation (54) states that there is no current outside the sphere .

Now let us demand that the two solutions (53) and (41) are continuous at  $r = r_o$  . This means that

$$\frac{\sin \rho_{on}}{\rho_{on}^2} - \frac{\cos \rho_{on}}{\rho_{on}} = \frac{1}{3\rho_{on}^2} \left[ -\rho_{on}^2 \sin \rho_{on} - 3\rho_{on} \cos \rho_{on} + 3 \sin \rho_{on} \right] \quad (55)$$

Equation (55) may be satisfied if

$$\sin \rho_{on} = 0 \quad (56)$$

so that

$$\rho_{on} = n\pi \quad (57)$$

From Eqs. (48) and (57)

$$\alpha_n = \frac{n^2 \pi^2}{\mu_o \sigma r_o^2} \quad (58)$$

From (37) and (58)

$$\rho_n = n\pi r/r_o \quad (59)$$

From (59), (58), and (41), inside the sphere, we obtain

$$\begin{aligned} \underline{A}_n^i &= e^{-n^2 \pi^2 t / \mu_o \sigma r_o^2} \sin \theta (-\underline{i} \sin \varphi + \underline{j} \cos \varphi) \\ &\times \left( \frac{r_o^2}{n^2 \pi^2 r^2} \sin \frac{n\pi r}{r_o} - \frac{r_o}{n\pi r} \cos \frac{n\pi r}{r_o} \right) \end{aligned} \quad (60)$$

for  $r \leq a$ , and from (53), (57), (58), and (59), outside the sphere

$$\underline{A}_n^O = \frac{(-1)^{n+1} r_o^2}{n\pi r^2} e^{-\frac{n^2 \pi^2 t}{\mu_o \sigma r_o^2}} \sin \theta (-\underline{i} \sin \varphi + \underline{j} \cos \theta) \quad (61)$$

for  $r \geq a$ . Define  $\underline{A}_n$  by

$$\underline{A}_n = \underline{A}_n^i \quad r \leq r_o \quad (62)$$

$$\underline{A}_n = \underline{A}_n^O \quad r \geq r_o \quad (63)$$

then  $\underline{A}_n$  and its derivatives are continuous at  $r = r_o$ . Note that  $\underline{A}_n^i$ ,  $\underline{A}_n^O$ , and  $\underline{A}_n$  are dimensionless but that  $\underline{A}$  is not.

Now let us look at the integral properties of the  $a_n$ 's

$$\begin{aligned} \int_0^{r_0} a_n a_{n'} r^2 dr &= \int_0^{r_0} r^2 dr \left( \frac{r_0^2}{n^2 \pi^2 r^2} \sin \frac{n\pi r}{r_0} - \frac{r_0}{n\pi r} \cos \frac{n\pi r}{r_0} \right) \\ &\times \left( \frac{r_0^2}{n'^2 \pi^2 r^2} \sin \frac{n'\pi r}{r_0} - \frac{r_0}{n'\pi r} \cos \frac{n'\pi r}{r_0} \right). \end{aligned} \quad (64)$$

By integration by parts

$$\begin{aligned} \int_0^{r_0} \frac{r_0^4}{n^2 n'^2 \pi^4 r^2} \sin \frac{n\pi r}{r_0} \sin \frac{n'\pi r}{r_0} dr &= - \frac{r_0^4}{n^2 n'^2 \pi^4 r} \sin \frac{n'\pi r}{r_0} \Big|_0^{r_0} \\ &+ \int_0^{r_0} \frac{dr}{r} \frac{r_0^3}{\pi^3} \left[ \frac{\cos n\pi r/r_0}{n n'^2} \sin \frac{n'\pi r}{r_0} + \frac{\sin n\pi r/r_0}{n^2 n'} \cos \frac{n'\pi r}{r_0} \right] \end{aligned} \quad (65)$$

Furthermore,

$$\frac{r_0^2}{\pi^2 n n'} \int_0^{r_0} \cos \frac{n'\pi r}{r_0} \cos \frac{n\pi r}{r_0} = \frac{r_0^3}{2n^2 \pi^2} \delta_{nn'}. \quad (66)$$

Thus

$$\int_0^{r_0} a_n a_{n'} r^2 dr = \frac{r_0^3}{2n^2 \pi^2} \delta_{nn'}. \quad (67)$$

Now

$$\begin{aligned} \int_0^{r_0} r a_n r^2 dr &= \int_0^{r_0} r^3 dr \left( \frac{r_0^2}{n^2 \pi^2 r^2} \sin \frac{n\pi r}{r_0} - \frac{r_0}{n\pi r} \cos \frac{n\pi r}{r_0} \right) \\ &= \left[ - \frac{r_0^2}{n^2 \pi^2} r^2 \sin \frac{n\pi r}{r_0} - \frac{3r_0^3}{n^3 \pi^3} \cos \frac{n\pi r}{r_0} + \frac{3r_0^4}{n^4 \pi^4} \sin \frac{n\pi r}{r_0} \right]_0^{r_0} \\ &= (-1)^{n+1} 3r_0^4 / n^3 \pi^3 \end{aligned} \quad (68)$$

so that

$$\frac{\int_0^{r_0} r a_n^2 dr}{\int_0^{r_0} a_n^2 r^2 dr} = (-1)^{n+1} 6r_0 / n\pi. \quad (69)$$

Thus

$$\underline{A} = \frac{B}{2} \left[ r \sin \theta (-\underline{i} \sin \varphi + \underline{j} \cos \varphi) - 6 \sum_{n=1}^{\infty} \frac{(-1)^{n+1} r_0}{n\pi} \underline{A}_n \right] \quad (70)$$

Note that

$$\sum_{n=1}^{\infty} 1/n^2 = \pi^2/6 \quad (71)$$

so that (70) agrees with (30) for  $t = 0$ .

Now, let  $\underline{A}_n^s$  be the spatial part of  $\underline{A}_n$  so that

$$\underline{A}_n = e^{-\frac{n^2 \pi^2 t}{\mu_0 \sigma r_0^2}} \underline{A}_n^s(r) \quad (72)$$

Now suppose a field of strength  $B_i$  is switched on at time  $t_{i-1}$  and switched off at  $t_i$ . Then at  $t > t_i$  the potential  $\underline{A}_i$  is given by

$$\underline{A}_i = \frac{3B_i r_0}{\pi} \sum_{n=1}^{\infty} \frac{(-1)^{n+1}}{n} \left[ e^{-\frac{n^2 \pi^2 (t-t_i)}{\mu_0 \sigma r_0^2}} - e^{-\frac{n^2 \pi^2 (t-t_{i-1})}{\mu_0 \sigma r_0^2}} \right] \underline{A}_n^s \quad (73)$$

By expanding the exponentials, we see that to first order in  $t_i - t_{i-1}$

$$e^{-\frac{n^2 \pi^2 (t-t_i)}{\mu_o \sigma r_o^2}} - e^{-\frac{n^2 \pi^2 (t-t_{i-1})}{\mu_o \sigma r_o^2}} = \frac{n^2 \pi^2 (t_i - t_{i-1})}{\mu_o \sigma r_o^2} e^{-\frac{n^2 \pi^2 (t-t_i)}{\mu_o \sigma r_o^2}} \quad (74)$$

so that

$$\underline{A}(\underline{r}, t) = \frac{3\pi}{\mu_o \sigma r_o} \sum_{n=1}^{\infty} (-1)^{n+1} n \int_0^t B(t') dt' e^{-\frac{n^2 \pi^2 (t-t')}{\mu_o \sigma r_o^2}} \underline{A}_n^s(\underline{r}) \quad (75)$$

Now let us look at the case where  $\sigma$  varies with  $t$ . If we go back to (31) we see that we can still make the separation by replacing

$$\frac{n^2 \pi^2 t}{\mu_o r_o^2 \sigma} \text{ by } \frac{n^2 \pi^2}{\mu_o r_o^2} \int_0^t \frac{dt'}{\sigma(t')}$$

By carrying this idea through, we see that in Eq. (75) we must replace

$$\frac{n^2 \pi^2 (t-t')}{\mu_o \sigma r_o^2} \text{ by } \frac{n^2 \pi^2}{\mu_o r_o^2} \int_{t'}^t \frac{dt''}{\sigma(t'')} .$$

Thus, the result is

$$\underline{A}(\underline{r}, t) = \frac{3\pi}{\mu_o r_o} \sum_{n=1}^{\infty} (-1)^{n+1} n \int_0^t \frac{B(t') dt'}{\sigma(t')} e^{-\frac{n^2 \pi^2}{\mu_o r_o^2} \int_{t'}^t \frac{dt''}{\sigma(t'')}} \underline{A}_n^s(\underline{r}) \quad (76)$$

c. Ohmic Heating due to Magnetic Diffusion

If the total energy due to ohmic heating at time  $t$  is  $W(t)$  then

$$W(t) = \int_0^t dt' \iiint d^3 \underline{r} \eta(t') \underline{J}^2(\underline{r}, t) . \quad (77)$$

Using Eq. (76)

$$\underline{A}(\underline{r}, t) = \frac{3\pi}{\mu_o r_o} \sum_{n=1}^{\infty} (-1)^{n+1} n \int_0^t \frac{B(t') dt'}{\sigma(t')} e^{-\frac{n^2 \pi^2}{2} \int_{t'}^t \frac{dt''}{\sigma(t'')}} \underline{A}_n^S(\underline{r}) \quad (76)$$

where for  $r \leq r_o$

$$\underline{A}_n^S(\underline{r}) = \sin \theta (-\underline{i} \sin \varphi + j \cos \theta) a_n(r) . \quad (78)$$

Now

$$\underline{J} = -\sigma \dot{\underline{A}} \quad (79)$$

so that

$$\underline{J} = \frac{3\pi}{\mu_o r_o} \sum_{n=1}^{\infty} (-1)^n n F_n(t) \underline{A}_n^S(\underline{r}) \quad (80)$$

where

$$F_n(t) = B(t) - \frac{n^2 \pi^2}{2} \int_0^t \frac{B(t') dt'}{\sigma(t')} e^{-\frac{n^2 \pi^2}{2} \int_{t'}^t \frac{dt''}{\sigma(t'')}} \quad (81)$$

thus

$$\underline{J}^2 = \frac{9\pi^2}{\mu_o^2 r_o^2} \sum_{n=1}^{\infty} \sum_{n'=1}^{\infty} (-1)^{n+n'} n n' F_n F_{n'} \underline{A}_n^S \cdot \underline{A}_{n'}^S, \quad (82)$$



since

$$d^3 \underline{r} = r^2 dr \sin \theta d\theta d\phi \quad (83)$$

then from (78)

$$\iiint d^3 \underline{r} A_n^s(\underline{r}) A_{n'}^s(\underline{r}) = 2\pi \int_0^\pi \cos^3 \theta d\theta \int_0^{r_0} r^2 a_n(r) a_{n'}(r) dr. \quad (84)$$

Now

$$\int_0^\pi \cos^3 \theta d\theta = 4/3. \quad (85)$$

From Eq. (67)

$$\int_0^{r_0} r^2 a_n(r) a_{n'}(r) dr = \frac{r_0^3}{2n^2 \pi^2} \delta_{nn'}, \quad (86)$$

so that

$$\iiint d^3 \underline{r} A_n^s(\underline{r}) A_{n'}^s(\underline{r}) = \frac{4r_0^3}{3n^2 \pi} \delta_{nn'}, \quad (87)$$

thus

$$\iiint J^2 d^3 \underline{r} = \frac{12\pi r_0}{\mu_0^2} \sum_{n=1}^{\infty} F_n^2 \quad (88)$$

so that

$$W(t) = \frac{12\pi r_0}{\mu_0^2} \sum_{n=1}^{\infty} \int_0^t dt' F_n^2(t') / \sigma(t') \quad (89)$$

The above equation is in a form suitable for numerical calculation. However, before this is attempted, it must be shown that the series will converge in the limit.

Let us assume that  $B$  is an exponentially increasing function for purposes of the convergence proof. Consider two series of positive terms

$\sum_{n=1}^{\infty} S_n$  and  $\sum_{n=1}^{\infty} T_n$ . By definition  $\sum_{n=1}^{\infty} S_n$  is convergent. Suppose there exists an  $n'$  such that for  $n$  greater than  $n'$

$$S_n \geq T_n \quad (90)$$

then  $\sum_{n=1}^{\infty} T_n$  is convergent. Since this is a standard theorem, its proof will be omitted here.

Let us start with Eq. (81):

$$F_n(t) = B(t) - \frac{n^2 \pi^2}{\mu_o r_o^2} \int_0^t \frac{B(t') dt'}{\sigma(t')} e^{-\frac{n^2 \pi^2}{\mu_o r_o^2} \int_{t'}^t \frac{dt''}{\sigma(t'')}} \quad (91)$$

Note that

$$\int_{t'}^t \frac{dt''}{\sigma(t'')} \equiv \int_0^t \frac{dt''}{\sigma(t'')} - \int_0^{t'} \frac{dt''}{\sigma(t'')} \quad (92)$$

so that

$$F_n(t) = B(t) - \frac{n^2 \pi^2}{\mu_o r_o^2} e^{-\frac{n^2 \pi^2}{\mu_o r_o^2} \int_0^t \frac{dt''}{\sigma(t'')}} \int_0^t \frac{B(t') dt'}{\sigma(t')} e^{\frac{n^2 \pi^2}{\mu_o r_o^2} \int_0^{t'} \frac{dt''}{\sigma(t'')}} \quad (93)$$

Now

$$\frac{d}{dt'} e^{\frac{n^2 \pi^2}{\mu_o r_o^2} \int_0^{t'} \frac{dt''}{\sigma(t'')}} = \frac{n^2 \pi^2}{\mu_o r_o^2 \sigma(t')} e^{\frac{n^2 \pi^2}{\mu_o r_o^2} \int_0^{t'} \frac{dt''}{\sigma(t'')}} \quad (94)$$

Thus

$$F_n(t) = B(t) - e^{-\frac{n^2 \pi^2}{\mu_o r_o^2} \int_0^t \frac{dt''}{\sigma(t'')}} \int_0^t dt' B(t') \frac{d}{dt'} e^{\frac{n^2 \pi^2}{\mu_o r_o^2} \int_0^{t'} \frac{dt''}{\sigma(t'')}} \quad (95)$$

By integration by parts

$$F_n(t) = B(t) - e^{-\frac{n^2 \pi^2}{\mu_o r_o^2} \int_0^t \frac{dt''}{\sigma(t'')}} \left\{ \left[ B(t') e^{\frac{n^2 \pi^2}{\mu_o r_o^2} \int_0^{t'} \frac{dt''}{\sigma(t'')}} \right]_{t'=0}^{t'=t} - \int_0^t dt' e^{\frac{n^2 \pi^2}{\mu_o r_o^2} \int_0^{t'} \frac{dt''}{\sigma(t'')}} \frac{d}{dt'} B(t') \right\} \quad (96)$$

Now

$$\left[ B(t') e^{\frac{n^2 \pi^2}{\mu_o r_o^2} \int_0^{t'} \frac{dt''}{\sigma(t'')}} \right]_{t'=0}^{t'=t} = B(t) e^{\frac{n^2 \pi^2}{\mu_o r_o^2} \int_0^t \frac{dt''}{\sigma(t'')}} - B(0) \quad (97)$$

so that

$$F_n(t) = B(t) - e^{-\frac{n^2 \pi^2}{\mu_o r_o^2} \int_0^t \frac{dt''}{\sigma(t'')}} \left\{ B(t) e^{\frac{n^2 \pi^2}{\mu_o r_o^2} \int_0^t \frac{dt''}{\sigma(t'')}} - B(0) - \int_0^t dt' e^{\frac{n^2 \pi^2}{\mu_o r_o^2} \int_0^{t'} \frac{dt''}{\sigma(t'')}} \frac{d}{dt'} B(t') \right\} \quad (98)$$

Equation (98) reduces to

$$F_n(t) = B(0) e^{-\frac{n^2 \pi^2}{\mu_o r_o^2} \int_0^t \frac{dt''}{\sigma(t'')}} - \frac{n^2 \pi^2}{\mu_o r_o^2} \int_0^t \frac{dt''}{\sigma(t'')} \int_0^t dt' e^{-\frac{n^2 \pi^2}{\mu_o r_o^2} \int_0^{t'} \frac{dt''}{\sigma(t'')}} \frac{d}{dt'} B(t') . \quad (99)$$

From Eq. (92)

$$e^{-\frac{n^2 \pi^2}{\mu_o r_o^2} \int_0^t \frac{dt''}{\sigma(t'')}} \int_0^t dt' e^{-\frac{n^2 \pi^2}{\mu_o r_o^2} \int_0^{t'} \frac{dt''}{\sigma(t'')}} \frac{d}{dt} B(t') = \int_0^t dt' e^{-\frac{n^2 \pi^2}{\mu_o r_o^2} \int_{t'}^t \frac{dt''}{\sigma(t'')}} \frac{d}{dt'} B(t') \quad (100)$$

Equation (99) thus becomes

$$F_n(t) = B(0) e^{-\frac{n^2 \pi^2}{\mu_o r_o^2} \int_0^t \frac{dt''}{\sigma(t'')}} + \int_0^t dt' e^{-\frac{n^2 \pi^2}{\mu_o r_o^2} \int_{t'}^t \frac{dt''}{\sigma(t'')}} \frac{d}{dt'} B(t') . \quad (101)$$

Let  $\sigma_{\max}$  be an upper bound of the conductivity, this implies

$$\int_0^t \frac{dt''}{\sigma(t'')} \geq t/\sigma_{\max} \quad (102)$$

$$\int_{t'}^t \frac{dt''}{\sigma(t'')} \geq (t-t')/\sigma_{\max} \quad (103)$$

From Eqs. (102) and (103)

$$e^{-\frac{n^2 \pi^2}{\mu_o r_o^2} \int_0^t \frac{dt''}{\sigma(t'')}} \leq e^{-\frac{n^2 \pi^2 t}{\mu_o r_o^2 \sigma_{\max}}} \quad (104)$$

$$e^{-\frac{n^2 \pi^2}{\mu_o r_o^2} \int_{t'}^t \frac{dt''}{\sigma(t'')}} \leq e^{-\frac{n^2 \pi^2 (t-t')}{\mu_o r_o^2 \sigma_{\max}}} . \quad (105)$$

Thus

$$F_n(t) \leq B(0) e^{-\frac{n^2 \pi^2 t}{\mu_o r_o^2 \sigma_{\max}}} + \int_0^t dt' e^{-\frac{n^2 \pi^2 (t-t')}{\mu_o r_o^2 \sigma_{\max}}} \frac{d}{dt'} B(t') . \quad (106)$$

Since it is assumed that  $B$  is an exponentially increasing function of time, we may write

$$B(t') = B(0) e^{\alpha t'} . \quad (107)$$

So that

$$\frac{d}{dt'} B(t') = \alpha B(0) e^{\alpha t'} . \quad (108)$$

Putting Eq. (108) into (106) gives

$$F_n(t) \leq B(0) e^{-\frac{n^2 \pi^2 t}{\mu_o r_o^2 \sigma_{\max}}} + \alpha \int_0^t dt' B(0) e^{\alpha t' - \frac{n^2 \pi^2 (t-t')}{\mu_o r_o^2 \sigma_{\max}}} . \quad (109)$$

Define  $\beta$  by

$$\beta = \frac{\frac{n^2 \pi^2}{\mu_o r_o^2 \sigma_{\max}}}{\alpha} . \quad (110)$$

Let the right side of (109) be  $u_n(t)$  so that it may be written

$$F_n(t) \leq u_n(t) \quad (111)$$

By carrying out the integration in (109) we see that

$$u_n(t) = \frac{B(0)}{\alpha + \beta} (\alpha e^{\alpha t} + \beta e^{-\beta t}). \quad (112)$$

Let  $\sigma_{\min}$  be a positive, non-zero, lower bound on the conductivity. Then

$$\int_0^t dt' F_n^2(t')/\sigma(t') \leq \frac{1}{\sigma_{\min}} \int_0^t F_n^2(t') dt'. \quad (113)$$

From (111)

$$\int_0^t F_n^2(t') dt' \leq \int_0^t u_n^2(t') dt'. \quad (114)$$

So that

$$\int_0^t dt' F_n^2(t')/\sigma(t') \leq \frac{1}{\sigma_{\min}} \int_0^t u_n^2(t') dt'. \quad (115)$$

From (112)

$$\int_0^t u_n^2(t') dt' = \frac{B^2(0)}{(\alpha + \beta)^2} \left[ \frac{\alpha}{2} e^{2\alpha t} + \frac{2\alpha\beta}{\alpha - \beta} e^{(\alpha - \beta)t} - \frac{\beta}{2} e^{-2\beta t} - \frac{\alpha}{2} - \frac{2\alpha\beta}{\alpha + \beta} + \frac{\beta}{2} \right] \quad (116)$$

From Eq. (110) we see that  $\beta \rightarrow \infty$  as  $n \rightarrow \infty$  so that

$$\lim_{n \rightarrow \infty} \frac{\beta^2}{(\alpha + \beta)^2} = 1 \quad (117)$$

$$\lim_{n \rightarrow \infty} \frac{2}{\beta} \left[ \frac{\alpha}{2} e^{2\alpha t} + \frac{2\alpha\beta}{\alpha - \beta} e^{(\alpha - \beta)t} - \frac{\beta}{2} e^{-2\beta t} - \frac{\alpha}{2} - \frac{2\alpha\beta}{\alpha + \beta} + \frac{\beta}{2} \right] = 1. \quad (118)$$

Define  $\gamma_n$  by

$$\frac{2\beta}{B^2(0)} \int_0^t u_n^2(t') dt' = \gamma_n \quad (119)$$

then

$$\lim_{n \rightarrow \infty} \gamma_n = 1. \quad (120)$$

From Eq. (120) it follows that there exists an  $n'$  such that for  $n > n'$ ,  $\gamma_n < 2$ . This means that

$$\int_0^t u_n^2(t') dt' < \frac{B^2(0)}{\beta} \quad \text{for } n > n'. \quad (121)$$

From Eqs. (110), (115), and (121), it follows that

$$\int_0^t F_n^2(t') dt' / \sigma(t') < \frac{\sigma_{\max}}{\sigma_{\min}} \frac{\mu_o r_o^2 B^2(0)}{n^2 \pi^2} \quad \text{for } n > n'. \quad (122)$$

Since  $\sum_{n=1}^{\infty} 1/n^2$  is convergent, it follows that  $\sum_{n=1}^{\infty} \frac{\sigma_{\max}}{\sigma_{\min}} \frac{\mu_o r_o^2 B^2(0)}{n^2 \pi^2}$  is a convergent series. From Eq. (122) and the basic theorem on convergence it follows that  $\sum_{n=1}^{\infty} \int_0^t F_n^2(t') dt' / \sigma(t')$  is a convergent series.

d. The Numerical Solution of the  
Magnetic Diffusion into a Sphere

(1) General

The analytic model which was set up in the preceding sections for a spherical particle in an exponentially increasing magnetic field is evaluated numerically. The equations of diffusion that were used assumed that the electric charge density ( $\rho$ ) was zero and that the time rate of change of the electric field ( $\dot{E}$ ) could be neglected. The result of these assumptions is the magnetic diffusion Eq. (27) repeated below.

$$\nabla^2 \underline{A} = \mu_o \sigma \frac{\partial \underline{A}}{\partial t} \quad (27)$$

The solution of this equation (where  $\underline{A}$  is the magnetic vector potential,  $\mu_0$  the free-space permeability,  $\sigma$  the conductivity) leads to an integral expression for  $A(\underline{r}, t)$  in the case of a stationary conducting sphere in an increasing magnetic field.

The expression for the deposited heat energy as a function of time,  $W(t)$  is given by

$$W(t) = \frac{12\pi r_0^2}{\mu_0} \sum_{n=1}^{\infty} \int_0^t \frac{dt' F_n^2(t')}{\sigma(t')} \quad (123)$$

where  $F_n(t')$  is given by the expression:

$$F_n(t') = B(t') - \frac{n^2 \pi^2}{\mu_0 r_0^2} \int_0^{t'} \frac{B(t'') dt''}{\sigma(t'')} \exp \left[ -\frac{n^2 \pi^2}{\mu_0 r_0^2} \int_{t''}^{t'} \frac{dt'''}{\sigma(t''')} \right] \quad (124)$$

Here  $r_0$  is the radius of the metallic sphere,  $\mu_0$  the magnetic free space permeability,  $B(t)$  the magnetic field intensity as a function of time, and  $\sigma(t)$  the variable conductivity of the metal, in this case aluminum.

Equation (27) is non-linear because of the dependence of  $\sigma$  on magnetic field strength as well as time. The solution from which Eq. (123) can be obtained is calculated under the assumption that  $\sigma$  is a function of time only.

The units used throughout this study are those of the MKSA system (meters, kilograms, seconds, amperes).

## (2) Physical Assumptions

In order to follow the behavior of the magnetic field in the aluminum medium, it is necessary to make certain initial and boundary value assumptions. The  $B$  field (magnetic intensity) not due to sphere eddy currents was specified as constant in space and varying exponentially with time (i.e.,  $B = B_0 e^{\alpha t}$ ). Because the



phenomena of interest occur within time intervals of a half-microsecond, the time constant,  $\alpha$ , was chosen so that B increased one hundredfold within that period of time ( $\alpha = 1.844 \times 10^7 \text{ sec}^{-1}$ ).  $B_0$ , the initial magnetic field, was chosen to be 50,000 gauss (5 webers/meter<sup>2</sup>). The conductivity,  $\sigma$ , varies as the field strength and an exponential model was chosen for

this variation (roughly  $\sigma = \sigma_0 e^{-\beta[(B/B_0)^2 - 1]} + A$ ). The constant A depends on the initial and final value of  $\sigma$  and whether  $\sigma$  is chosen to be increasing or decreasing with time. Various values of  $\sigma_0$ , the initial value, and  $\sigma_1$ , the final value of  $\sigma$ , were taken in the calculation of (B). The model for  $\sigma(t)$  took the specific form:

$$\sigma(t) = \sigma_1 - (\sigma_1 - \sigma_0) e^{-\beta(e^{2\alpha t} - 1)} \quad (125)$$

(for  $\sigma$  increasing), and

$$\sigma(t) = (\sigma_0 - \sigma_1) e^{-\beta(e^{2\alpha t} - 1)} + \sigma_1$$

(for  $\sigma$  decreasing). The value of  $\beta$  was taken to be  $.2303 \times 10^{-3}$  corresponding to a 90% change between the initial and final values of  $\sigma$  during the half-microsecond interval under consideration.

### (3) Numerical Analysis

Trapezoidal integration was decided upon as a means of solving Eq. (123). If the problem were treated as a triple integral, it was felt that a single solution of (27) for  $n = 15$  up to  $t = 1/2 \mu\text{sec}$ , might require as much as 15 minutes of computer time (7094); therefore, the iterative nature of Eq. (27) was used to derive an algorithm allowing a stepped solution. The resulting technique required less than .0032 hr (approximately 0.2 min) solution time for  $n = 15$ .

To develop the required algorithm it is necessary to define the terms in Eq. (123) as follows:

$$I(t') = \int_0^{t'} \frac{B(t'')}{\sigma(t'')} \exp \left[ -\frac{n^2 \pi^2}{\mu_o r_o^2} \int_{t''}^{t'} \frac{dt'''}{\sigma(t''')} \right]$$

$$F(t', L) = \exp \left[ -\frac{n^2 \pi^2}{\mu_o r_o^2} \int_L^{t'} \frac{dt'''}{\sigma(t''')} \right].$$

Dividing the interval  $(-, t')$  into  $M$  increments of  $\Delta t$  width, application of the trapezoidal rule gives:

$$\begin{aligned} I(t') = & \left[ \frac{1}{2} \frac{B(0)}{\sigma(0)} F(t', 0) + \frac{B(\Delta t)}{\sigma(\Delta t)} F(t', \Delta t) + \frac{B(2\Delta t)}{\sigma(2\Delta t)} F(t', 2\Delta t) \right. \\ & + \frac{B(3\Delta t)}{\sigma(3\Delta t)} F(t', 3\Delta t) + \dots + \frac{B(t'-\Delta t)}{\sigma(t'-\Delta t)} F(t', t'-\Delta t) \\ & \left. + \frac{1}{2} \frac{B(t')}{\sigma(t')} F(t', t') \Delta t \right]. \end{aligned} \quad (126)$$

Similarly,

$$\begin{aligned} I(t'+\Delta t) = & \left[ \frac{1}{2} \frac{B(0)}{\sigma(0)} F(t'+\Delta t, 0) + \frac{B(\Delta t)}{\sigma(\Delta t)} F(t'+\Delta t, \Delta t) + \dots + \frac{B(t')}{\sigma(t')} F(t'+\Delta t, t') \right. \\ & \left. + \frac{1}{2} \frac{B(t'+\Delta t)}{\sigma(t'+\Delta t)} F(t'+\Delta t, t'+\Delta t) \right] \cdot \Delta t. \end{aligned} \quad (127)$$

Note that  $M \Delta t = t'$  and that  $F(X, X) = 1$  for all  $x$ . Defining  $A(t')$  as

$$A(t') = \exp \left[ -\frac{n^2 \pi^2}{\mu_o r_o^2} \frac{1}{2} \left( \frac{1}{\sigma(t')} + \frac{1}{\sigma(t'+\Delta t)} \right) \right] \quad (128)$$

it follows from the laws of exponential functions and addition of integration limits that

$$F(t'+\Delta t, L) = F(t', L) \cdot A(t') . \quad (129)$$

Therefore, from (126), (127), (128) and (129)

$$I(t'+\Delta t) = I(t') \cdot A(t') + \frac{1}{2} \left( \frac{B(t')}{\sigma(t')} A(t') + \frac{B(t'+\Delta t)}{\sigma(t'+\Delta t)} \right) \Delta t \quad (130)$$

Since, by definition of I,  $I(0) = 0$ , it is seen that (130) provides the step from  $I(t')$  to  $I(t'+t)$  and thus the induction step is established. Each value of  $I(t')$  is calculated from the previous value in the program and the computation is begun from  $I(0)$ . Thus, Eq. (123) can be integrated by merely operating on each preceding step by the operation given in Eq. (130). All of the functions in (130) are known functions and thus allow the induction step to be carried out in each instance.

Once Eq. (130) has been utilized, trapezoidal integration can be reapplied to the result to obtain the integration process for the final integral  $\left( \int_0^t \right)$  in Eq. (123) and the results can then be calculated for each value of  $n$  and summed to obtain the final result.

The program was written along the lines discussed above and a printout of  $W(t)$  (in joules) was made every  $.1 \mu\text{sec}$  up to and including  $.6 \mu\text{sec}$ . An option for using either an increasing or decreasing  $\sigma$  function was included as well as options for printouts of various program variables for checking purposes. The deposited energy required for the vaporization of the aluminum sphere was computed in the program and the ratio of the total energy deposited to the magnitude of required energy was printed out as "fraction" of vaporization energy. When this ratio exceeded unity, it could be assumed that vaporization of the aluminum was occurring.

#### (4) Checking the Program

To check the logic and numerics of the program and the validity of the algorithm, a special case was designed which could be integrated analytically by hand and compared with the program output. In particular  $W(t)$  was calculated for a constant magnetic intensity,  $B$ , and conductivity,  $\sigma$ . The expression that results (for  $B$  and  $\sigma$  constant) is

$$W(t) = \frac{6\pi r_o^2 B^2}{\mu_o^2} \sum_{n=1}^{\infty} \frac{1 - \exp \left[ -\frac{2n^2 \pi^2}{\mu_o r_o^2 \sigma} t \right]}{\frac{n^2 \pi^2}{\mu_o r_o^2}}. \quad (131)$$

For specific values of  $B, \sigma$  and the other constants, Eq. (131) was programmed and checked with the output of the general program (ENGINT). It was found that the values checked for most part to within 5% and rarely approached a 10% discrepancy. It was therefore concluded that within the numerical accuracy of roundoff error, the original program was essentially valid.

#### e. Results and Conclusions

The first series of runs after debugging showed very large vaporization ratios after the elapse of 0.5  $\mu$ sec (ranging from about 12 to 3000) for ten terms of the series, depending on the time-dependent behavior of the conductivity (whether increasing or decreasing) and on the size of the particle (particles were chosen at radii of .8, 1.5, and 2.5 mm).

The terms of the series did not show any tendency to converge even when 100 terms were calculated. This can be attributed to the very slow convergence rate for the type of series used. It has, however, been shown that in the limit as  $n$  becomes large the series approaches the behavior of a  $\sum \frac{1}{n^2}$  type of series. For this reason, it is possible that as many as several thousand terms may be needed before numerical convergence can be achieved. Since the series does converge (in the rigorous meaning of the term) the slowness of convergence indicates the model predicts that the magnetic field has diffused a small distance into the sphere. This combined with the high energy deposition means that the model predicts surface vaporization. Vapor conductivity is much less than metal conductivity until electron volt temperatures are reached, but the model is based on constant conductivity throughout the sphere. Thus, it breaks down, indicating that the magnetic field diffusion process is highly nonlinear, and that a nonlinear model will be required for definitive calculations.

### 3. Non-Linear Analysis

#### a. Statement of Problem

The non-linear analysis was performed on the diffusion of the magnetic flux into a cylinder of the same diameter as the sphere. This model was sufficiently similar to provide an accurate estimate of projectile vaporization.

The problem consists of an axial magnetic flux which initially is uniformly distributed both internally and external to an infinitely long aluminum cylinder of small diameter (1 to 2 mm). The concentric volume surrounding the cylinder is rapidly compressed so that the flux external to the cylinder increases without loss. The magnetic field strength-time history was taken from experimental measurements. For purposes of computation, it was closely approximated by two exponentiating functions, the first slow for a short period, followed by a fast exponentiation.

The physical boundary conditions at the surface require that the axial magnetic field be the same internal and external to the surface. Thus, the magnetic field tends to increase just inside the surface at the same rate as in the volume external to the cylinder. As the magnetic field increases at the surface, the flux tends to diffuse into the metal at a rate which is relatively slow compared to the rate of change at the surface. Thus, the metal has a capacitive effect with respect to magnetic flux in the same physical sense that the metal has a capacitive effect for heat, and as will be shown, the mathematical description turns out to have the same basic form as thermal diffusion. As the axial magnetic flux diffuses into the metal an electric field is induced in a circumferential direction. This field results in an electric current which is dissipated by the material resistance. This results in heating of the

material. The heat deposition has the same radial distribution as the current that is generating it and under normal conditions the heat would diffuse in the same manner as the magnetic flux. However, in the case of the heat, the time of the transient is so short that no appreciable diffusion can occur and the heating results in an increase in temperature only in the local area where the heat deposition occurs.\*

The material properties which affect the distribution and diffusion are the magnetic permeability,  $\mu$ , the specific heat,  $c_p$ , and the resistivity,  $\eta$ . The material is non-magnetic, has a permeability equivalent to a vacuum and is considered to be a constant in these problems. The specific heat and resistivity are both functions of temperature and thus have a spatial distribution associated with the temperature distribution. Dependence of these properties on other variables such as pressure or magnetic field strength were not taken into account initially.

#### b. Method of Calculation

The requirements of the problem are the determination of the current and temperature, spatial and time dependent, distribution in the cylinder. The electro-dynamic character of the cylinder can be described by Maxwell's equations,

$$\nabla \cdot \overline{D} = \rho = 0 \quad (1)$$

$$\nabla \cdot \overline{B} = 0 \quad (2)$$

$$\nabla \times \overline{E} = - \frac{\partial \overline{B}}{\partial t} \quad (3)$$

---

\* Typical heat deposition occurs at  $10^4$  times the rate of removal by thermal diffusion.

$$\nabla \times \overline{H} = \overline{J} + \frac{\partial \overline{D}}{\partial t} = \overline{J} \quad (4)$$

Ohms Law,

$$\overline{E} = \eta \overline{J} \quad (132)$$

and the permeability equation,

$$\overline{B} = \mu \overline{H} \quad (133)$$

The thermal characteristics of the load are expressed by

$$\rho c_p \frac{\partial T}{\partial t} = \nabla \cdot (k \nabla T) + \eta J^2 \quad (134)$$

The first problem is to evolve an expression for the spatial and time dependent distribution of the magnetic field vector  $\overline{H}$ . This is accomplished by taking the curl of Eq. (14) and then successively substituting in Eqs. (132), (133) and (134), and expanding as follows:

$$\nabla \times \nabla \times \overline{H} = \nabla \times \overline{J} = \nabla \times \left( \frac{1}{\eta} \overline{E} \right)$$

$$\nabla(\nabla \cdot \overline{H}) - \nabla^2 \overline{H} = \nabla \left( \frac{1}{\eta} \right) \times \overline{E} + \left( \frac{1}{\eta} \right) \nabla \times \overline{E}$$

$$\nabla(\nabla \cdot \overline{H}) - \nabla^2 \overline{H} = \nabla \left( \frac{1}{\eta} \right) \times \left( \eta [\nabla \times \overline{H}] \right) - \frac{\mu}{\eta} \frac{\partial \overline{H}}{\partial t}$$

Now the magnetic field vector has only one component,  $\overline{H}_z(r)$  and the scalar resistivity is also a function,  $\eta(r)$ , varying only in the radial direction. Inserting these components we find that



$$\nabla \cdot \bar{H} = 0 \quad \text{and} \quad \nabla(\nabla \cdot \bar{H}) = 0$$

$$\nabla^2 \bar{H} = \bar{z} \left[ \frac{1}{r} \frac{\partial}{\partial r} \left( r \frac{\partial H_z(r)}{\partial r} \right) \right]$$

$$\nabla \left( \frac{1}{\eta} \right) \alpha(\eta[\nabla \times \bar{H}]) = \bar{z} \left[ \left( \frac{\partial \left( \frac{1}{\eta(r)} \right)}{\partial r} \right) \eta(r) \left( - \frac{\partial H_z(r)}{\partial r} \right) \right]$$

$$\frac{\mu}{\eta} \frac{\partial \bar{H}}{\partial r} = \bar{z} \left[ \frac{\mu}{\eta(r)} \left( \frac{\partial H_z(r)}{\partial r} \right) \right]$$

where  $\bar{z}$  is the unit vector in the  $z$  direction. Since the vector components are all in the same direction, the following scalar equation can be formed wherein  $H_z(r)$  is written as  $H(r)$ .

$$\frac{\partial H(r)}{\partial t} = \frac{\eta(r)}{\mu} \left[ \frac{1}{r} \frac{\partial}{\partial r} \left( r \frac{\partial H(r)}{\partial r} \right) - \eta(r) \left( \frac{\partial \left( \frac{1}{\eta(r)} \right)}{\partial r} \right) \left( \frac{\partial H(r)}{\partial r} \right) \right] \quad (135)$$

The boundary conditions on the equation are that the radial gradient of  $H(0)$  equal zero and that  $H(r)$  is equal to a known, time-varying magnetic field vector. Equation (135) can be rewritten, expanding the spatial distribution in a finite difference form for  $K + 1$  equally thick radial segments, i.e.,  $0 \leq k \leq K$ .

$$\begin{aligned} \left. \frac{\partial H(r)}{\partial t} \right|_k &= \frac{\eta_k}{\mu} \left[ \frac{1}{r_k} \left[ \left( \frac{2r_k + \Delta r}{2\Delta r^2} \right) (H_{k+1} - H_k) + \left( \frac{2r_k - \Delta r}{2\Delta r^2} \right) (H_{k-1} - H_k) \right] \right. \\ &\quad \left. - \eta_k \left( \frac{H_{k+1} - H_{k-1}}{2\Delta r} \right) \left( \frac{(1/\eta)_{k+1} - (1/\eta)_{k-1}}{2\Delta r} \right) \right] \quad 1 \leq k \leq K \quad (136a) \end{aligned}$$

$$H_0 = H_1 \quad (136b)$$

$$H_k = f(t) \quad (136c)$$

where  $f(t)$  is the known time variation of the magnetic field vector external to the cylinder.

The equations describing the temperature distribution are obtained by writing Eq. (134) in a finite difference form. Before doing this, however, it should be pointed out that this transient process is quite fast (on the order of  $2 \mu\text{sec}$ ). Thermal diffusion thus has a very limited effect, i.e.,  $\nabla \cdot (k \nabla T) \ll J^2$  and Eq. (134) can be written as

$$\rho c_p \frac{\partial T}{\partial t} = \eta J^2$$

or in finite difference form as

$$\left. \frac{dT}{dt} \right|_k = \left( \frac{1}{\rho c_p} \right)_k (\eta i)_k i_k^0 \quad k = 0, 1, 2, \dots, K \quad (137)$$

In this equation,  $c_p$  is a function of the temperature of the zone.

The current can be evaluated directly from Eq. (4) by noting that the currents are limited to the circumferential direction and are only a function of radius so that Eq. (4) can be expanded to

$$i(r) = \frac{\partial H(r)}{\partial r} \quad (138)$$

or in finite difference form

$$i_k = \frac{H_{k+1} - H_{k-1}}{2\Delta r} \quad 1 \leq k < K \quad (139a)$$

$$i_k = \frac{H_k - H_{k-1}}{\Delta r} \quad (139b)$$

$$i_0 = 0 \quad (139c)$$

In summary, the vector equations have been reduced to a set of ordinary, non-linear, first-order, coupled, differential equations in the single independent variable, time, and a number of algebraic equations which are used to determine the nodal currents.

This set of equations is compatible, and can be solved using an integrating scheme such as the Adams routine. A computer code, MIDAS,<sup>2</sup> was used to solve these equations. The code is designed to provide a solution to a general set of equations of the type encountered in this problem, using a variable time step, fifth order, predict-correct, integration routine.<sup>3</sup> The time step is determined based on an error criteria for the dependent variables.

A set of problems has been run on a 1- and 2-mm diameter aluminum rod. These computations have used 20 equal radial increments and temperature dependent specific heat and resistivity properties. These properties have been approximated by the following linear equations.

$$\eta(T) = 2.824 \times 10^{-8} + 0.011 \times 10^{-8} T \quad (140a)$$

$$\frac{1}{\rho c_p}(T) = 0.33 \times 10^{-6} - 1.0 \times 10^{-10} T \quad (140b)$$

The driving magnetic flux has been simulated by exponentiation at a rate of  $1.72 \times 10^6$ /sec during the first  $2.1 \times 10^{-6}$  sec and then at a rate of  $3.0 \times 10^6$ /sec until the problem was terminated. Initial magnetic flux of

---

<sup>2</sup>SEG-TDR-64-1. "MIDAS Programming Guide," R. T. Harnett, F. J. Sansom, L. M. Warshawsky, Project 1523, Task No. 152304, January 1964.

<sup>3</sup>W. E. Milne and R. R. Reynolds, "Fifth Order Methods for the Numerical Solution of Ordinary Differential Equations," Journal of the Association for Computing Machinery, Vol. 9, No. 1, p. 64, January 1962.

$4 \times 10^4$  gauss was used and the driving flux distribution was a simulation of experiment MGA-15. Figure 1 shows the driving magnetic flux as a function of time.

The problems were run so that the temperature of the node would be clamped when that node reached its vaporization temperature ( $2057^\circ\text{C}$ ). Heat generation was allowed to continue until vaporization had occurred to some extent. In these problems the outer ten nodes were allowed to vaporize and the vaporization of the tenth node caused the termination of the problem.

#### c. Results

Figures 2 through 5 show the radial variation of magnetic flux and temperature for various times for both the 1- and 2-mm cylinder. In both cases, vaporization starts to occur in slightly over  $2 \mu\text{sec}$  or about 1.5 Mgauss. The results of the problem after the beginning of vaporization are no better defined than the material properties in that condition.

### 4. Correction for High Magnetic Field Effects

#### a. Description

The calculations described above on 1- and 2-mm diameter aluminum cylinders utilized a linear temperature dependence for the resistivity, i.e.,  $\eta(T) = a + bT$ . Subsequent to this the project was informed of experiments at the Sandia Corporation, Albuquerque, concerning the effect of a 1-Mgauss magnetic field on the conductivity of aluminum.<sup>4</sup> This indicated that the temperature coefficient,  $b$ , is a function of the magnetic field strength. Although uncertainties were expressed in the results, their measurements showed  $b$  decreasing by a factor of 33 when

---

<sup>4</sup>J. C. Crawford, Sandia Laboratory, Private communication.

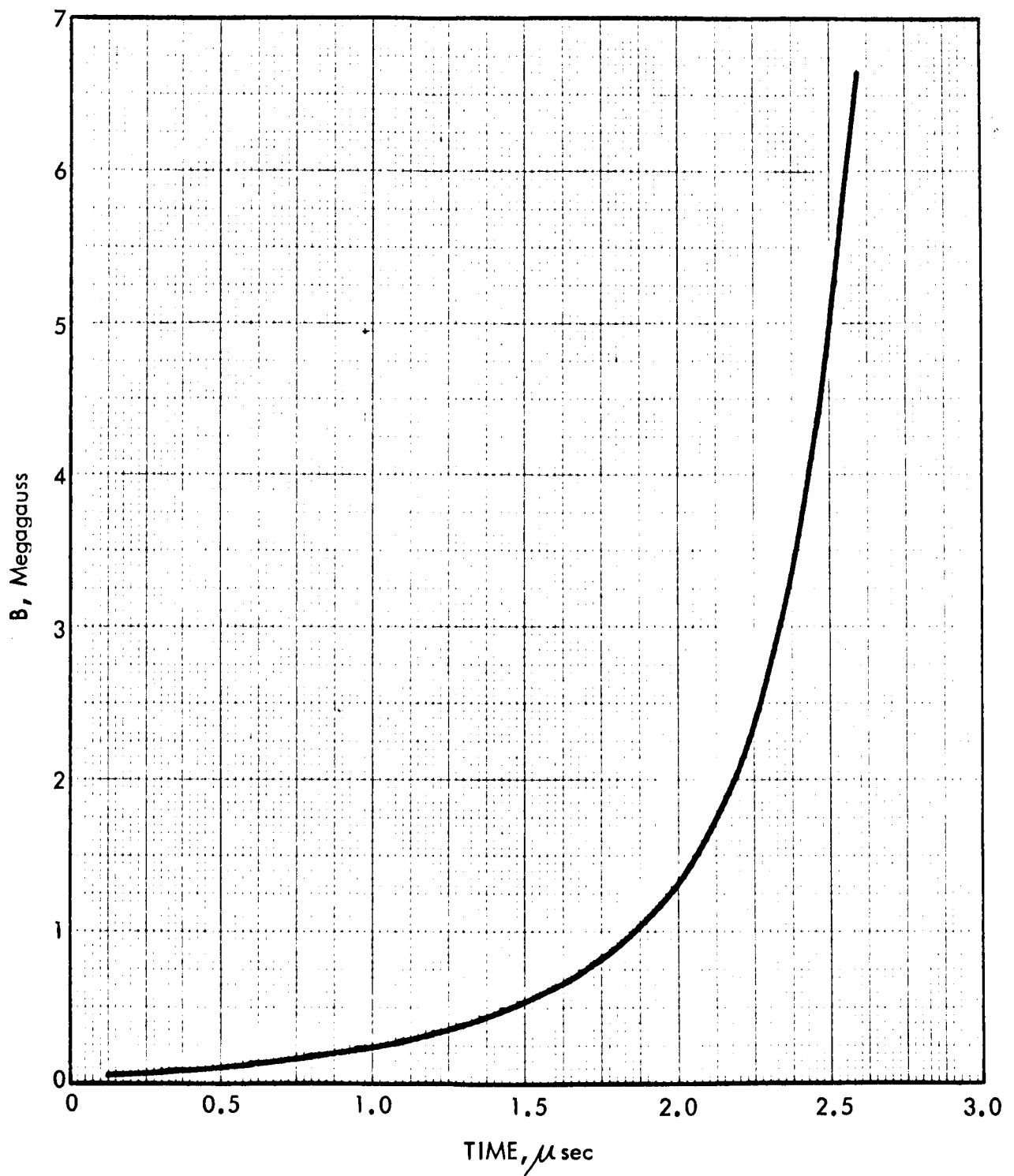


FIGURE 1. SIMULATED DRIVE FIELD FOR DIFFUSION AND HEATING CALCULATIONS (Applied in outer computation zone)

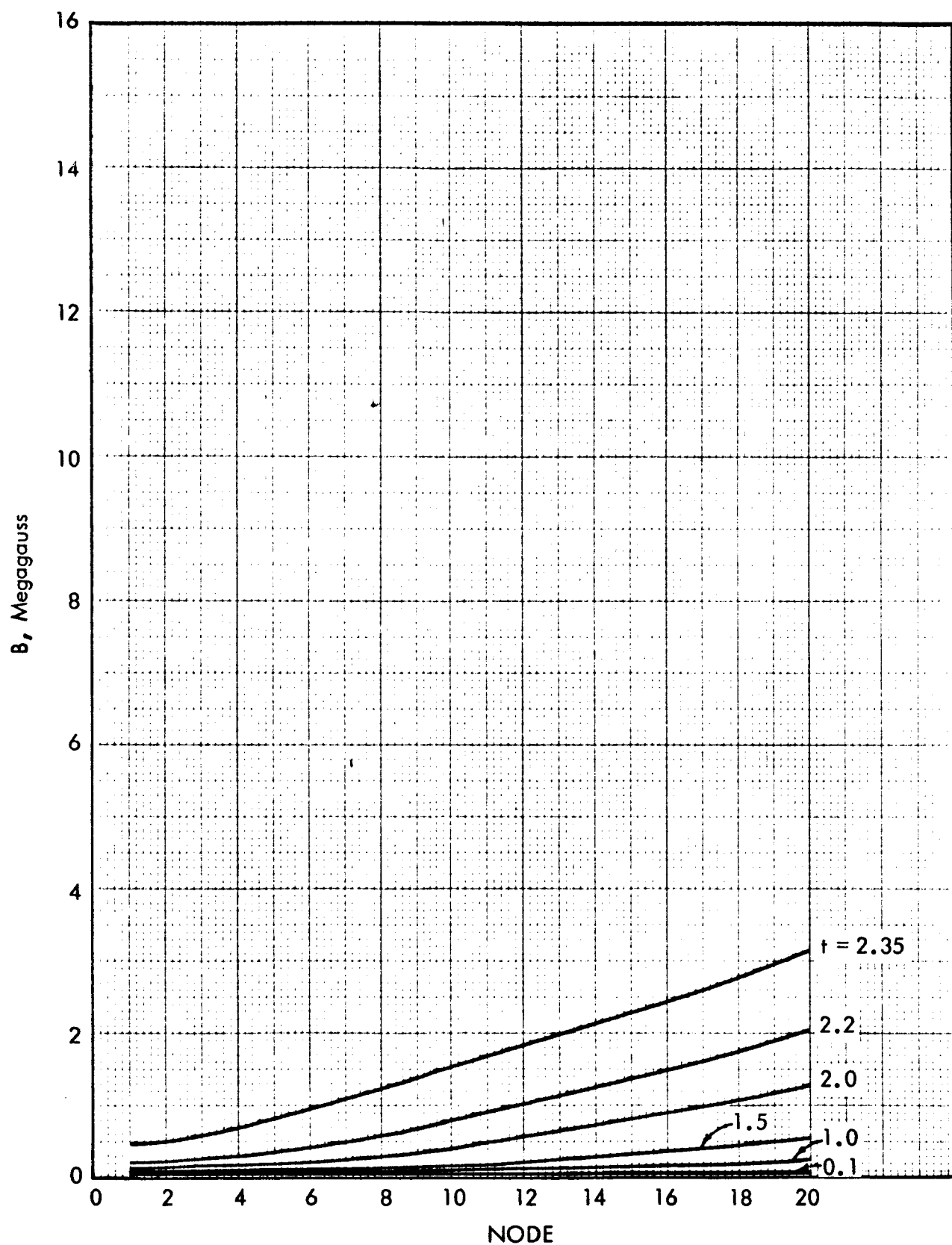


FIGURE 2. MAGNETIC FIELD DIFFUSION INTO 1 mm DIAMETER ALUMINUM CYLINDER,  $\eta = a + bT$

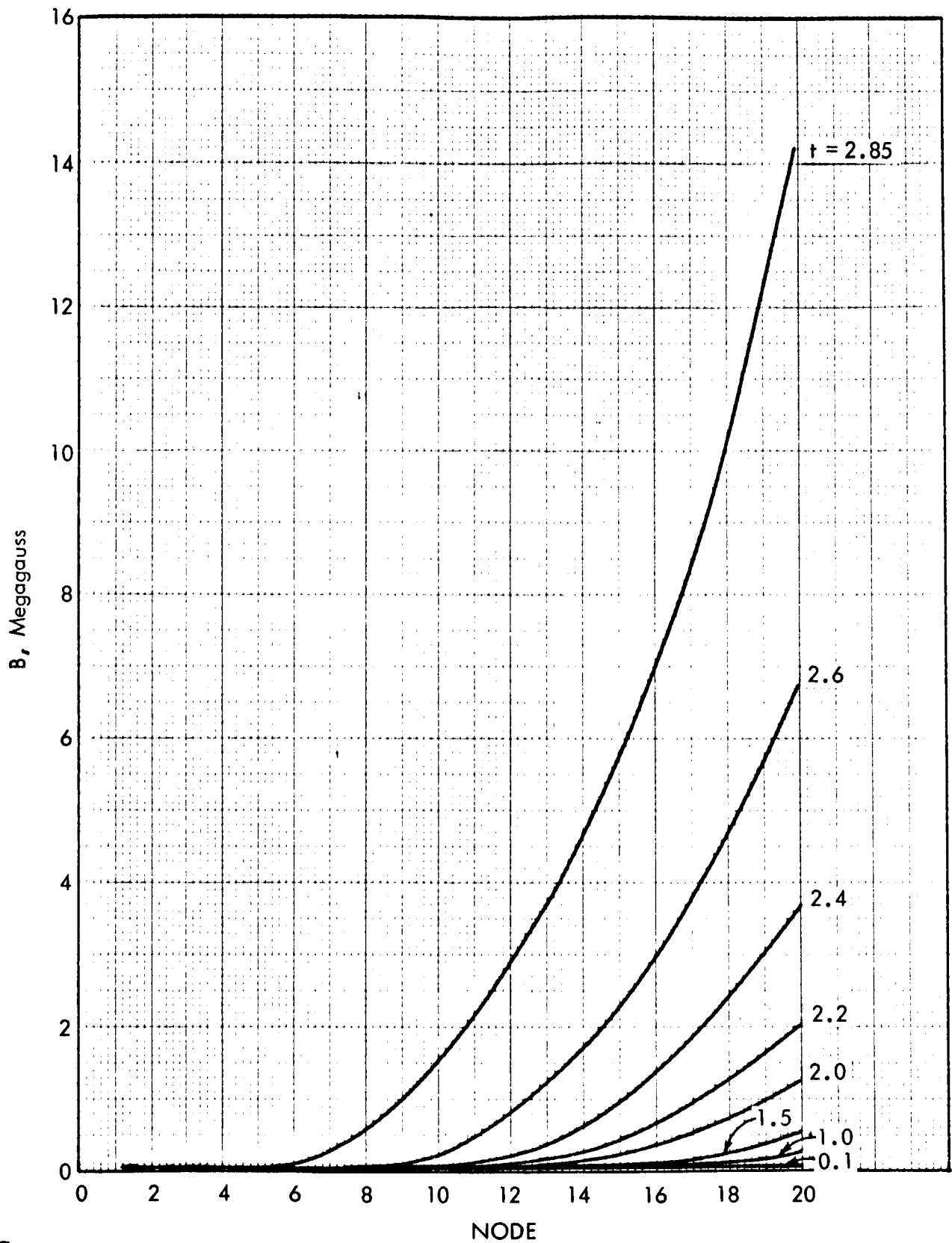


FIGURE 3. MAGNETIC FIELD DIFFUSION INTO 2mm DIAMETER ALUMINUM CYLINDER,  $\eta = a + bT$

35.1-66-073

35.1-66-074

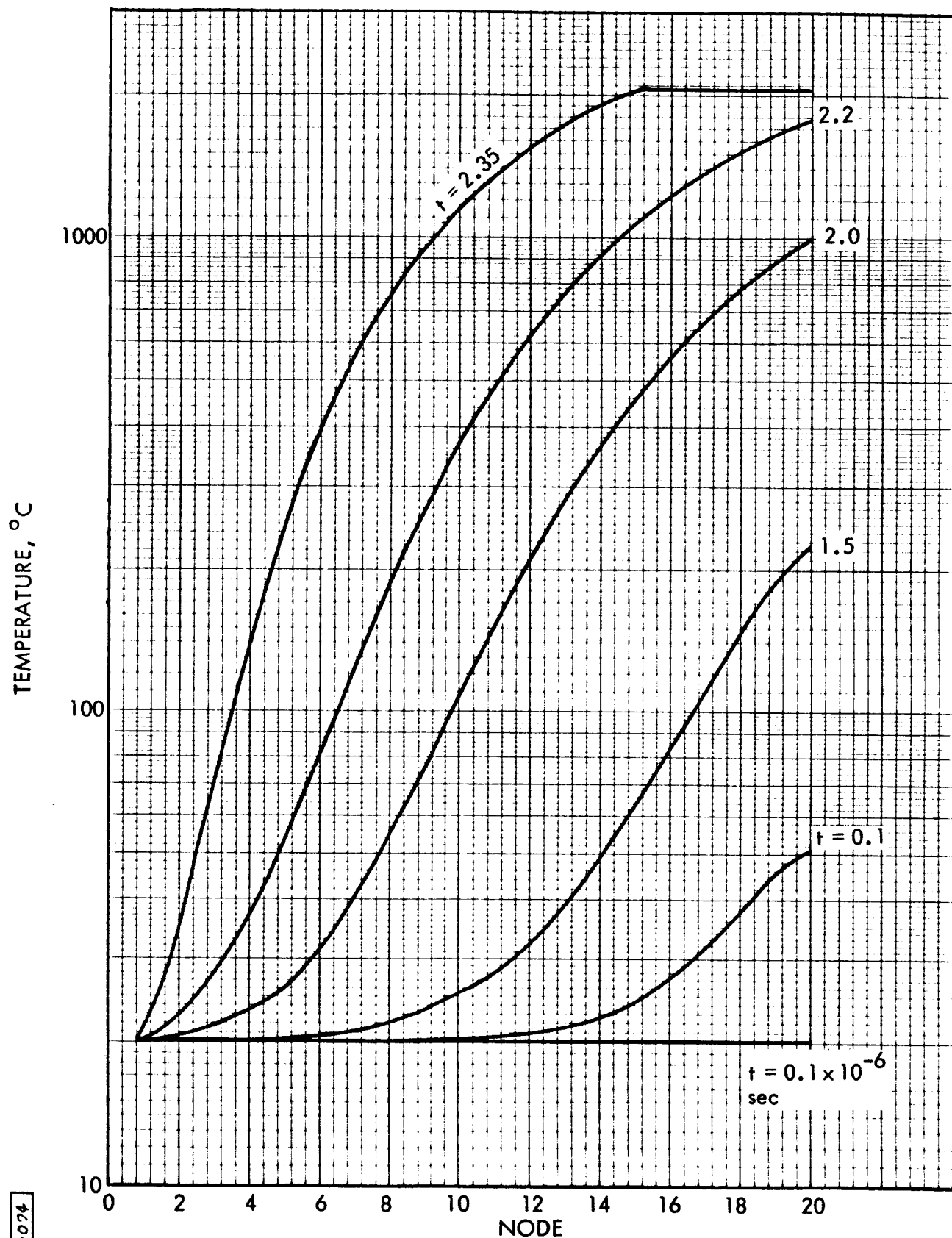


FIGURE 4. MAGNETIC HEATING OF 1mm DIAMETER ALUMINUM CYLINDER,  $\eta = a + bT$



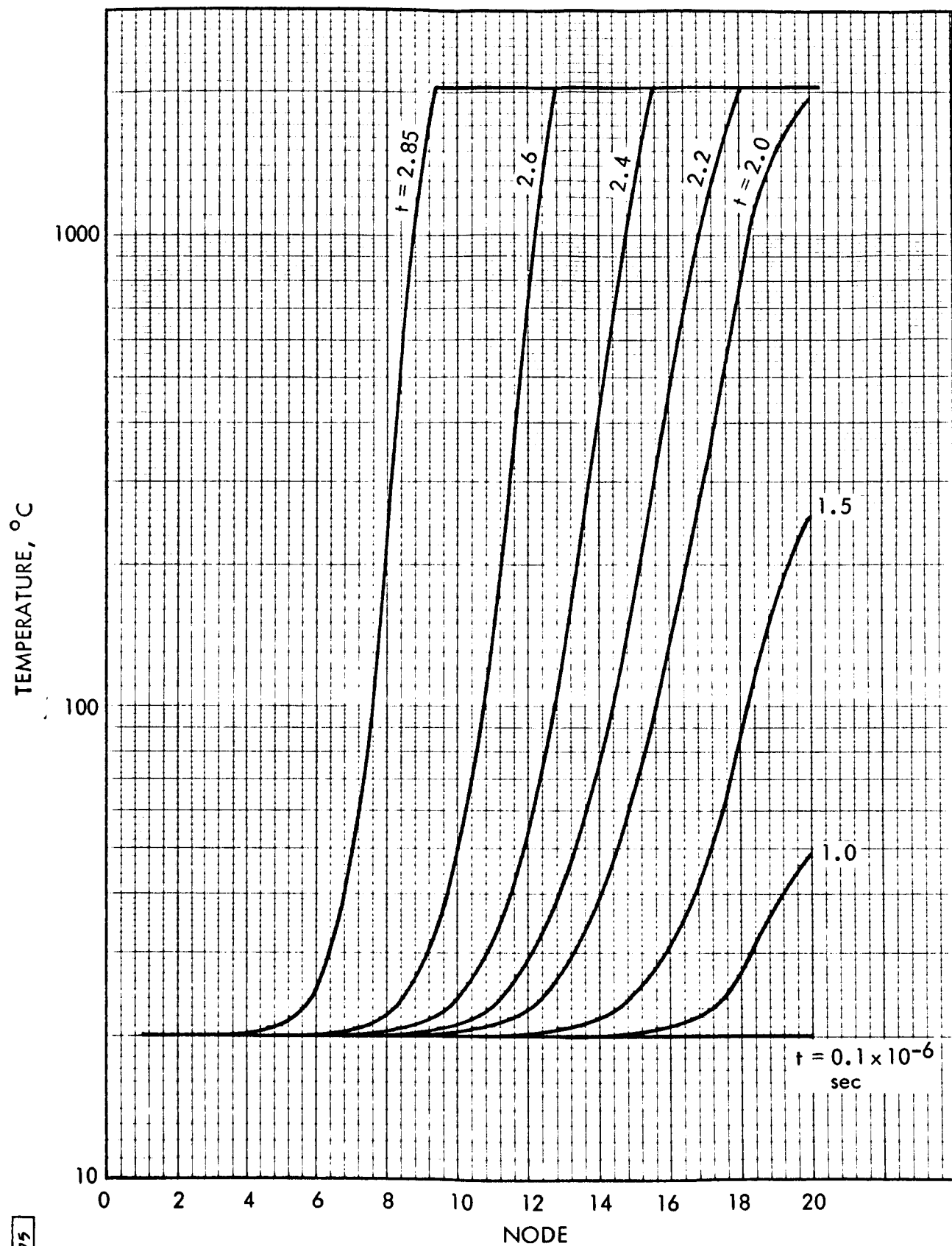


FIGURE 5. MAGNETIC HEATING OF 2mm DIAMETER ALUMINUM CYLINDER,  $\eta = a + bT$

raising the field to 1 Mgauss. The presence of this type of effect has been suspected for some time, but this experiment, to our knowledge, has been the first attempt to measure it.

To test out the results of the decrease in  $b$ , the problems were rerun using the MIMIC<sup>5</sup> computer program. These were done using a cylinder diameter of 1.5 mm. The MIMIC code permitted the resistivity,  $\eta$  to be expressed as a function of two variables,  $B$  and  $T$ . The same driving field profile was used.

For purposes of comparison, this set of problems was run with the following function of  $\eta$ .

$$(a) \quad \eta(T) = a + bT$$

$$(b) \quad \eta(T) = a + \frac{b}{33}T$$

$$(c) \quad \eta(B, T) = \frac{a + bT}{1 + 32B}$$

$$(d) \quad \eta(B, T) = \frac{a + bT}{1 + 32B^2}$$

}  $B$  in megagauss

No fundamental theory of the high- $B$  conductivity phenomenon is known to AGN. It appears, however, that at least magnetic field strength, electric field strength, and pressure are involved. The experimental data available are in terms of magnetic field strength. Empirically, it seemed reasonable that a field-dependent resistivity function could vary inversely as  $B$ , to a first approximation; thus, Eq. (c) above. Since static high pressure experiments have shown reduced resistivity, a magnetic field pressure dependence was considered. The effect of this is rather drastic, and probably unrealistic, but for comparison Eq. (d) was run. Equations (c)

---

<sup>5</sup>H. E. Petersen and F. J. Sansom, MIMIC--A Digital Simulator Program, SESCO Internal Memo 65-12, May 1965.

and (d) are arranged to coincide with the experimental measurement made by Crawford.

b. Results

The results of the calculations are shown in Figs. 6 through 13. They follow the expected trend. It is recognized that the functions describing the B dependence of  $\eta$  are crude. Qualitatively, however, it is apparent that this phenomenon causes order-of-magnitude reductions of the magnetic field penetration and heating of small aluminum conductors. Crawford's experiments also indicated an increase of specific heat with B. No attempt was made to include this, thus causing the results to be more pessimistic than they would be otherwise.

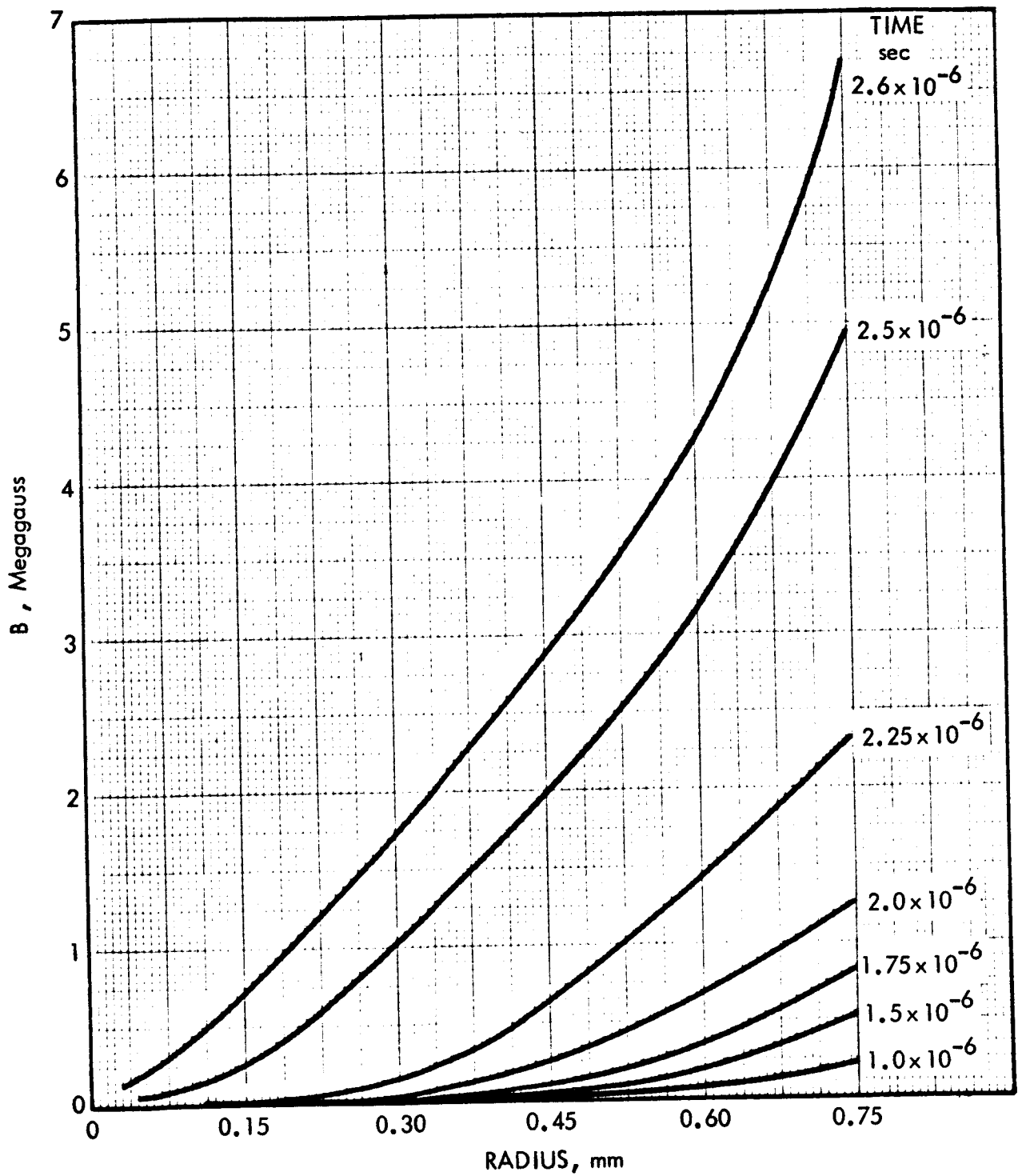


FIGURE 6. MAGNETIC FIELD DIFFUSION INTO 1.5mm DIAMETER ALUMINUM CYLINDER,  $\eta = a + bT$

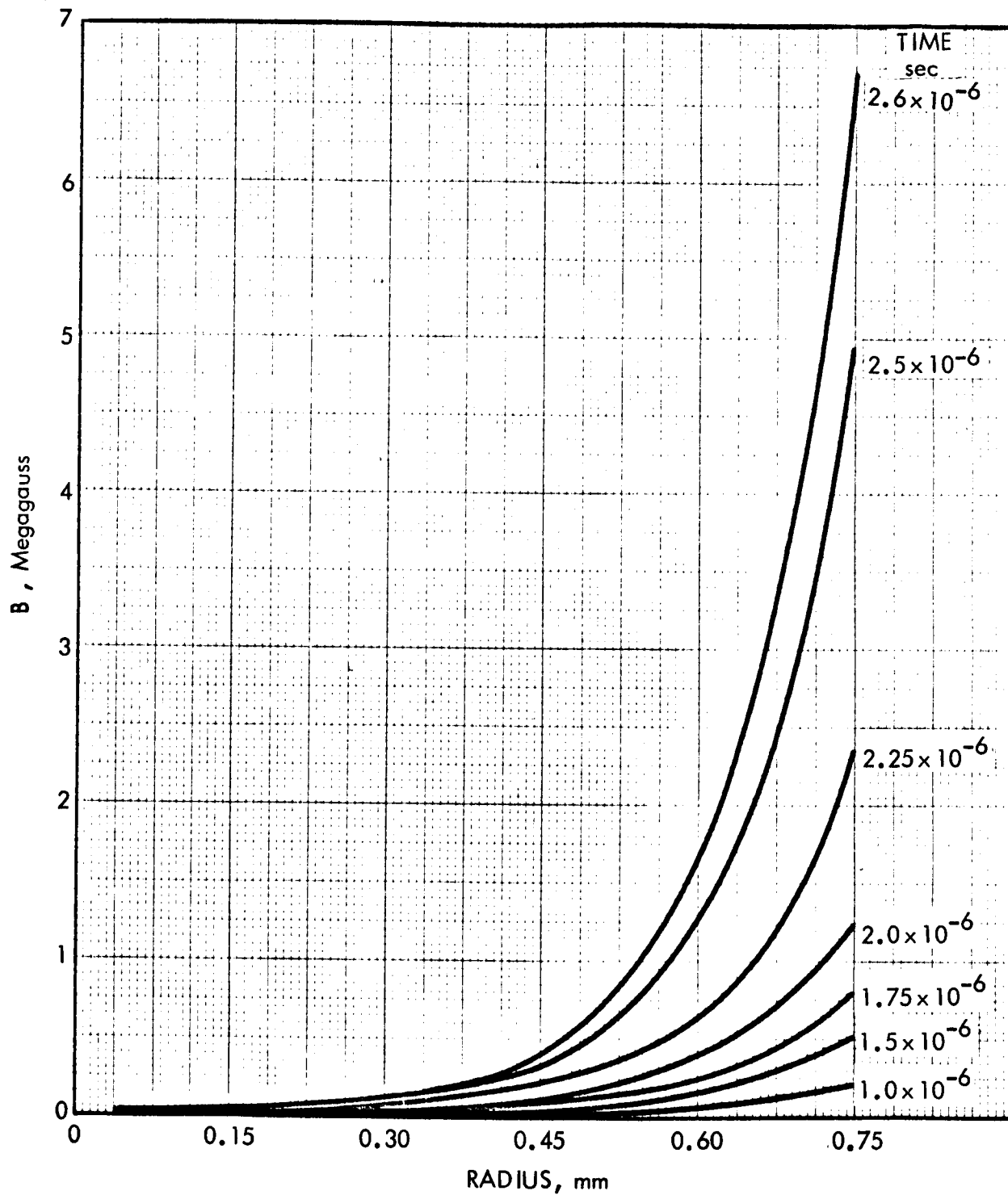


FIGURE 7. MAGNETIC FIELD DIFFUSION INTO 1.5 mm DIAMETER ALUMINUM CYLINDER,  $\eta = a + \frac{b}{33} T$

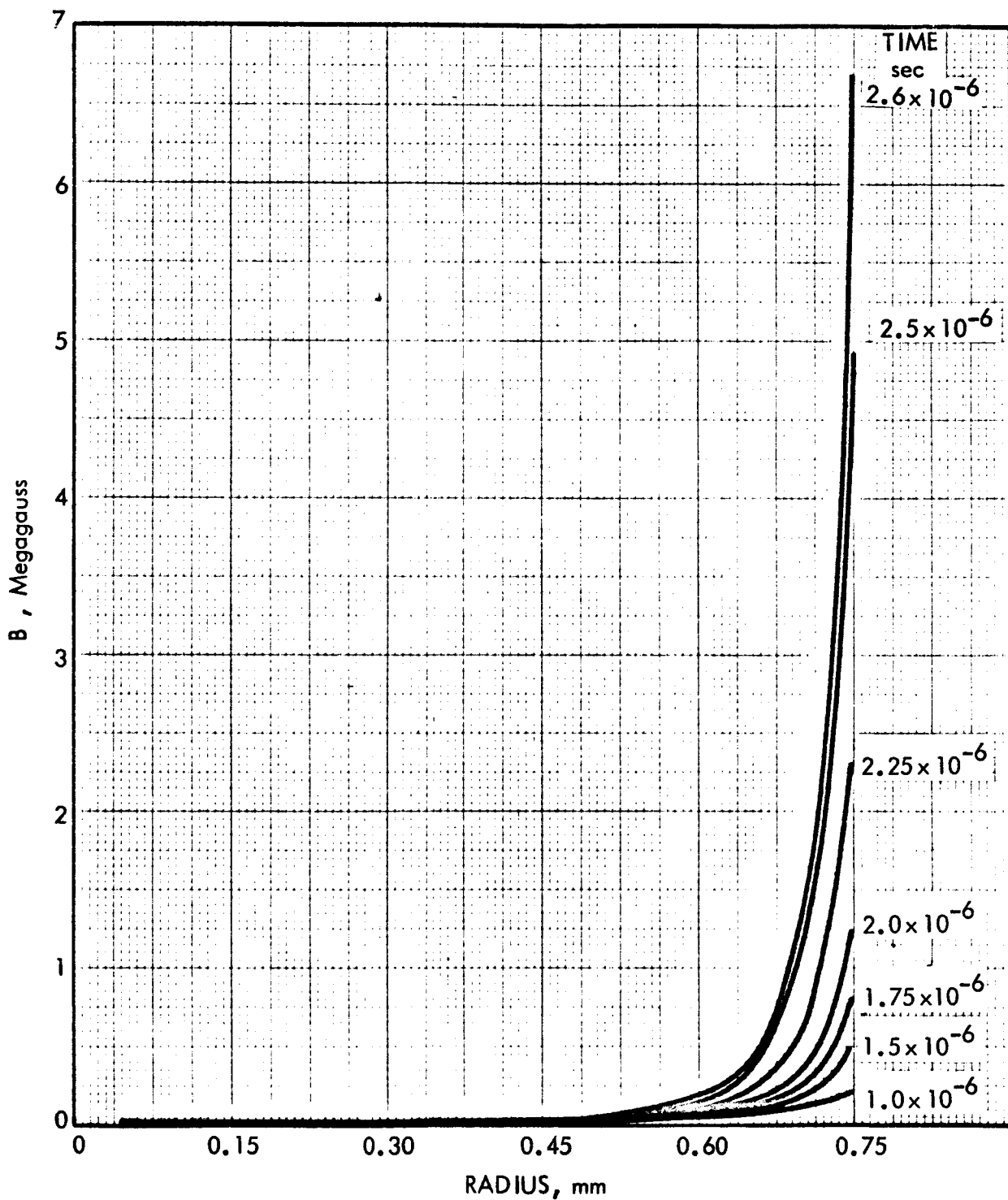


FIGURE 8. MAGNETIC FIELD DIFFUSION INTO 1.5mm DIAMETER ALUMINUM CYLINDER,  $\eta = \frac{a+bT}{1+32B}$

351-66-078

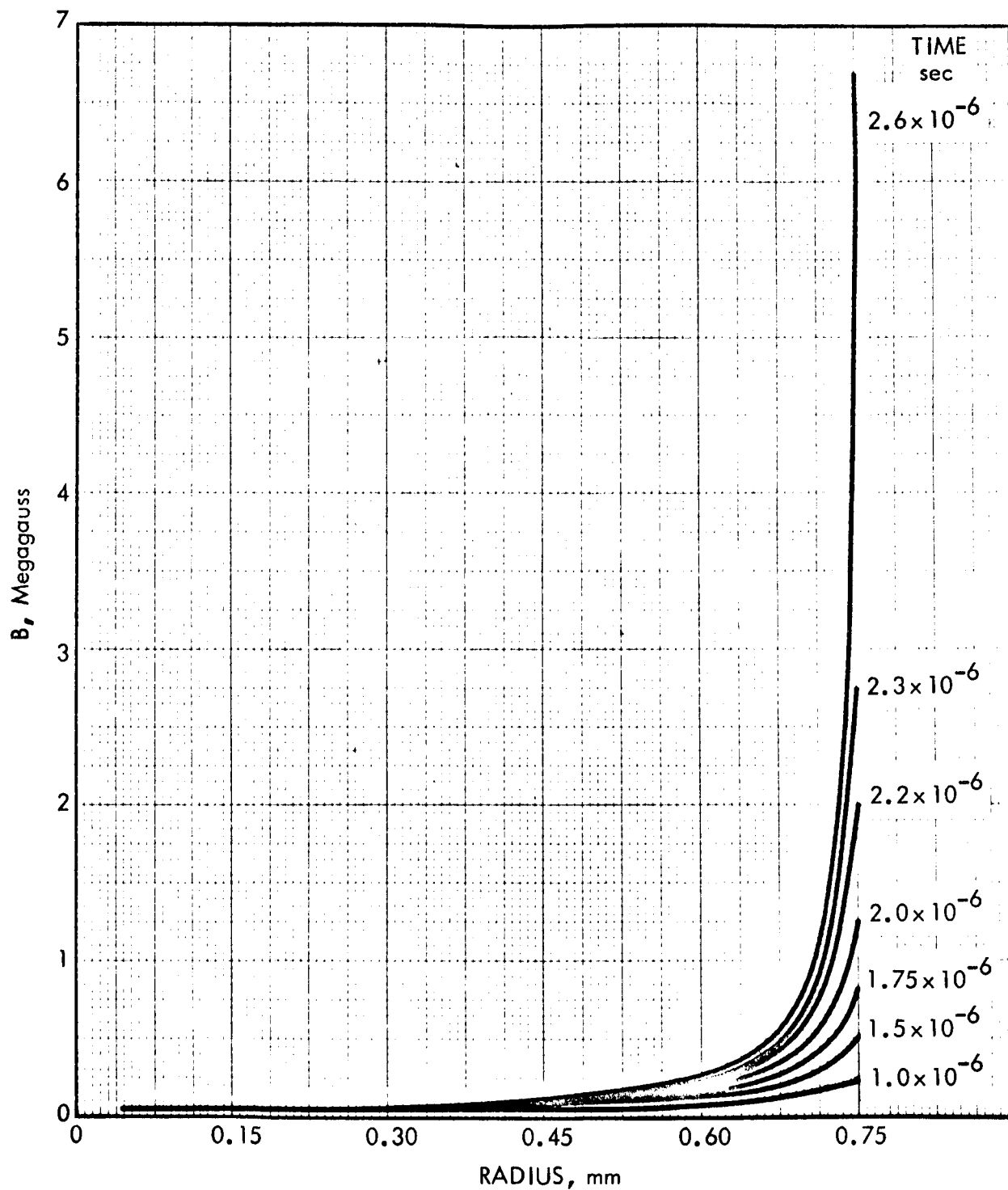


FIGURE 9. MAGNETIC FIELD DIFFUSION INTO 1.5mm DIAMETER ALUMINUM CYLINDER,  $\eta = \frac{a+bT}{1+32B^2}$

351-66-079

35.1-66-080

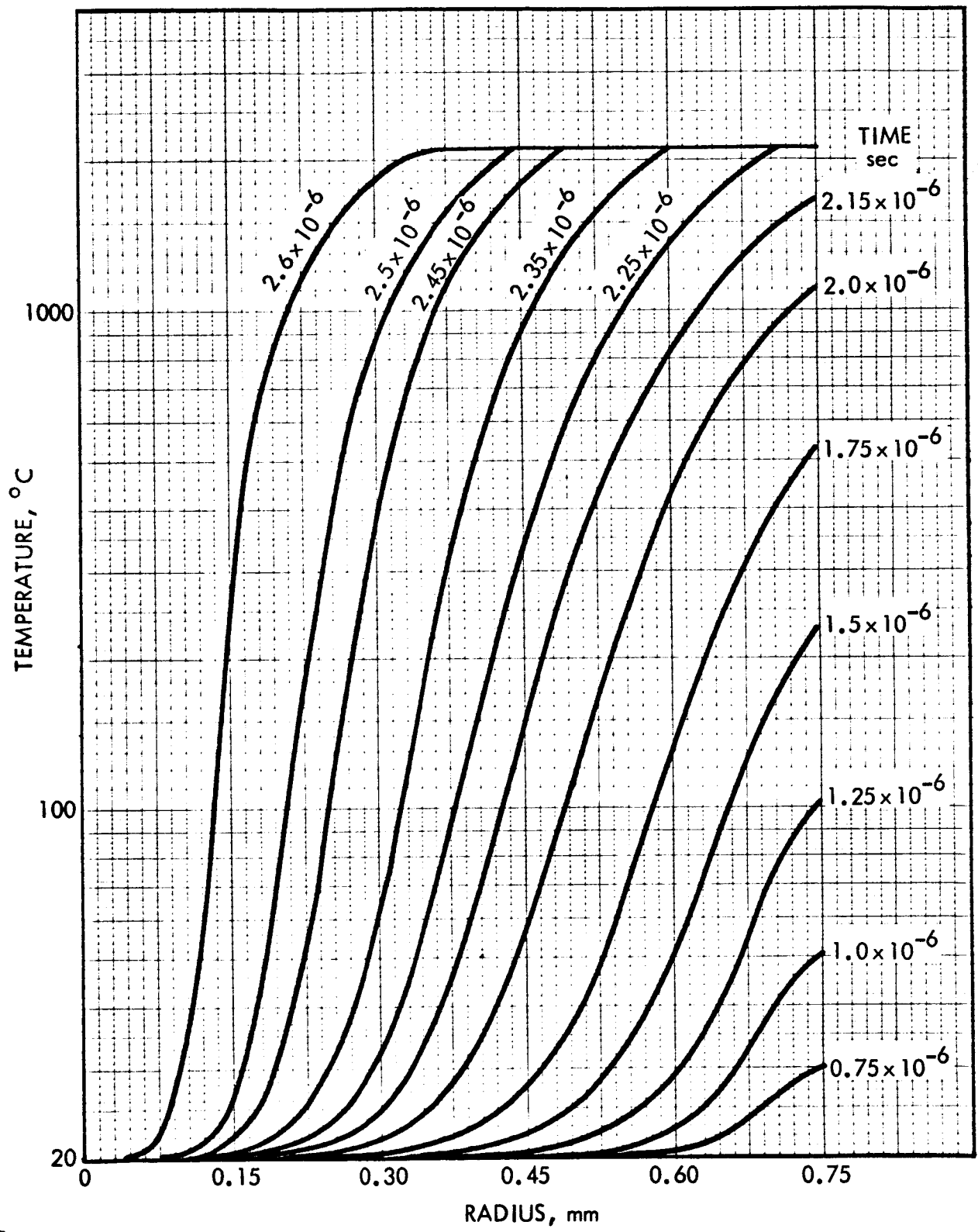


FIGURE 10. MAGNETIC HEATING OF 1.5 mm DIAMETER ALUMINUM CYLINDER,  $\eta = a + bT$



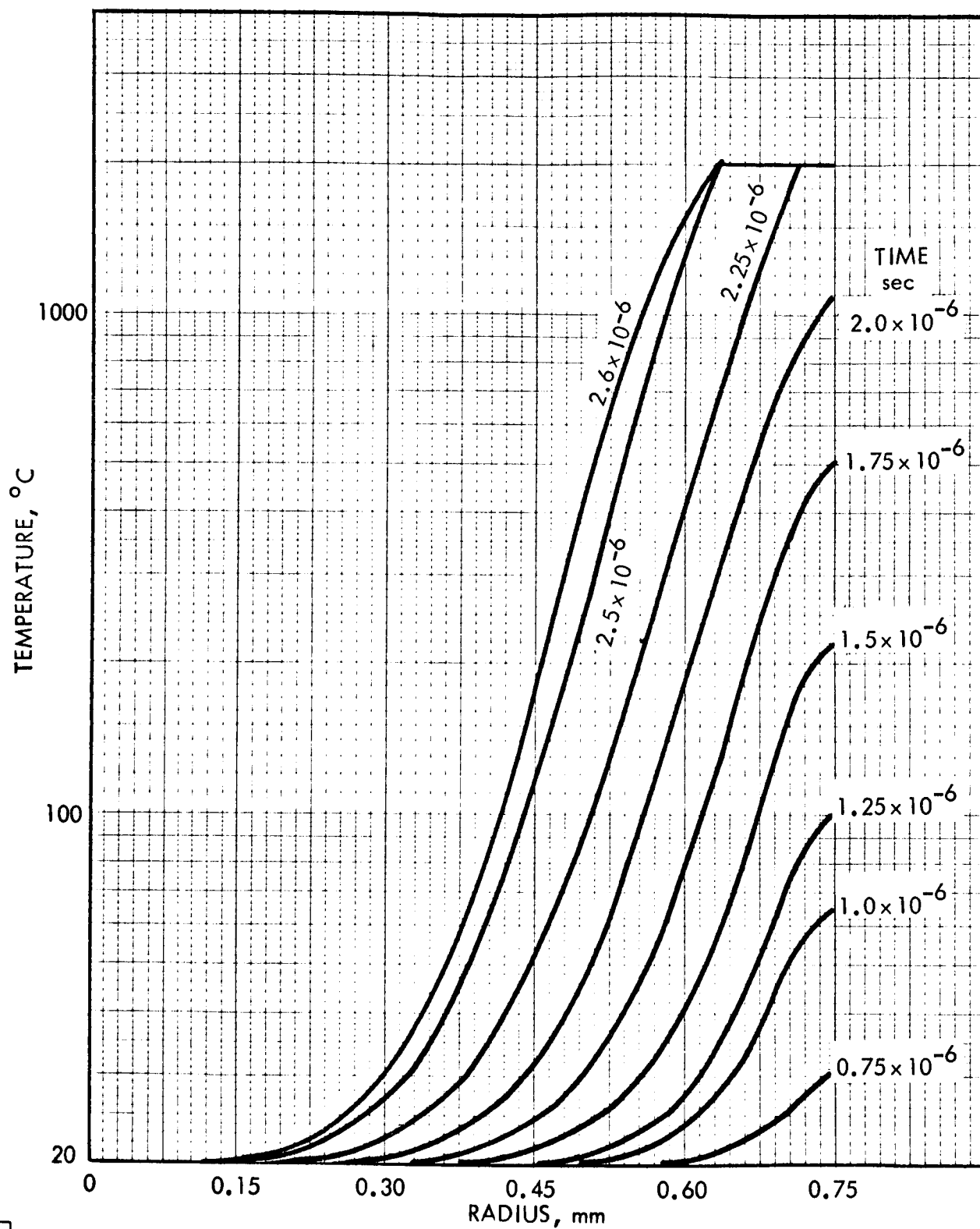


FIGURE 11. MAGNETIC HEATING OF 1.5 mm DIAMETER ALUMINUM CYLINDER,  $\eta = a + \frac{b}{33}T$

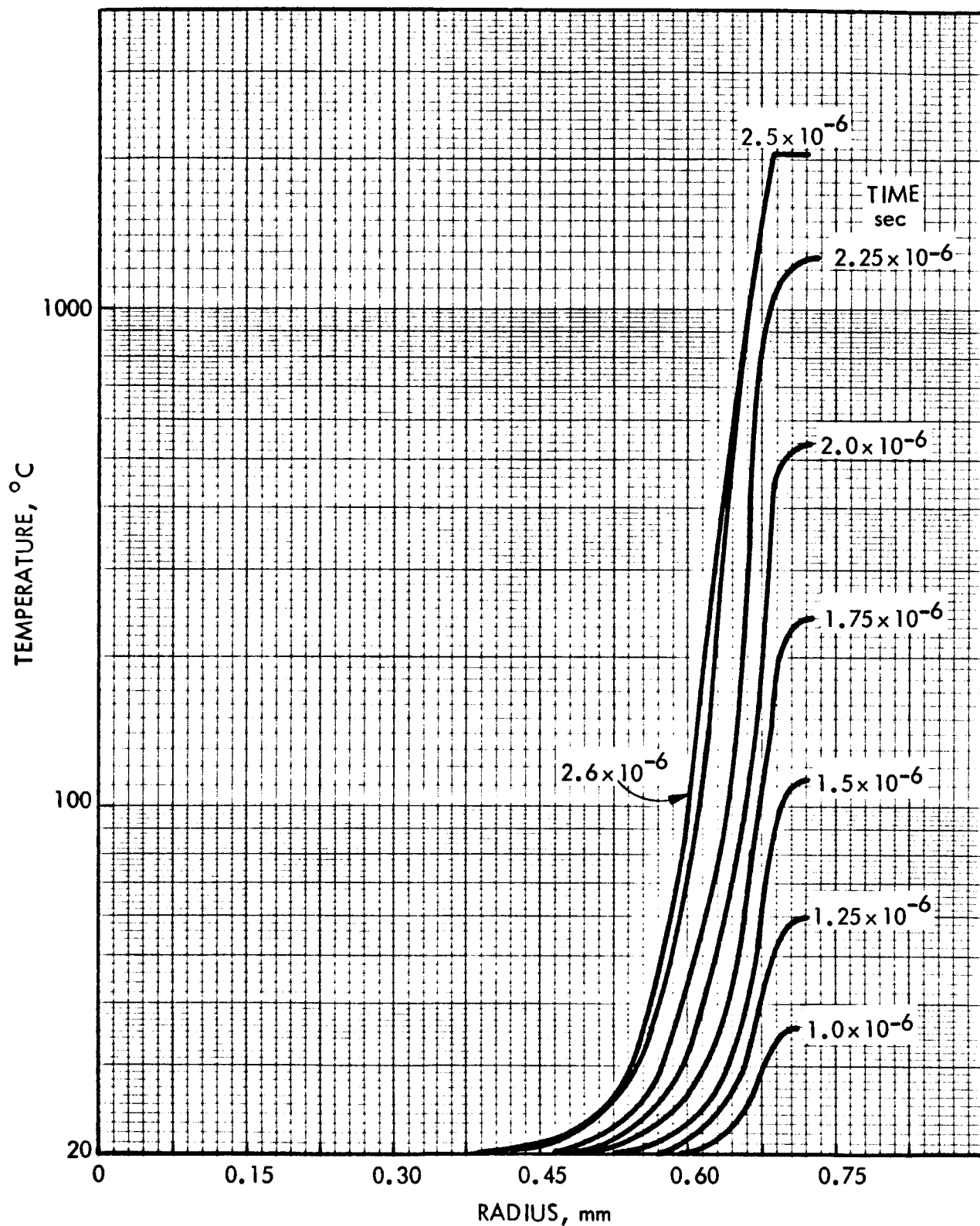


FIGURE 12. MAGNETIC HEATING OF 1.5mm DIAMETER ALUMINUM CYLINDER,  $\eta = \frac{a+bT}{1+32B}$

35.1-66-082

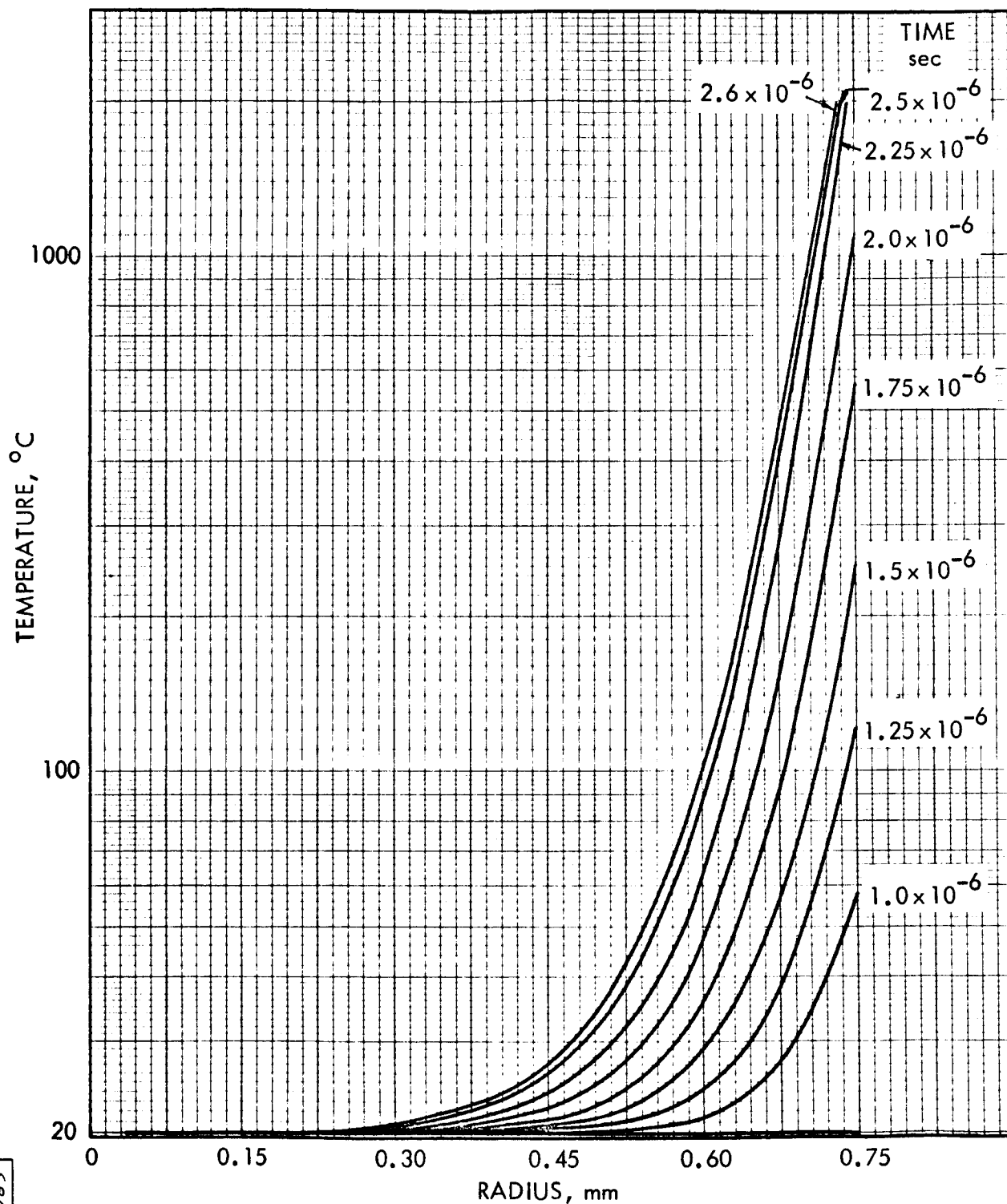


FIGURE 13. MAGNETIC HEATING OF 1.5 mm DIAMETER ALUMINUM CYLINDER,  $\eta = \frac{a + b T}{1 + 32 B^2}$

## B. FLUX CONCENTRATOR HYDRODYNAMICS

### 1. Introduction

Another problem which was treated analytically was motion of the flux concentrator segments. Peak magnetic pressures up to a few megabars are experienced by the flux concentrator, followed by impact of the armature after final collapse of the field. The initial squeezing of the segments widens the slots, thus lowering the peak magnetic field strength. Final collapse of the system could trap the projectile if it is not fast enough. This analysis was performed by Stanford Research Institute under subcontract.

### 2. Statement of Problem

The configuration to be discussed is diagrammed in Fig. 14. The assembly consists of two cylindrical shells; the outer is the armature and the inner is the flux concentrator. The armature is a continuous shell while the concentrator is slotted in three or more places parallel to the axis of symmetry of the assembly. A magnetic field is induced in the annulus between the two shells and inside the concentrator. The problem to be solved here involves finding the motions of the armature and the concentrator when the armature is given some predetermined velocity radially inward. The solution of the problem should give the time at which the armature comes into contact with the concentrator, if such contact is possible. If the armature does hit the concentrator, shock waves are induced which may have undesirable consequences. The solution includes the effects of different initial values of the intensity of the magnetic field, and of the use of different materials.

### 3. Method of Calculation

The solution of the problem was obtained by numerical methods based on an existing computer program. The program is an

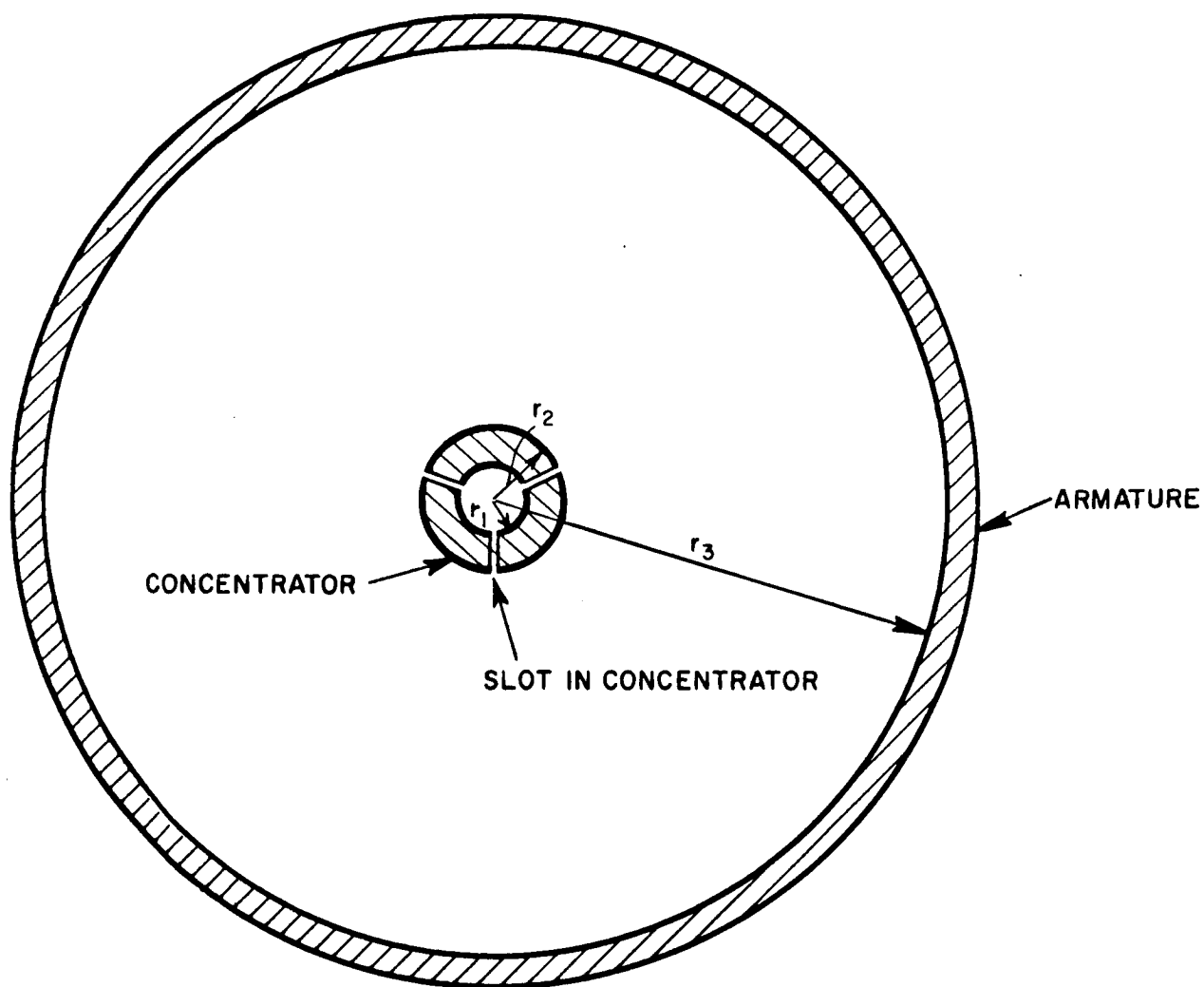


FIGURE 14. CONFIGURATION FOR FLUX CONCENTRATOR  
HYDRODYNAMIC CALCULATIONS



U	particle velocity
t	time
P	pressure
Q	artificial viscosity
E	internal energy
W	energy per unit mass added to medium from external sources (assumed to be zero)

Difference equations are derived which are second order analogs of the differential equations. The continuum in the space-time plane is divided into finite segments,  $\Delta R$  in the space direction and  $\Delta t$  in the time direction. Thus the space coordinate of a mesh point in this plane is  $X_J^n = X(J \cdot \Delta R, n \cdot \Delta t)$ . The difference equations as given by Herrmann, et al., are as follows:

$$v_{J+1/2}^{n+1} = v_{J+1/2}^0 \left[ \left( X_{J+1}^{n+1} \right)^a - \left( X_J^{n+1} \right)^a \right] / \left[ \left( R_{J+1} \right)^a - \left( R_J \right)^a \right] \quad (145)$$

$$\frac{U_J^{n+1/2} - U_J^{n-1/2}}{\Delta t^{n+1/2} + \Delta t^{n-1/2}} = \frac{P_{J-1/2}^n - P_{J+1/2}^n + Q_{J-1/2}^n - Q_{J+1/2}^n}{\left( X_{J+1}^n - X_J^n \right) / v_{J+1/2}^n + \left( X_J^n - X_{J-1}^n \right) / v_{J-1/2}^n} \quad (146)$$

$$E_{J+1/2}^{n+1} - E_{J+1/2}^n = \frac{1}{2} \left( P_{J+1/2}^{n+1} + P_{J+1/2}^n + Q_{J+1/2}^{n+1} + Q_{J+1/2}^n \right) \cdot \left( v_{J+1/2}^n - v_{J+1/2}^{n+1} \right) \quad (147)$$

$$U_J^{n+1/2} = \frac{X_J^{n+1} - X_J^n}{\Delta t^{n+1/2}} \quad (148)$$

where:

n	index for time
J	index for Lagrange coordinate
$\Delta t$	increment in time

KQ    coefficient for quadratic term of Q  
 KL    coefficient for linear term of Q  
 C    local sound speed [SND (J) in code]  
 $\rho$     density

Both linear and quadratic terms are included in the equation for Q, either of which may be used alone or in combination, depending on the values of the constants, KQ and KL. There is no general guide to the best values for the two constants, although Grandey<sup>8</sup> gives a useful discussion of the problem. Experimentation with different values of the constants is frequently required to ensure a reasonable solution, especially if the equation of state of the media is unusual. The difference equation for Q is

$$Q_{J+1/2}^n = - \left[ (KQ)^2 |\Delta U| + KL \cdot C_{J+1/2}^{n-1} \right] \Delta T / V_{J+1/2}^n \quad (149)$$

where

$$\Delta U = U_{J+1}^{n-1/2} - U_J^{n-1/2}$$

and

$$C = \sqrt{dP/d\rho}$$

The difference equations yield a stable solution if the increment in time is suitably controlled. The relation for determining the time step uses the same constants as does the relations giving the value for Q. The relation is

$$\Delta t_{J+1/2}^{n+1/2} = \frac{X_{J+1}^n - X_J^n}{(1 + 2 \cdot KL) C_{J+1/2}^n + 4(KQ)^2 |\Delta U|} \quad (150)$$

<sup>8</sup>R. A. Grandey, "PUFF-VTS Computer Program," Tech. Doc. Rept. No. AFSWC-TDR-62-76, February 1963.



This quantity is evaluated for each value of  $J$ , and the minimum value is used to calculate the next increment in time. This does not use the computer as efficiently as does the scheme used by Grandey, in which he uses the time-step calculated at each mesh point to advance the solution for that mesh point. The variable time-step method requires considerably more coding than does the fixed time-step type of operation.

The computer program which was adapted for solving this problem is described in some detail in Final Report, Project GSU-4475, Stanford Research Institute.

One of the major changes that had to be made in the program consisted in adapting it to handle two regions, viz, the armature and the concentrator. Provision also had to be made for the use of a different equation of state in these two regions. The program had to provide for the possibility that the armature might strike the concentrator, and for the effects of the pressure due to the magnetic field.

The magnetic pressure is  $B^2/(8\pi)$ , where the field strength is given in megagauss and the pressure is in megabars. As the armature moves inward, the area occupied by the field is reduced, and the field strength is increased. Assuming no flux leakage through the armature, the strength of the field at any time is

$$B = B_0 A_0 / A, \quad (151)$$

where  $B_0$  is the field strength at a time when the cross sectional area is  $A_0$ . The area  $A$  is a function of time and is calculated by the program by using the radii  $r_1$ ,  $r_2$ , and  $r_3$ ,

$$A = \pi (r_e^2 + r_1^2 - r_2^2). \quad (152)$$

The channels are ignored in the calculations of the area occupied by the magnetic flux.

The Mie-Gruneisen equation of state

$$P - P_H = (\gamma/V) (E - E_H) \quad (153)$$

was used to relate the pressure  $P$ , volume  $V$  and the energy  $E$ . The quantities  $P_H$  and  $E_H$  are related to the volume  $V$  by the relations

$$\mu = V_0/V - 1$$

$$P_H = A\mu + B\mu^2 + C\mu^3$$

$$E_H = 0.5 P_H (V_0 - V).$$

The latter two relations define a curve called the Hugoniot. The coefficients  $A$ ,  $B$ , and  $C$  were adjusted so that the function fit the experimentally determined Hugoniot data. The Gruneisen ratio  $\gamma$  is given by

$$\gamma = \gamma_0 + e\mu + f\mu^2 + g\mu^3. \quad (154)$$

Values of the coefficients are given in Table I.

TABLE I  
EQUATION OF STATE CONSTANTS

<u>Constant</u>	<u>Aluminum</u> <sup>a</sup>	<u>Copper</u> <sup>b</sup>	<u>Gold</u> <sup>c</sup>
A	0.765	1.597	1.9117
B	1.659	1.0525	2.4905
C	0.428	6.3875	8.420
$\gamma_0$	2.13	2.0	3.29
e	-7.245	-1.740	-3.29
f	24.707	1.90	3.29
g	-32.577	-5.207	-3.29

<sup>a</sup> Coefficients from M. H. Rice, R. G. McQueen and J. M. Walsh, "Compression of Solids by Strong Shock Waves," Solid State Physics, Vol. 6, Academic Press, Inc., New York, 1958.

<sup>b</sup> Coefficients fitted to Hugoniot data given by R. G. McQueen and S. P. Marsh, "Equations of State for Nineteen Metallic Elements from Shock Wave Measurements to Two Megabars," J. Appl. Phys. 31, 1253 (1960).

<sup>c</sup> Coefficients for  $\gamma$  from approximate fit to data of R. G. McQueen and R. G. Marsh (footnote above) and data of L. V. Al'tschuler, S. B. Kormer, A. A. Bakanova and R. F. Trunin, "Equation of State for Aluminum, Copper and Lead in the High Pressure Region," Soviet Phys.-JETP 11, 573 (1960).

In all cases for which calculations have been done, the armature was assumed to be made of aluminum; the material of the concentrator was either copper or gold. Different values of  $r_1$  and  $B_0$  were used. Parameters for twelve cases are summarized in Table II. In all cases, the inside diameter of the armature is 2.0 in., and the thickness of the armature is 1/16 in. (0.159 cm). The initial velocity of the armature was assumed to be 0.5 cm/ $\mu$ sec radially inward.

TABLE II  
PARAMETERS AND MATERIALS

Case	Concentrator Material	$B_o$ (kgauss)	Concentrator Radius ( $r_1$ )*		Armature Contacts Concentrator
			(cm)	(in.)	( $\mu$ sec)
1	Copper	25	0.225	0.0885	3.82
2	Copper	25	.113	.0445	3.95
3	Copper	25	.019	.0075	None
4	Copper	50	.225	.0885	3.92
5	Copper	50	.113	.0445	None
6	Copper	50	.019	.0075	None
7	Gold	25	.225	.0885	3.82
8	Gold	25	.113	.0445	3.96
9	Gold	25	.019	.0075	None
10	Gold	50	.225	.0885	3.92
11	Gold	50	.113	.0445	None
12	Gold	50	.019	.0075	None

\* Outside radius ( $r_2$ ) = 0.402 cm.

Because the von Neumann-Richtmyer artificial viscosity method is a finite difference method, the media may be visualized as being divided into a number of cells. The computational scheme proceeds by calculating the velocity of each cell wall and the pressure in the cell at a given time. The time is then advanced and the computations are repeated for each cell. Shock fronts are smeared out over a few cells, so that sharp discontinuities are reproduced poorly unless many cells are used. In the present problem details of the flow in the interior of the metal parts of the device are not needed. The gross behavior of the armature and concentrator are given by using a relatively small number of

cells--10 to represent the armature. Hence each cell is 0.016-cm thick, and the same thickness was used for each cell in the concentrator, 24 cells being used for the case in which  $r_1 = 0.019$  cm.

#### 4. Results

The results of the computations are presented in Figs. 15 through 26. The most noteworthy feature is that the inside diameter of the flux concentrator initially increases as the metal is compressed by the very high magnetic pressure. This not only leaves the projectile (also highly compressed) free, but also limits the peak magnetic field by increasing the cross-sectional area. Other points to be noted are:

- a. The armature does not contact the flux concentrator for the smallest value of  $r_1$ .
- b. The magnetic field gradient is perhaps a little larger for lower initial field.
- c. The peak field is slightly higher for a gold flux concentrator as compared with copper.
- d. The peak field is the same for the two values of initial field which were used.
- e. The field gradient changes sign at long times.

It is difficult to assess how closely these computations represent reality, because of the simplifying assumptions that were made. In particular, the explosive was ignored, except for the initial velocity it imparted to the armature. The magnitude of the initial velocity was itself an assumption, or rather, an educated guess, based on a lower limit from the case of a non-convergent detonation, and an average value derived from the total armature collapse time measured in an earlier experimental configuration with no magnetic field.

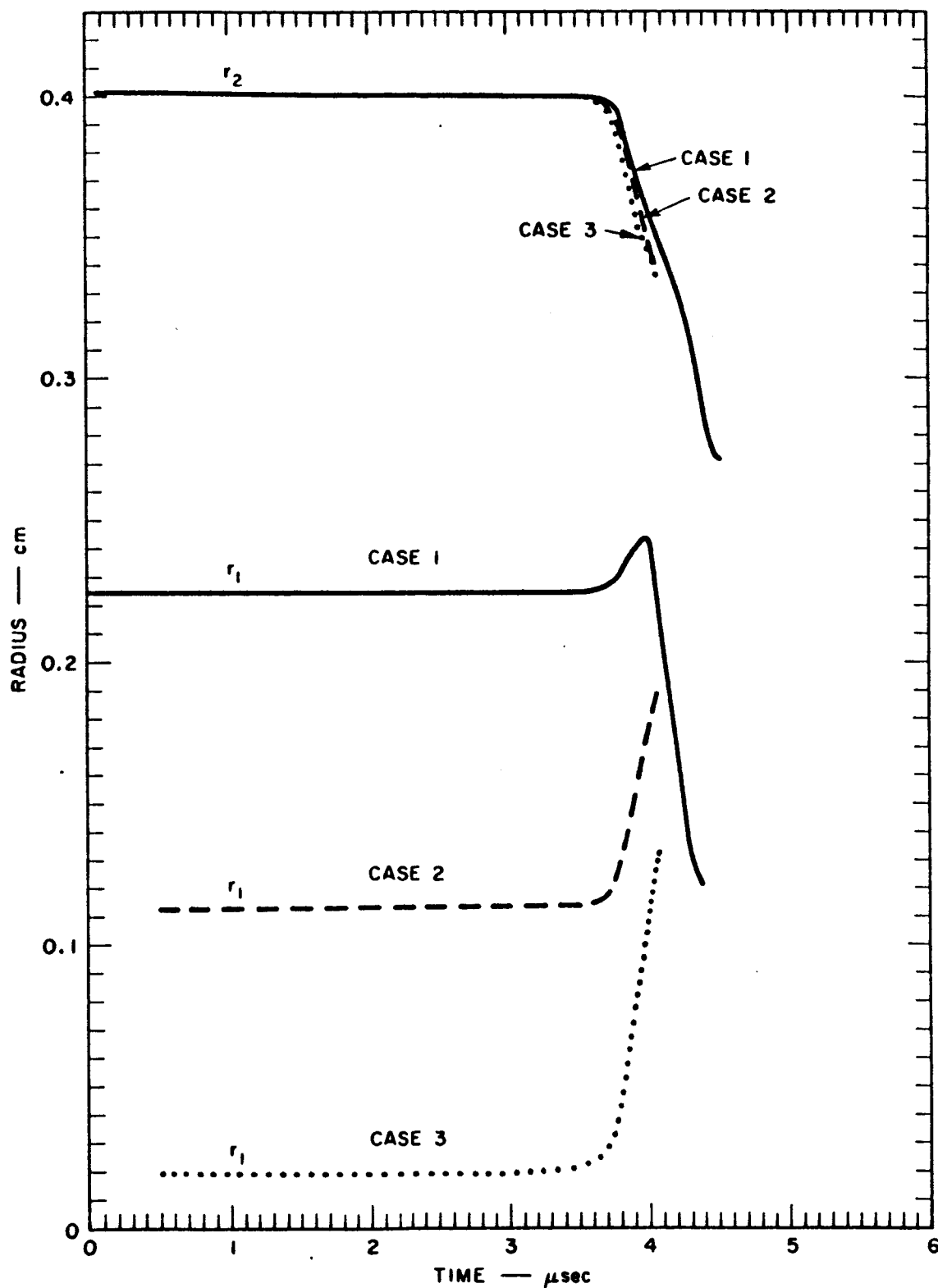


FIGURE 15. FLUX CONCENTRATOR INNER AND OUTER RADII VERSUS TIME, CASES 1, 2, 3

33-1-66-085

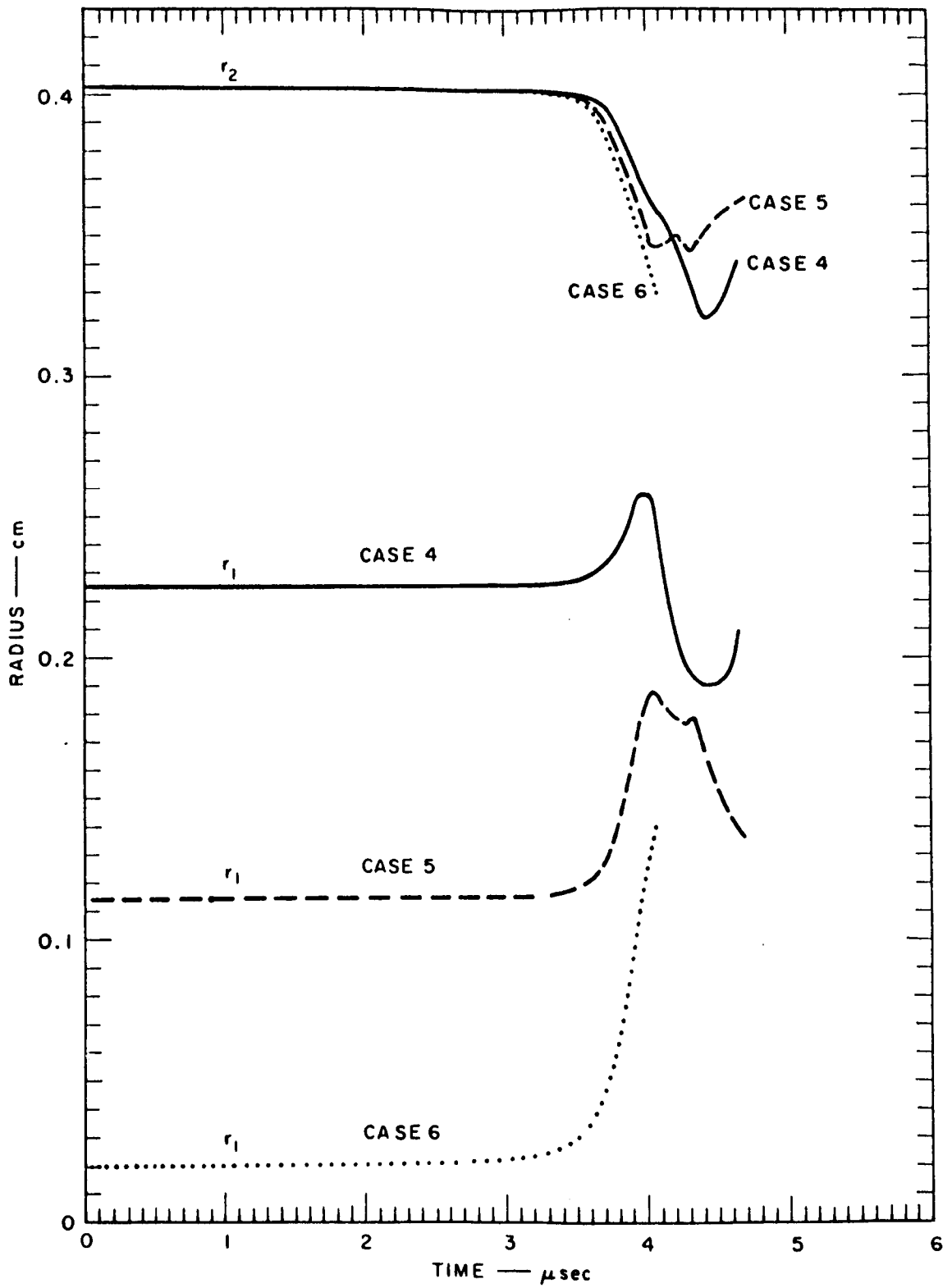


FIGURE 16. FLUX CONCENTRATOR INNER AND OUTER RADII VERSUS TIME, CASES 4, 5, 6

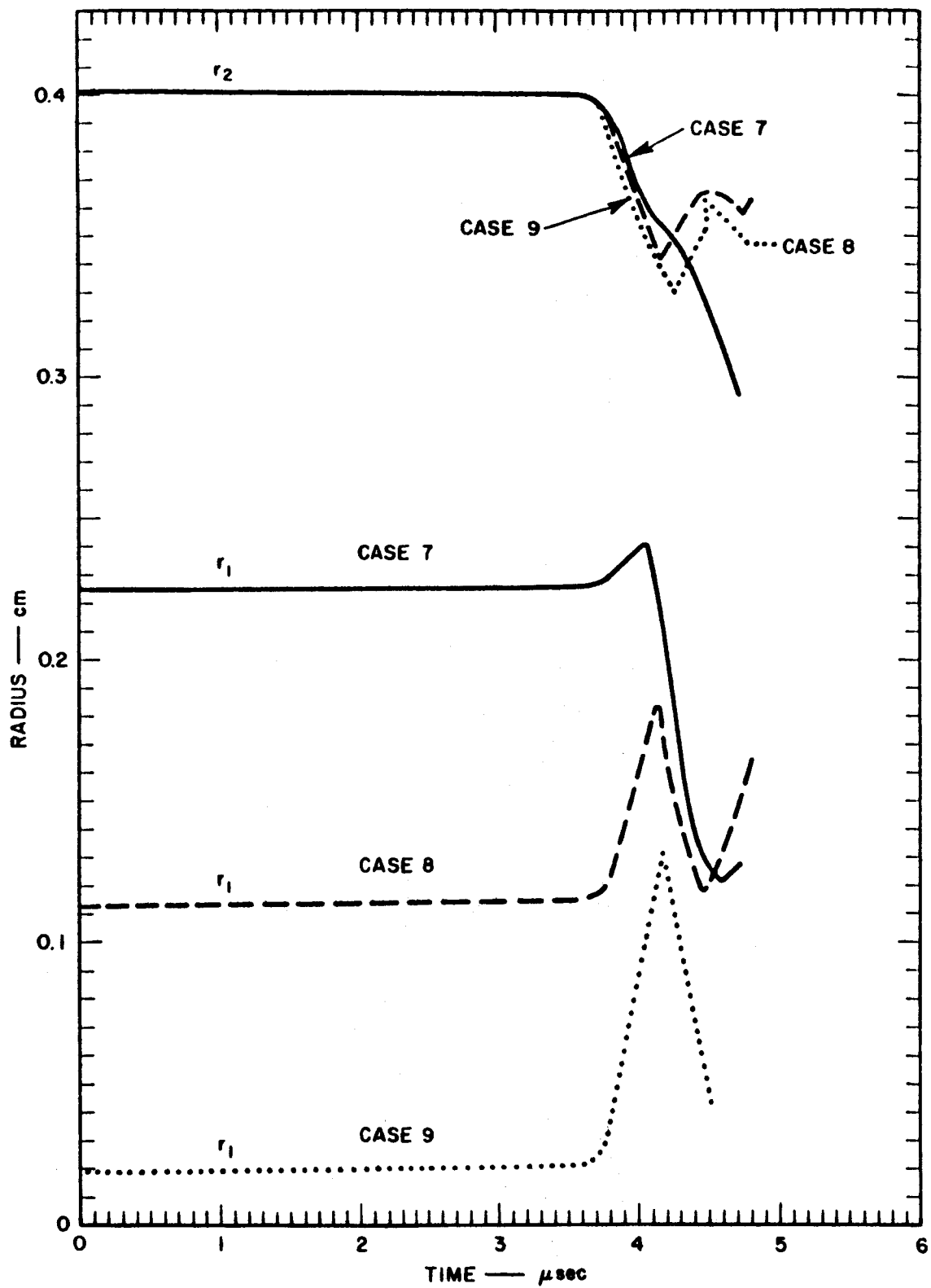


FIGURE 17. FLUX CONCENTRATOR INNER AND OUTER RADII VERSUS TIME, CASES 7, 8, 9

35.1-66-007



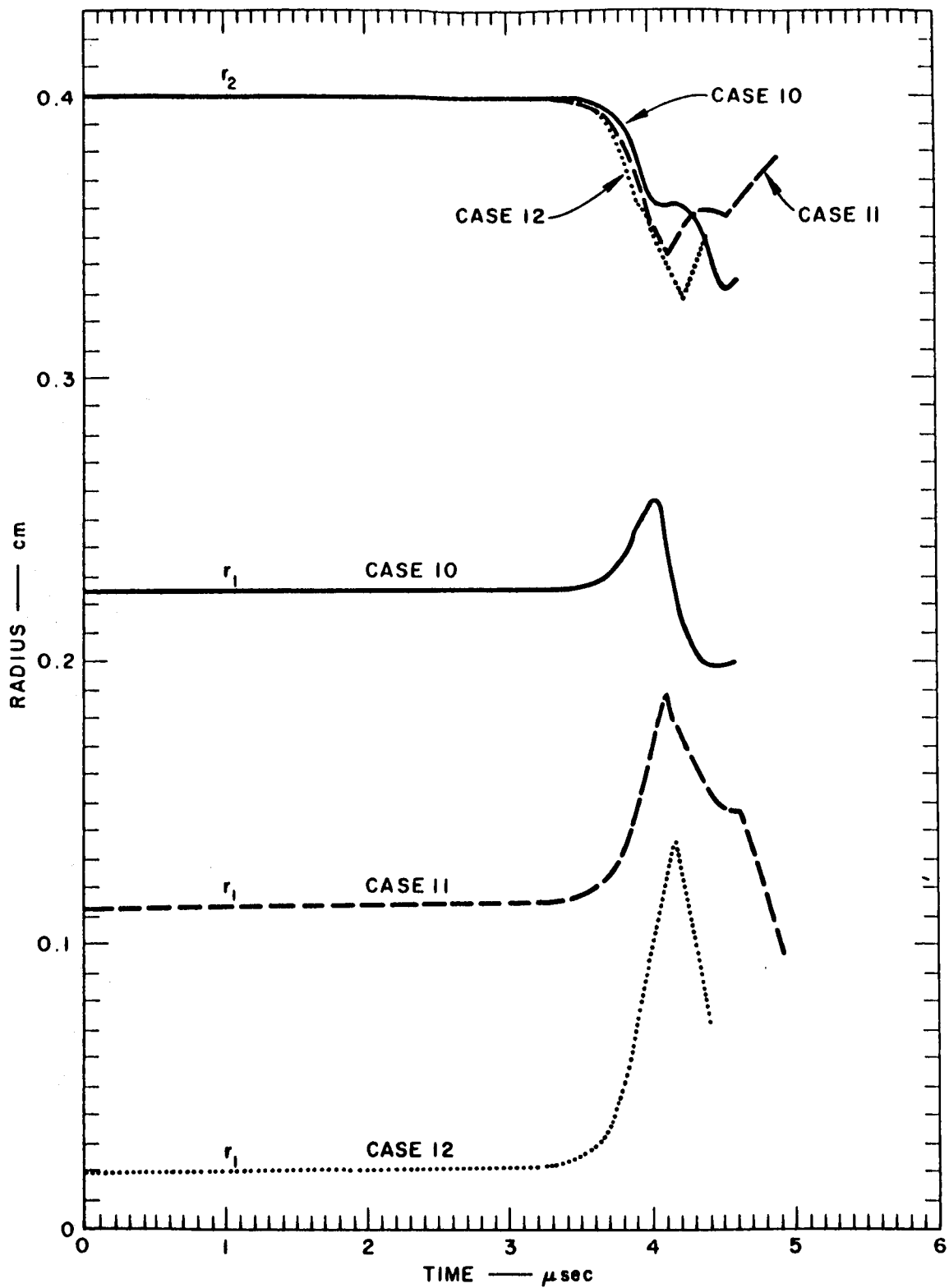


FIGURE 18. FLUX CONCENTRATOR INNER AND OUTER RADII VERSUS TIME, CASES 10, 11, 12

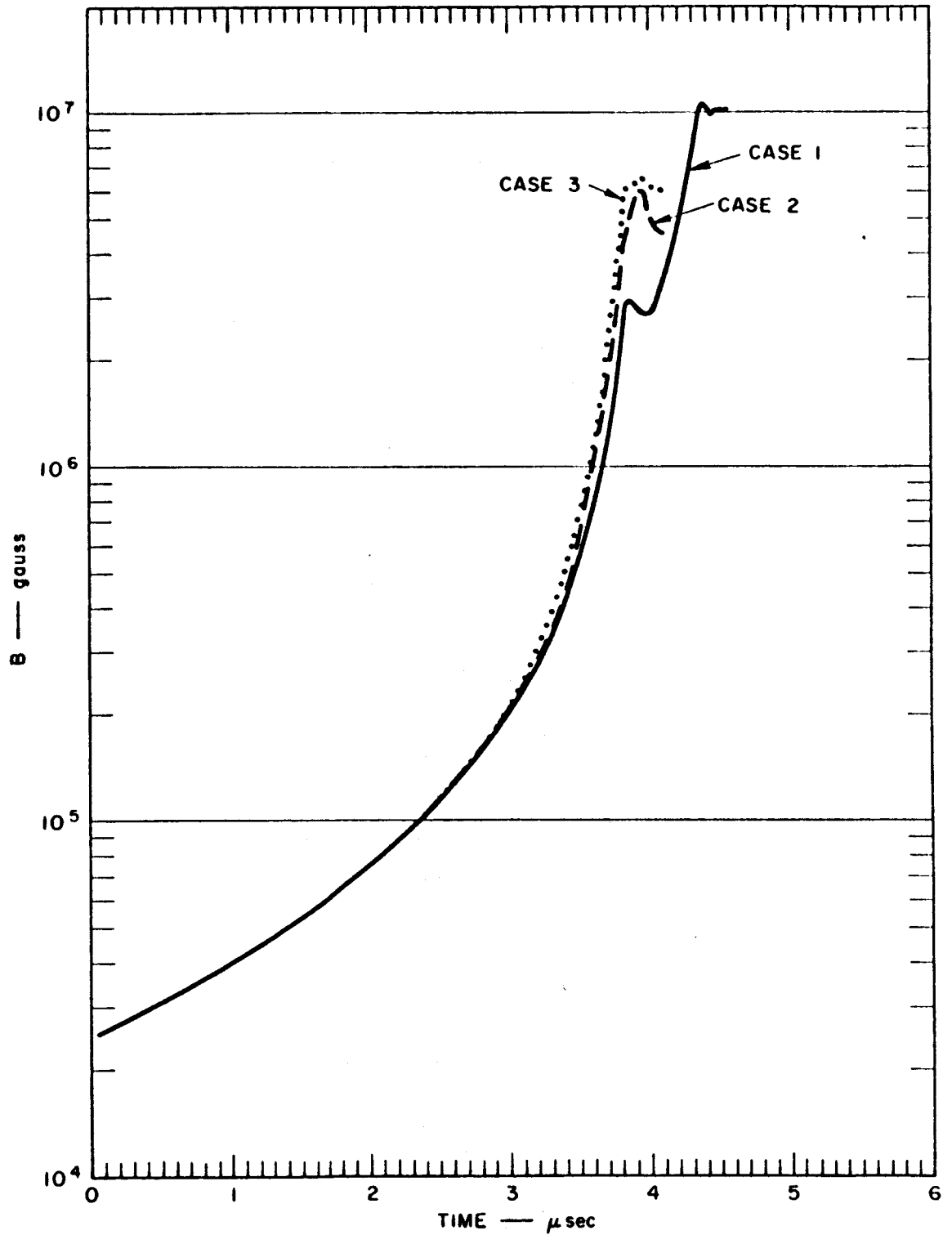


FIGURE 19. MAGNETIC FIELD STRENGTH VERSUS TIME, CASES 1, 2, 3

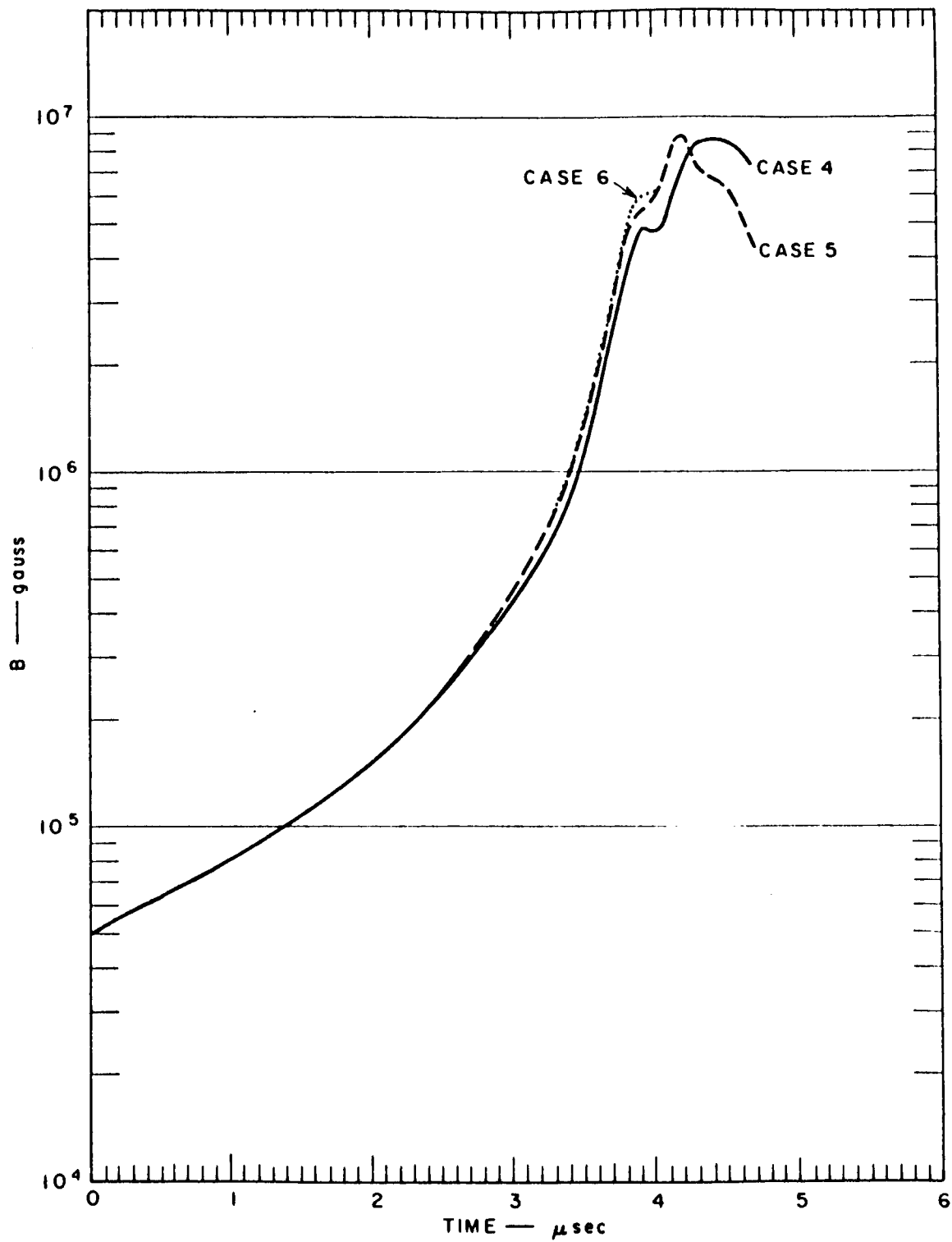


FIGURE 20. MAGNETIC FIELD STRENGTH VERSUS TIME, CASES 4, 5, 6

35.1-65-090

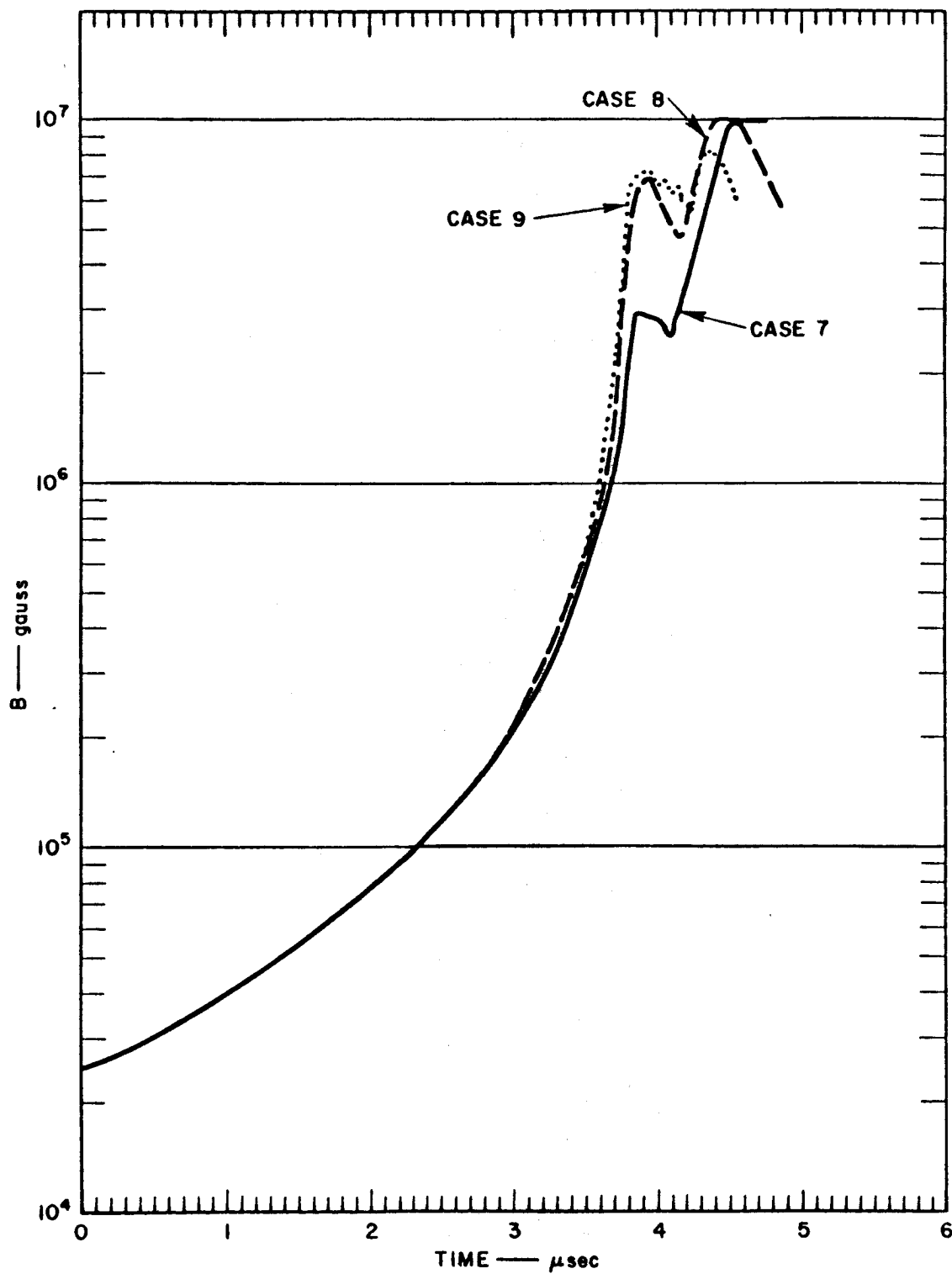


FIGURE 21. MAGNETIC FIELD STRENGTH VERSUS TIME, CASES 7, 8, 9

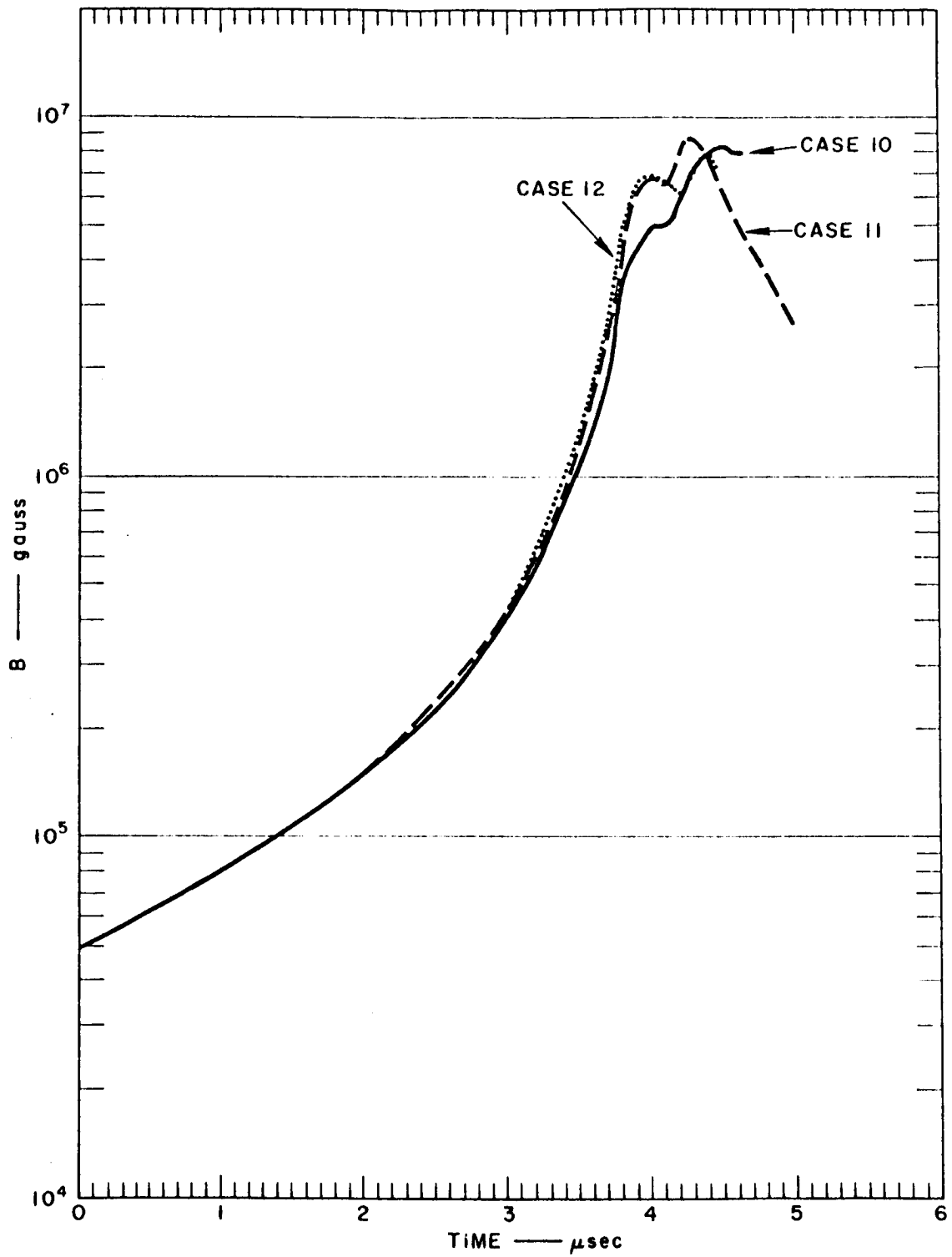


FIGURE 22. MAGNETIC FIELD STRENGTH VERSUS TIME, CASES 10, 11, 12

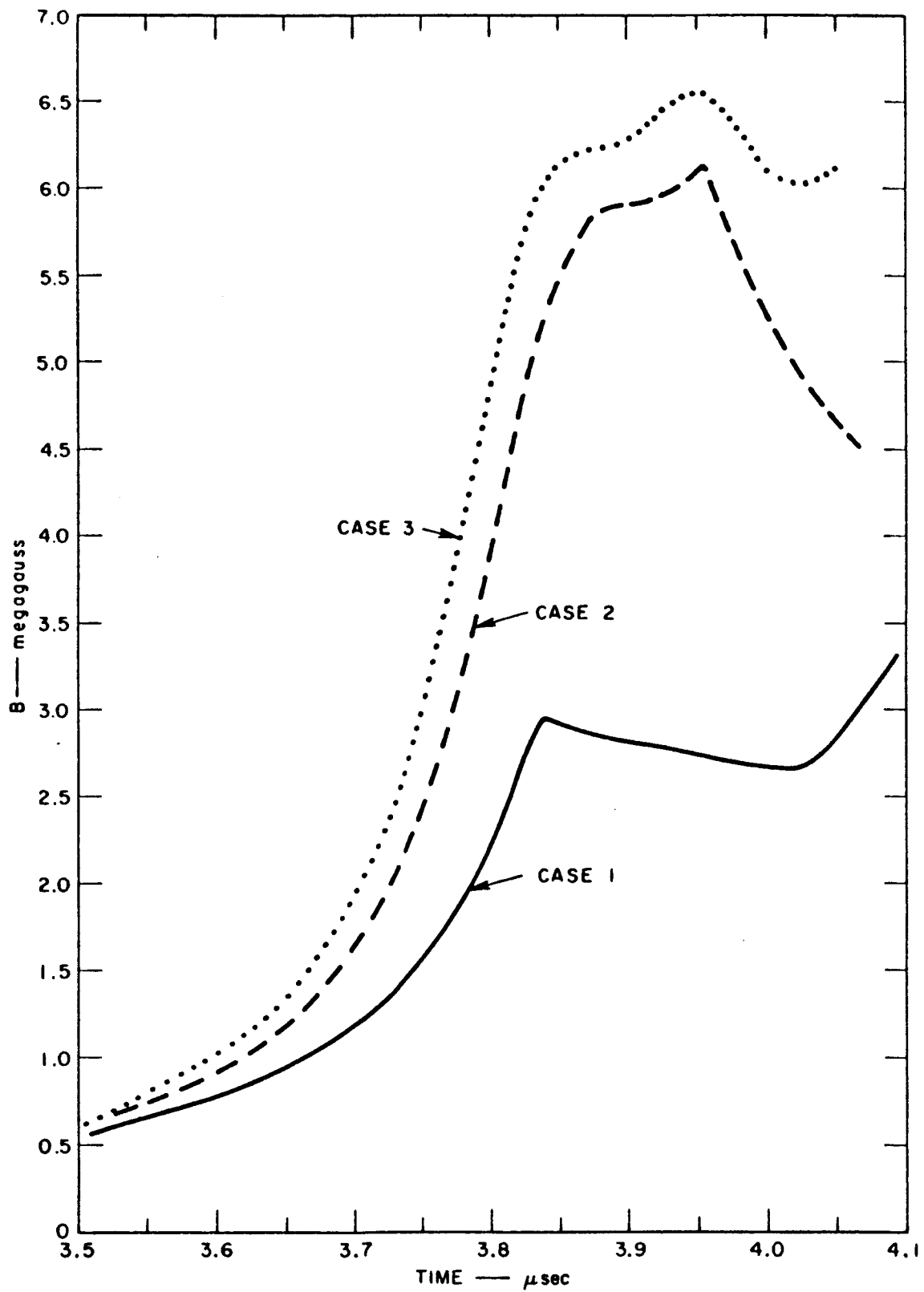


FIGURE 23. MAGNETIC FIELD STRENGTH VERSUS TIME AT END OF COMPRESSION, CASES 1, 2, 3

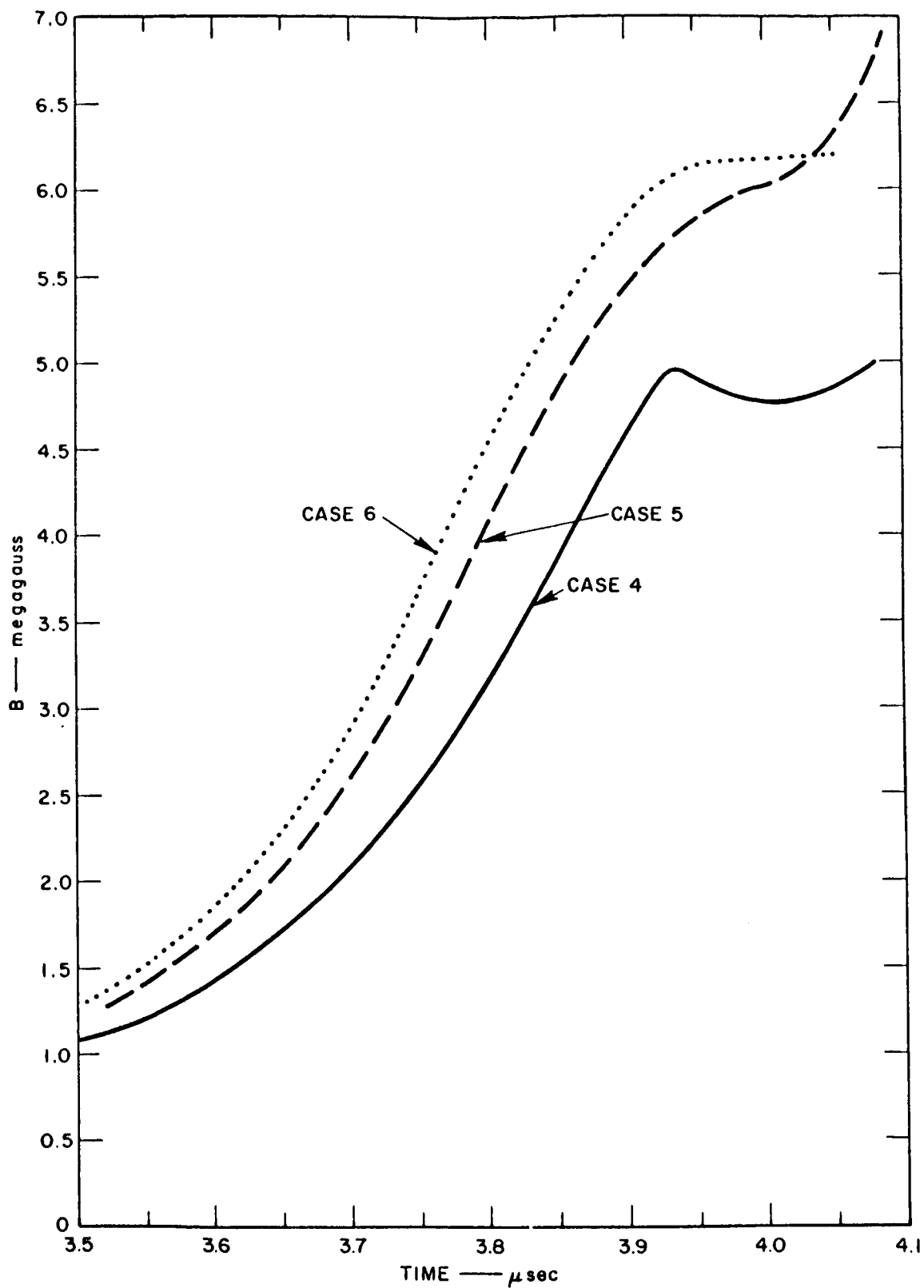


FIGURE 24. MAGNETIC FIELD STRENGTH VERSUS TIME AT END OF COMPRESSION, CASES 4, 5, 6

351-66-094

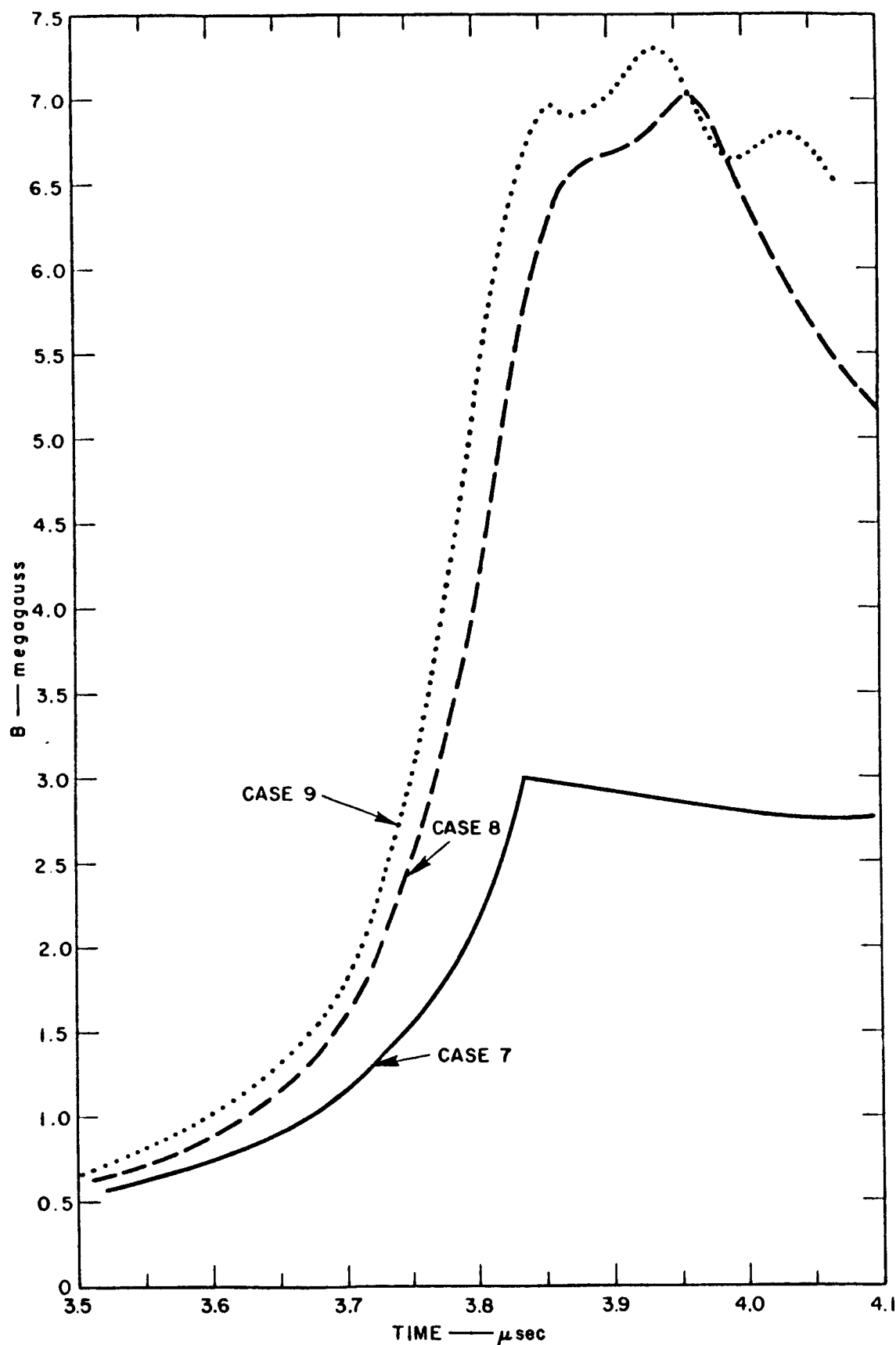


FIGURE 25. MAGNETIC FIELD STRENGTH VERSUS TIME AT END OF COMPRESSION, CASES 7, 8, 9



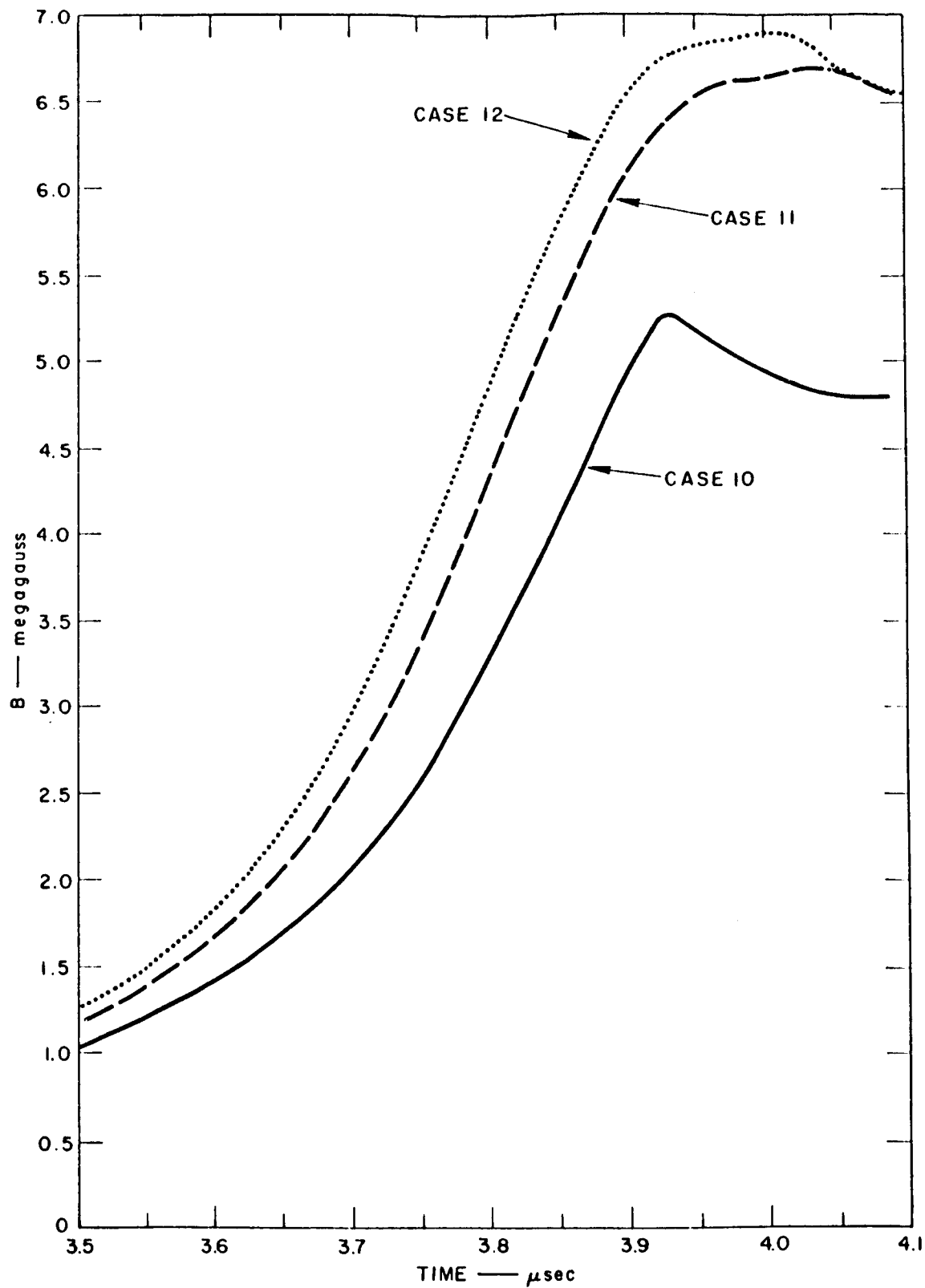


FIGURE 26. MAGNETIC FIELD STRENGTH VERSUS TIME AT END OF COMPRESSION, CASES 10, 11, 12

It was assumed that the armature collapse began simultaneously everywhere, i.e., any curvature of the detonation front was neglected. We know that the center of the front must lead the edges for the geometry employed, and hence the field gradient has been presumably underestimated.

The curves take on complex shapes near times of contact or closest approach. The significance of this structure is not clear because of the complex shock interactions taking place.

Another simplification in the calculations is the neglect of the slots in the flux concentrator. This should result in an overestimate of the field strength as the armature nears the flux concentrator because the effective cross-sectional area is underestimated. This will be most severe for small  $r_1$ , and could rather drastically change the peak field values for the case of  $r_1 = 0.019$  cm.

#### IV. REDESIGN AND IMPROVEMENT OF SYSTEM PERFORMANCE

##### A. EXPLOSIVE SYSTEM

The achievement of high peak magnetic field strengths in the magnetic gradient accelerator depends largely on the circular symmetry of the armature when it arrives at the flux concentrator. Thus the precision with which the outside surface of the explosive is simultaneously detonated is quite important. Earlier in this work, under Contract NAS8-5266, a flying cone cylindrical wave initiator was developed which created a cylindrical detonation from one detonator. Although the flying cone system worked fairly well it proved to have limitations. Test results indicated that better azimuthal symmetry would be required to consistently obtain high peak magnetic field strengths. The improvement of azimuthal symmetry in this system would require a much better control of density uniformity during the casting of the blanks from which the various explosive components were machined. It was felt that the facility available to the experimenters could not be improved, and thus the decision was made to try a multiple detonator system. Also, switching to the multiple detonator configuration meant that the upper magnet coil would no longer be enclosed. The enclosure of the coil by the flying cone system caused some operational problems during the conduct of experiments.

##### 1. Multiple Detonator Initiation System

In the multiple point initiation scheme, the cylindrical explosive charge is surrounded by a ring of detonators. To achieve a faster implosion, more explosive was used in this system than with the

flying cone initiator. All multiple-detonator system shots have had a main charge diameter of 228.6 mm. In all cases 24 detonators were used spaced  $15^{\circ}$  apart. Thus the detonators were about 30 mm center to center. The thickness of the explosive charge was the same as before, 50.8 mm. The detonators were spaced along a circle at the center plane, causing some axial curvature in the detonation front, symmetric about the center plane. There is a possibility that this curvature aids the development of the gradient across the projectile.

Two types of exploding bridge wire detonators were considered. The first was a general purpose precision detonator fabricated by SRI. This detonator, the PL-2, is cheap and readily available. A high-quality, weapons type detonator, designated SE-1, was made available to U. S. Government contractors on a commercial basis about the time this problem arose. The SE-1 detonators are expensive but are also readily available. Their total time to detonation is listed as  $3.666 \mu\text{sec}$  with a time variation of  $0.013 \mu\text{sec}$ .

Simultaneity tests were conducted using a standard 200-joule detonator firing unit located in the bunker. Multiple cables were run to the detonators at the firing position. The results of these tests are listed in Table III.

TABLE III  
DETONATOR TIME VARIATION WITH STANDARD 200-JOULE FIRING UNIT

Description	Jitter ( $\mu\text{sec}$ )	
	Average	Maximum
12-PL 2, parallel connected to two copper rings	0.43	1.24
12-SE 1, parallel groups of three, 4 det. cables	0.17	0.71
12-PL 2, parallel groups of two, 6 det. cables	0.29	0.51
12-PL 2, parallel connected to 12 det. cables	0.22	0.36
12-SE 1, parallel groups of two, 6 det. cables	0.10	0.20

Because of the excessive cable inductance and the inherent design of the firing unit, the firing time variation between detonators was larger than that believed to be attainable. The SE-1, however, showed much better performance than the PL-2's.

Improvement of detonator firing simultaneity required the construction of a firing unit with a much faster rise time. To achieve this with a high energy system, expendable slave firing units were constructed and located approximately 1/2 m from the explosive. This design consisted of four 0.5- $\mu$ f capacitors in parallel which were pulse-charged in 6.5  $\mu$ sec by a standard high capacity firing unit in the bunker. The slave units contained an automatic spark gap that discharged the capacitors at 8.5 kv. The energy was delivered to the detonators through 24 coaxial cables (1 per detonator), about 0.75 m in length. With this system the average firing time variation of the SE-1 detonators was reduced to 0.04  $\mu$ sec.

In July 1965, test operations were terminated at SRI and were moved to the AGN Pulse Power Facility. The AGN facility uses a containment tank that completely confines the explosion, and thus expendable slave units were no longer necessary. A permanent low inductance system was designed and fabricated. This slave unit, illustrated in Fig. 27, is installed just outside the containment tank wall. Its capacitors are of extended foil construction to handle the large current peaks and reduce system inductance. The coaxial spark gap is mounted under the upper plate. A separate coaxial cable, 2 m long, is provided for each detonator. The total slave unit energy is 64 joules at 8 kv. The circuit diagram of the system is illustrated in Fig. 28. This system has provided an SE-1 firing time average variation of  $\pm 0.01 \mu$ sec over 24 detonators.

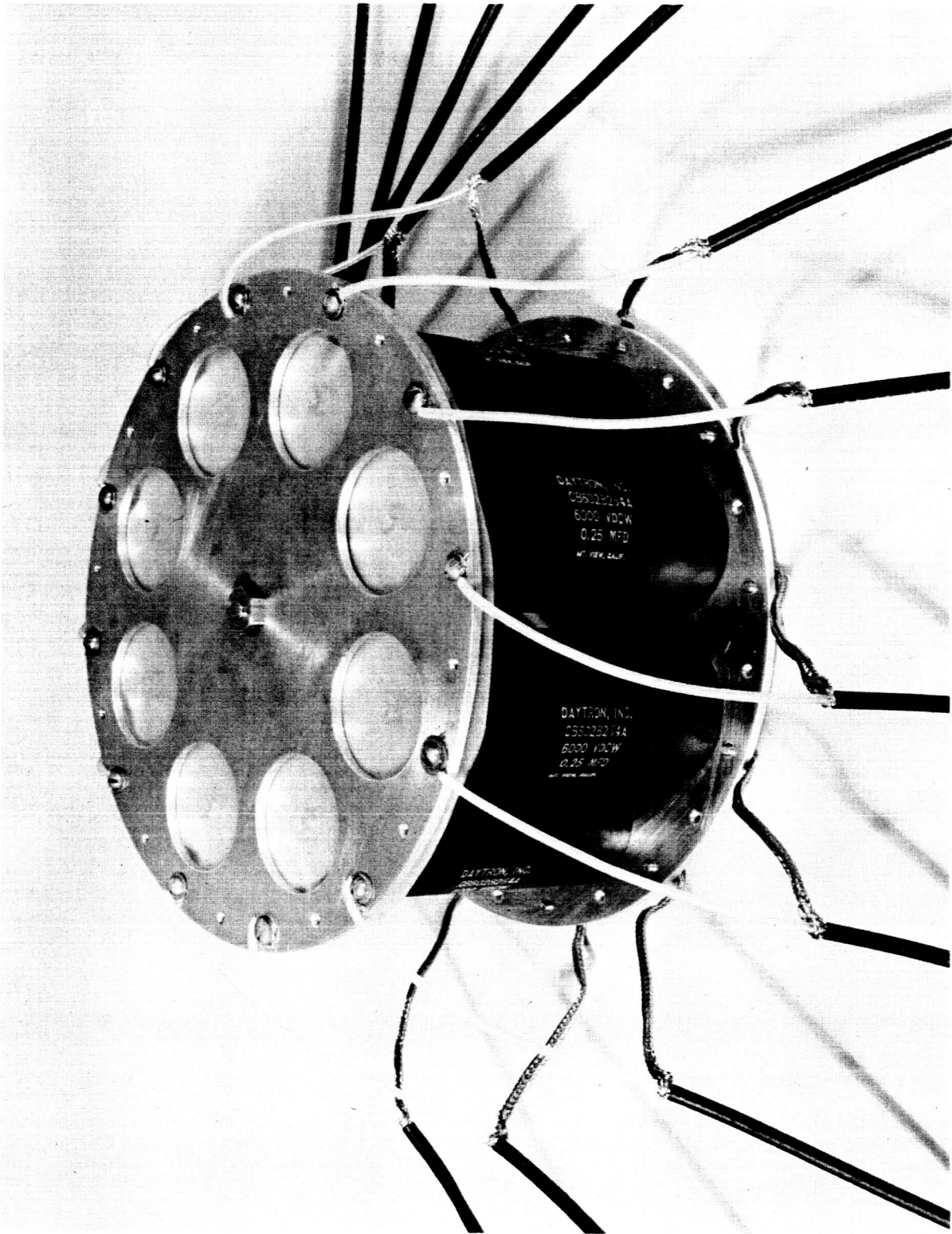


FIGURE 27. MULTIPLE DETONATOR FIRING SYSTEM - SLAVE UNIT

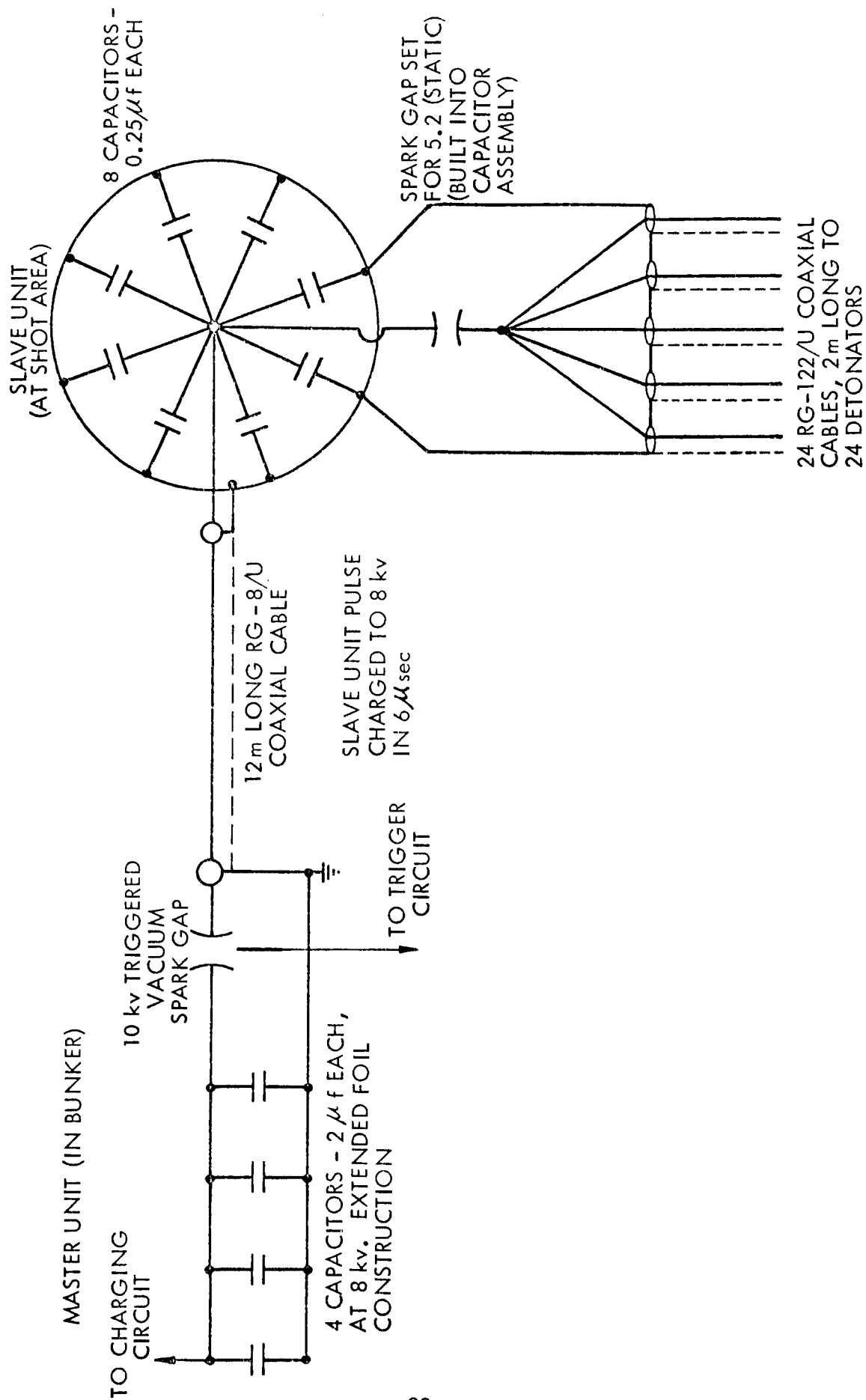


FIGURE 28. SCHEMATIC DIAGRAM OF MULTIPLE DETONATOR FIRING SYSTEM

## 2. Armature Considerations

The presence of the flux concentrator makes it imperative that the armature collapse be as cylindrical and concentric as possible; otherwise, magnetic flux could be trapped outside the flux concentrator by eccentricities or perturbations in the armature wall. Until recently, great care was taken to insure a round, constant wall thickness aluminum armature in the annealed state. An elaborate and expensive process of machining and annealing in several steps was used. Tolerances in all dimensions were held to 0.012 mm. However, tests have been conducted using armatures machined from 6061-T6 aluminum with the same degree of machining precision. There appears to be no measurable difference in the performance. The surfaces of all armatures are polished to eliminate any nicks or scratches which could give rise to jetting or the formation of instabilities during the collapse. All armatures had an i.d. of 5.08 cm and a wall thickness of 1.57 mm. Unless evacuated, they were purged with Freon 12 to inhibit electrical breakdown.

## 3. End Confinement of the Main Explosive Charge

Since the thickness of the main explosive charge is substantially less than its diameter, there is a tendency of the detonation front to lag at the end relative to its position along the center plane perpendicular to its direction of motion. This end effect can be reduced by placing a tamping material in contact with the explosive, this confinement being perpendicular to the direction of motion of the detonation front. Stainless (non-magnetic) steel was used with a battery-driven initial magnetic field system. When the change to the capacitor bank system was made, the shorter pulse rise time required re-examination of the end plate material.



Tests were conducted to determine the effect of several materials on the axial shape of the armature. These simulated the cylindrical geometry with a linear geometry. A plane wave generator was used to detonate a rectangular block of explosive. The explosive was confined between two end plates and launched an aluminum flyer plate. The shape of the flyer plate was observed with flash x-ray. The same arrangement without the flyer plate was used to determine the shape of the detonation front. A streak camera slit was oriented perpendicular to the confining plates along the center of the explosive. The results of these tests showed that the flyer plate shape was essentially the same as the detonation front shape.

The results of two tests with 6.35-mm thick phenolic and stainless steel plates and air are shown in Fig. 29. Stainless steel produced a smaller edge effect than phenolic, as expected. The profile observed at the explosive-air interface was not consistent with known characteristics of detonation for an air boundary. Density variation in the Composition B pad is a possible explanation.

The superiority of stainless steel or materials of similar density is obvious. To achieve high density end confinement and maintain compatibility with the magnet system, the tamping plate material was changed to an epoxy loaded with lead powder (Epocast). After two days of curing in the mold, end plates of this material were quite rigid and had good dimensional stability. Their cast density is typically  $7.5 \text{ g/cm}^3$ . Since the lead was powdered there was no gross conductivity across the plates and the magnetic flux penetrated quite readily. Also, explosive performance appeared to be quite satisfactory.

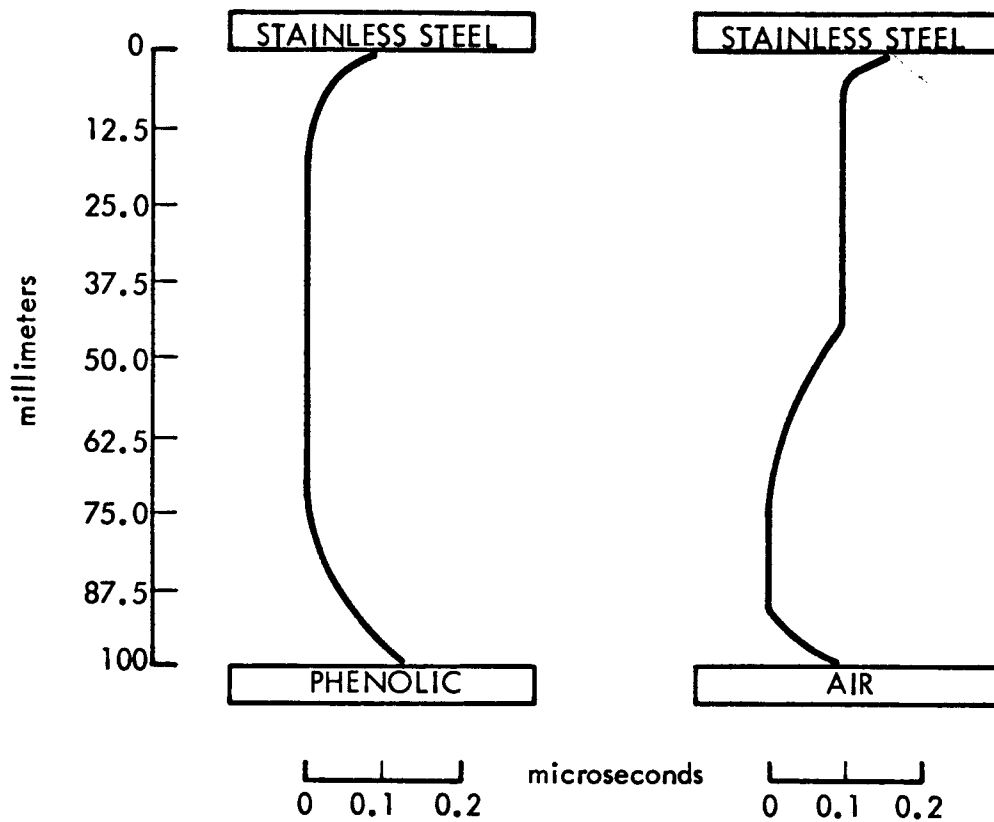


FIGURE 29. EXPLOSIVE END CONFINEMENT TEST RESULTS

351-66-099

## B. MAGNETIC FIELD SYSTEM

Initial magnetic field strengths of several tens of kilogauss within the armature were desired. To achieve this with a practical power supply and expendable coils, a pulse discharge system was used. The armature had to be a completely closed cylinder (i.e., no slots to allow flow of field to the interior). It was therefore necessary to make the rise of the magnetic field slow enough to allow diffusion of the flux lines through the armature wall to its interior prior to the explosive collapse. At the beginning of this program, under NAS8-5266, the power supply was a bank of lead acid storage batteries. During the current contract, being reported here, a slow rise time capacitor discharge system was developed.

### 1. Capacitor Bank Magnet System

With the storage battery power supply, the highest magnetic field strength which could be achieved in the armature was about 20 kgauss. A stronger field was required. There were two alternatives: The battery supply could be enlarged, or another type of system could be used. Since the battery power supply proved to be cumbersome and difficult to keep in the fully charged state, it was decided to try a slow rise time capacitor bank magnet system. Moreover, use of capacitors eliminated the requirement for liquid nitrogen cooling of the coils, which had created a number of severe operational problems.

In the battery-supplied magnet system, the peak current is dependent almost entirely on the dc resistance of the coils. In a capacitor bank system, the peak current is controlled by the ac impedance due to the inductance and capacitance of the circuit. In most systems of this type, the resistance affects the circuit characteristics by only a few percent. With the 46-kj, 230- $\mu$ f capacitor bank available to the experimenters, it was estimated that two to three times more field

strength could be obtained. Elimination of liquid nitrogen cooling removed the requirement for coil cans, insulation, and a number of other fittings.

To approach this design problem, some calculations were made to estimate the diffusion time and capacitor system rise time required to get at least  $3/4$  of the available flux into the armature. Also, the presence of end plates had to be considered. These calculations indicated that a capacitor bank system rise time of 1.5 to 2 msec would be required. This was for the aluminum armature, using stainless steel explosive tamping end plates 6.35 mm thick.

To test this concept, 41 small- and full-scale tests were conducted. The small-scale tests utilized two low-voltage capacitor banks of 60 and 237  $\mu\text{f}$ . The full-scale tests used the 230- $\mu\text{f}$ , 46-kj bank. The characteristics of the magnets tested are given in Fig. 30. These tests determined the effect of the armature and end plates on the peak magnetic field obtainable within the armature. In many of these, detailed field distribution measurements were taken within the armature using a 2-mm diameter search coil. With a capacitance of 230  $\mu\text{f}$ , a magnet coil inductance of 4 to 5 mh would permit a rise time slow enough to allow more than 80% of the flux to diffuse to the interior of the armature. It was interesting to observe the delay of field rise within the armature relative to that outside. For example, a system rise time of 1.5 msec would produce a field rise time within the armature of about 1.85 msec. The detailed field plots indicated that the magnetic field strength did not vary more than about 10% throughout the inner 90% of armature volume.

Having determined the electric circuit parameters, it was then necessary to consider the mechanical design problems. Since the coils would be destroyed with each shot, it was mandatory that they be inexpensive to fabricate. In a high power system of this type, the

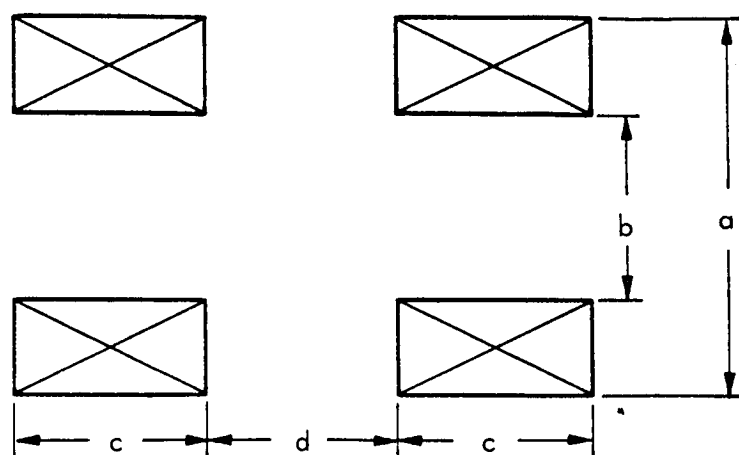


TABLE OF CHARACTERISTICS (DIMENSIONS IN cm)

COIL MODEL	a	b	c	d	WIRE SIZE	URNS COIL	NO. OF LAYERS	TOTAL L (mh)	POTTING	TEST ENERGY
1	5.24	3.40	2.79	5.71	#19	280	10	5.22	--	LOW
2	5.38	4.32	2.79	5.71	#19	140	5	1.66	--	LOW
3	6.82	5.08	2.79	5.71	#19	252	8	5.21	--	LOW
4	10.16	5.08	5.08	6.35	#10	200	10	4	POLYESTER	FULL
5	9.75	5.08	2.69	6.35	#14	224	14	6	POLYESTER	FULL
41	10.16	5.08	5.08	6.35	#10	200	10	4	POLYESTER	FULL

MODELS 1, 2, 3 USED IN SCALE TESTS

FIGURE 30. CHARACTERISTICS OF CAPACITOR DRIVEN MAGNETS FOR INITIAL MAGNETIC FIELD PRODUCTION

35.1-66-100

magnetic forces tend to draw the coil turns together in the axial direction. Normal construction practice for high field strength coils dictates the use of square wire so that the axial compressive forces can be easily absorbed by the insulation between the turns. In the relatively small coils being considered for the magnetic gradient accelerator, however, it was desired to use a wire which had a width of about 2.5 mm. Square wire in this size is difficult to handle in order to achieve a uniform winding. Also, the epoxy which is used for vacuum potting cannot easily penetrate between the windings unless a cloth wrapping is applied about each individual turn to space it out from the adjacent turns. Therefore, it was decided to attempt to construct the coils from standard round #10 Formvar insulated wire. The round cross section wire presented an unstable situation in that the axial forces drawing the turns together would cause them to try to slip and ride up on each other. This would cause chafing of the insulation with resultant electrical breakdown and failure of the coil.

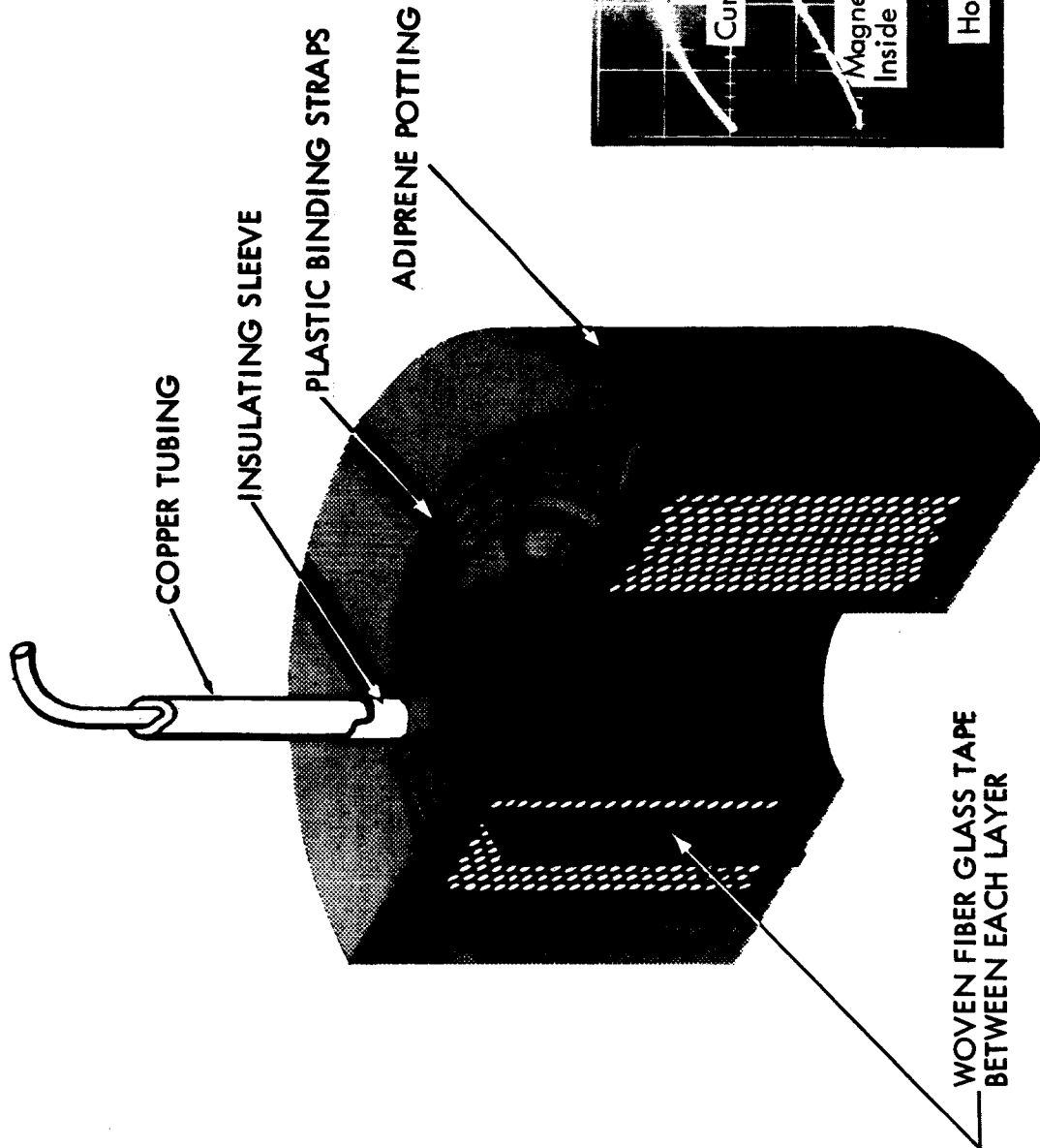
In order to limit lateral movement, the coils were wound with the turns of succeeding layers lying in the grooves between the wires of the previous layers. Thus in a coil whose turns were tightly packed and bound, any gross movement would be prevented. As an additional cushioning measure, woven fiberglass tape was laid in between the layers. Thus, when the turns of outer layers were wound into the grooves below, the tape assumed a zig-zag pattern. When the coils were vacuum-potted, the epoxy flowed into the mesh of the fiberglass tape, providing a cushion about each turn of wire. Sections of coils used in manufacturing test runs showed that the potting compound did indeed completely penetrate the windings.

The first coils made this way were models 4 and 5. After the winding process was completed, they were tightly toroidally

wrapped with 2.5-cm wide woven fiberglass tape to restrict motion of the windings. Polyester resin was used as the potting compound. This subsequently proved too brittle. Cracks developed after one or two full energy pulses on the coils. The Model 5 coil proved to be unreliable. The more conservatively designed Model 4 coil withstood at least 25 pulses at full energy before failure, with no additional surface cracking beyond that which occurred after the first few pulses.

Because of the cracking problem, a search was made for a potting compound resilient enough to prevent the occurrence of cracks, yet tough enough to rigidly hold the coil windings. Adiprene proved to be an ideal material. Its use eliminated the necessity of toroidal wrapping of the coils with fiberglass tape, although the woven fiberglass tape between layers was retained. After winding, these coils were tied with straps to hold their shape during the potting operation. Figure 31 illustrates the Model 41 coil, which is now standard for the MGA project. Since whipping of the leads from the coil during pulse could result in breakage and failure of the magnet system, they were encased in copper tubing. This in turn was encased in "thermofit" shrinkable plastic tubing, which aids insulation of the leads both inside and outside the potted assembly. Connection was made to the RG-8/U coaxial cable transmission line (from the capacitor bank) with standard heavy electric cable clamps.

The coils as presently used have an inductance of about 1.9 mh each. When assembled, the total inductance of the system is about 4 mh. With the 230- $\mu$ f, 20-kv capacitor bank, peak magnetic field strengths up to 50 kgauss can be generated within the armature with a rise time of 1.8 msec. Figure 31 also shows oscillographs of the field buildup inside the armature and the current in the coil circuit.



# SPECIFICATIONS

<u>COIL</u>	<u>POTTING</u>
OD 101.6 mm	131.3 mm
ID 50.8	40.64 mm
LENGTH 50.8 mm	66.04 mm
20 TURNS PER LAYER, 10 LAYERS	
NO. 10 DOUBLE FORMVAR	
ENAMELED COPPER WIRE	

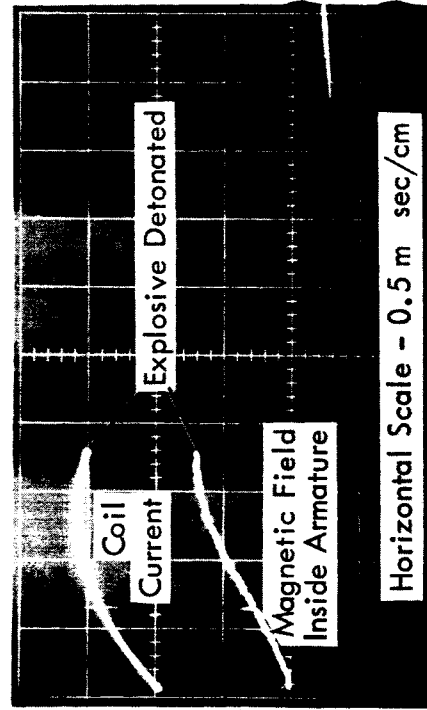


FIGURE 31. CROSS SECTION OF CAPACITOR DRIVEN COIL



## 2. Attractive Coil Motion

The COIL computer program<sup>9</sup> was employed to calculate the peak magnetic attraction forces for typical coil spacings in the test device. Table IV lists the results of these computations.

TABLE IV  
COMPUTED ATTRACTIVE FORCES BETWEEN  
THE MGA MAGNET COILS

Separation Between Coil Potting Surface and End Confinement Plate (mm)	Center-to-Center Coil Spacing (mm)	Peak Force For Peak Current of 4700 amp (kg)
0	130.3	3,545
6.35	143.0	2,534
12.70	155.7	1,852
19.05	168.4	1,383
25.4	181.1	1,051

Because of the relatively long rise time of the magnetic field pulse, it was feared that the explosive, which was between the coils, might be cracked before detonation, thus upsetting the hydrodynamic performance of the device. An investigation of various means of restraining the coils showed this approach to be expensive and cumbersome, and would create an additional abundance of fragments from the explosion.

An alternate approach was to space the coils some distance from the explosive tamping discs and allow them to move inward during the 1.8 msec before the explosive was detonated. It was

---

<sup>9</sup>M. W. Garrett and C. E. Parker, COIL, Computer Program for Calculating the Force and Mutual Inductance Between Coaxial Coils, Oak Ridge National Laboratory.

believed that the spacing should be at least twice the distance of travel to allow for a margin of safety. Double integration of the acceleration due to the computed forces and measured mass of the coils indicated that when each coil was spaced 12 mm from the explosive tamping plate, they should move inward a distance of about 6 mm before detonation. This was for a sinusoidal pulse with a rise time of 1.4 msec (coil circuit). Several tests were run using a high speed motion picture camera. The results of these tests agreed well with the calculations, so the 12-mm spacing was used.

To simplify the experiment, a search was made for a material which could be inserted in this space and which would be stiff enough to support the assembly in the usual vertical firing position while absorbing the motion of the coils without transmitting significant force to the tamping plates and explosive. Thus the parts of the device could merely be stacked vertically and held in position by gravity. The best plastic foam material tried was Post-Pack, an instrument packaging material made from polyurethane foam and available in cylindrical billets of the same diameter as the coils. Thus, it was a simple matter to slice off 12-mm thick discs to use as the shock absorbers.

This technique appears to be quite satisfactory. Test shots showed no degradation of explosive performance. Its usefulness was more dramatically demonstrated, however, in an experiment where an electronic failure caused discharge of the capacitor bank just before the firing key was depressed. Since the explosive was not fired, a detailed inspection was made of the experiment components. No damage of any kind could be found to explosive or non-explosive components, and the coils were merely displaced somewhat from the axis of the system. The device was realigned and a successful experiment subsequently conducted.

## V. SPECIAL INSTRUMENTATION

Instrumentation for observation of the projectile has been a particular problem in this program. The high expected velocities, obscuring gaseous material, and the difficulty of probing the interior of the MGA for in situ diagnostics have compounded the problem. A variety of techniques has been considered. Several which appear to have particular merit were tested. Two were put into practice.

### A. FLASH X-RAY

High energy flash x-ray was considered for direct particle observation. Two time-separated exposures were possible which could be used to record either particle position during field compression or measure particle velocity. The amount of material (lucite detonator ring, explosive pad, aluminum armature, and copper flux concentrator) forming the background against which the small aluminum particle must be resolved made the probability of success marginal at best. A feasibility test using a 0.76-mm diameter aluminum ball contained inside a special two-slot ( $180^\circ$  separation) copper flux concentrator was conducted. Several attempts at both 300-kv and 250-kv settings of the flash x-ray machine were made. Visual examination of the film negatives and prints failed to reveal the sphere. Negatives were submitted to isodensitometer examination but this also proved fruitless.

In-flight flash x-ray of the projectile outside of the accelerator was also considered. In order to obtain definitive photographs, however, the basic requirements of x-ray technique required that the film cassette be so close to the test device that it would not be able to survive the explosion. This was because of the very small size of the projectile.

## B. PROJECTILE FLIGHT CHAMBER

The cloud-like luminous effusion observed during Phase I (Contract NAS8-5266) of this program suggested the presence of detonation products and/or vaporized material which could obscure any ejected projectile. A detection chamber was designed for the dual purpose of restraining gases and providing an optical indicator of material ejected from the accelerator. This device is illustrated in Fig. 32. The 0.0125-mm thick aluminized mylar foils would allow penetration of a solid mass such as the projectile but would inhibit passage of gaseous material. The shock waves induced in the terminal lucite block would indicate the size, mass, and velocity of solid or gaseous material which impacted upon it.

The optical arrangement for framing camera observation is also shown in Fig. 32. A plano-convex lens was located directly behind the chamber. This collimated light from an exploding bridgewire. The bridgewire was located at the focal point of the total optical system including the camera, the chamber, and the lens. This position was found by back-projecting an image of the framing camera aperture stop through the system to a screen located on the firing table behind the lens.

This instrumentation technique proved useful in a number of experiments for determining the character of material being ejected from the accelerator (see Section VI).

## C. INTERNAL PROJECTILE OBSERVATION

Direct observation of the projectile inside the flux concentrator during the magnetic compression is extremely difficult. The restricted opening through the field coils and into the flux concentrator throat inhibits not only the optical path but, more importantly, makes it difficult to provide adequate lighting arrangements. Under the most favorable conditions, photographing a small spherical object against a

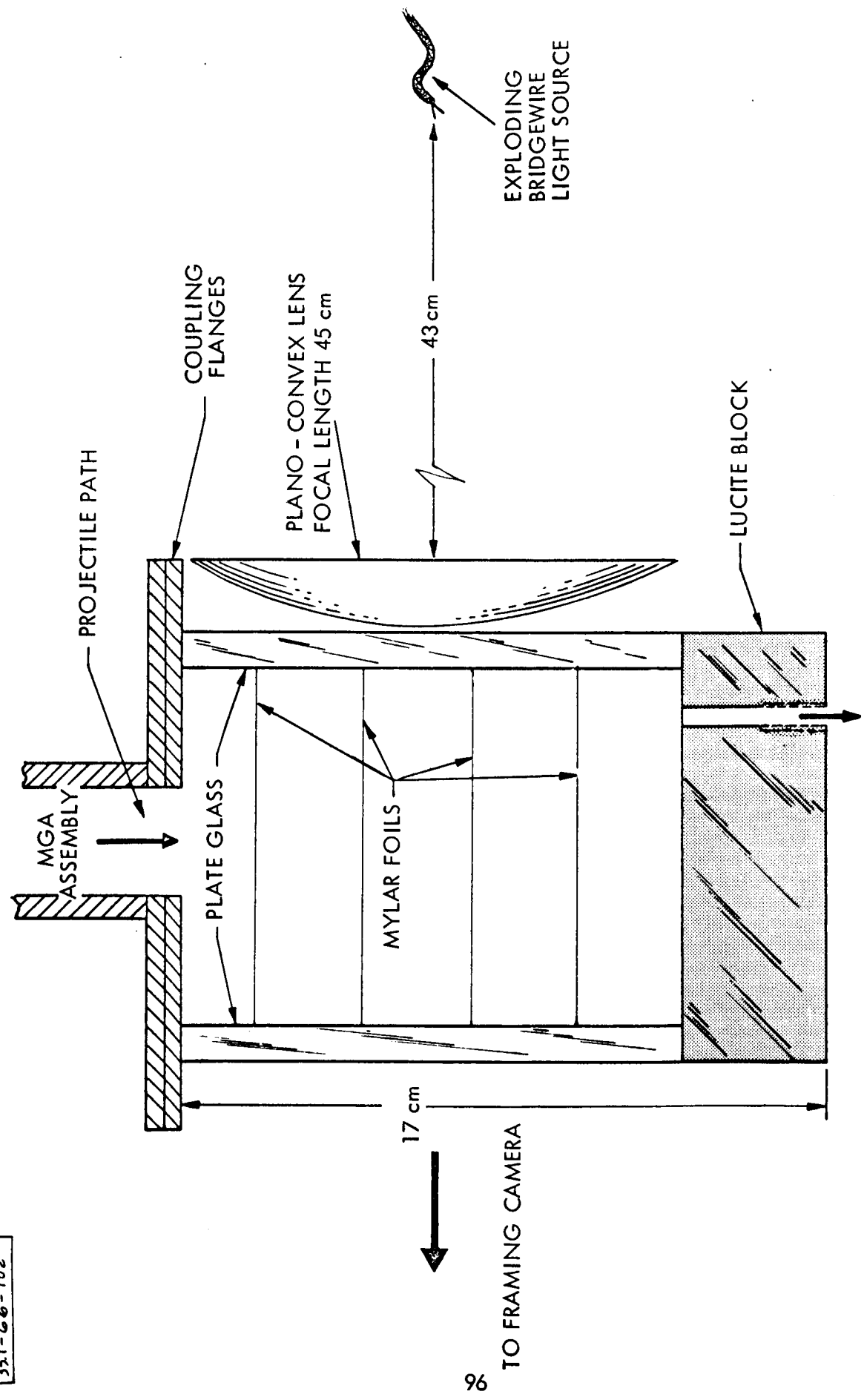


FIGURE 32. CHAMBER FOR EXTERNAL PROJECTILE DIAGNOSTICS

dark or neutral background is difficult since curved surfaces produce highlights which may obscure surface details. Also, the short exposure time per frame (down to  $0.15 \mu\text{sec}$ ), coupled with an unavoidable attenuation of 75% in the beam splitting mirror, demanded an exceptionally brilliant light source. The development of a usable technique, therefore, required a considerable effort.

Evolution of the final arrangement involved several intermediate designs and a number of tests. A xenon flash lamp was tried, unsuccessfully, as the light source. Explosive argon candles were considered, but found to be unsuitable. Moreover, their use also precluded pre-shot dry runs. Exploding bridgewires, however, offered a small source size and high intensity. Eight tests of these bridgewires were run with different energy inputs. Bare wires were found to be inadequate, but enclosure of the wire in a small (2-3 cm) saran balloon of argon proved to be satisfactory. This miniature argon candle was focused on the projectile in order to maximize the illumination. A 1575-joule capacitor discharge ( $14\text{-}\mu\text{f}$ , 15-kv) exploded the 1-cm long, 0.05-mm diameter Almag wire. Eastman type 2475 Data Recording Film was used, developed for 18 minutes in D-19 developer to a sensitivity equivalent to about ASA 4000.

The final design of the complete system is illustrated in Fig. 33. The first objective lens magnified the image about a factor of 18 so that it occupied most of the camera's field of view. This lens was adjusted to focus its first image point some distance in front of the camera. A field lens was placed at this location, and the camera focused there.

Although this design was the simplest which could be used with the available framing camera installation, some of its adjustments were extremely critical. For example, a 1-mm change in the first

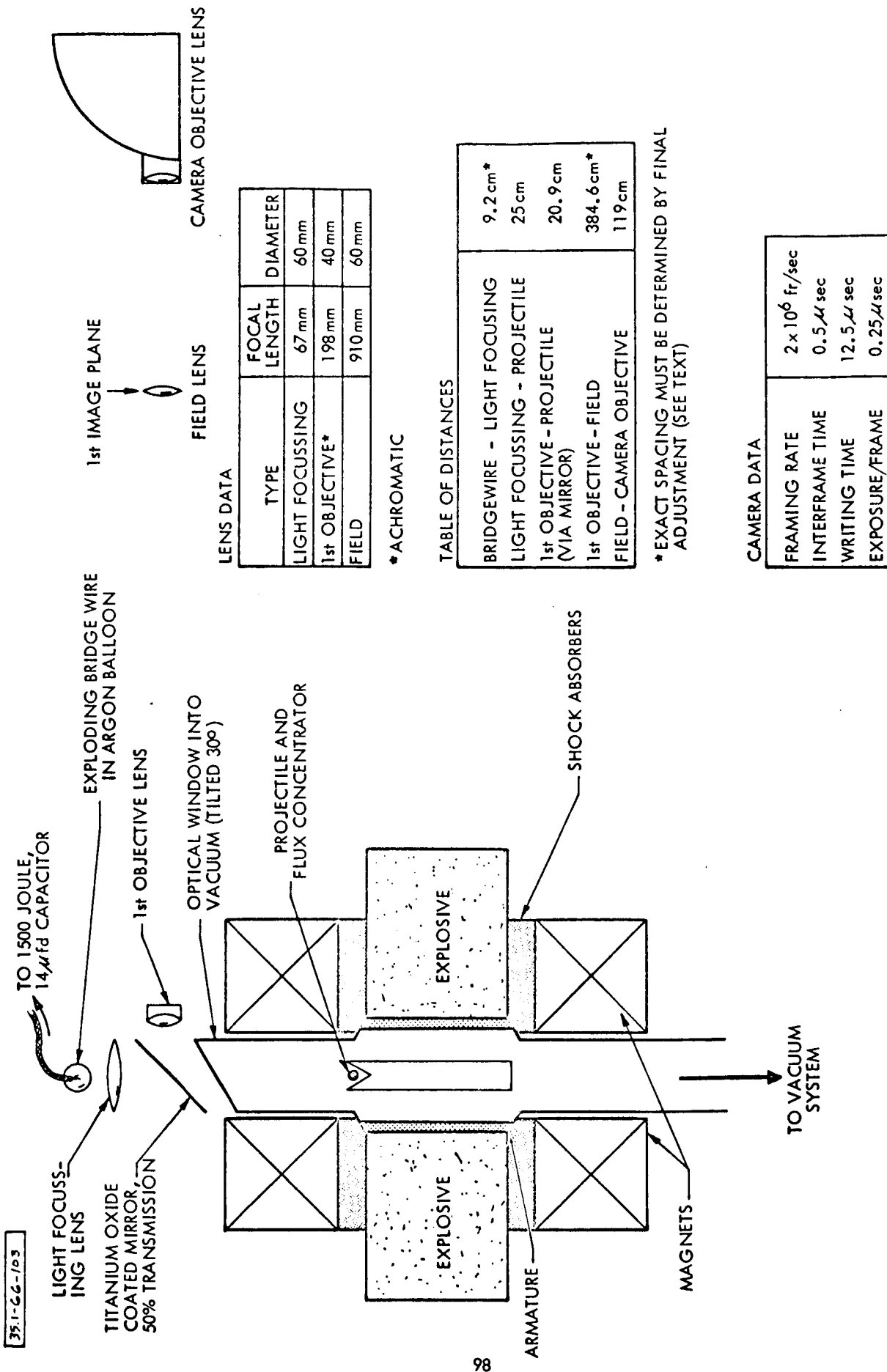


FIGURE 33. OPTICAL ARRANGEMENT FOR OBSERVING PROJECTILE DURING MAGNETIC COMPRESSION

objective lens-projectile distance would cause a change of about 1 m in the first objective lens-field lens distance. Thus, the design of the experiment had to allow for small adjustments of the optical components. A considerable amount of experimentation with different methods of assembly was also necessary. Techniques had to be developed for properly adjusting the system in a reasonable length of time.

Adjustment was accomplished as follows: a lamp was placed at the camera eyepiece, thus projecting an image of the eyepiece cross hairs to the shot. The test device, including the first objective lens and mirror, was then adjusted to bring it onto the optical axis. The field lens was then placed at the calculated position and centered on the cross-hair image. The first objective lens and mirror subassembly were then adjusted to place the center of the cross hairs on the projectile. The light focusing lens was then installed at its proper distance and the lamp at the camera removed. Another small dc lamp was placed at the light source position and adjusted for sharp focus of the lamp filament on the projectile. The first objective lens and mirror were then given a final alignment check by sighting through the camera. If necessary, they were adjusted to put the projectile image at the center of the camera field of view.

The mirror also projected the lamp image behind the optical assembly. That focus point was found with a screen and a second small lamp accurately located there. The first lamp was then removed. The mirror and light focusing lens back-projected the second lamp, focusing it at the light source location. The bridgewire-argon balloon assembly could then be accurately positioned by looking for maximum light reflection from the bridgewire.

With the camera set for critical focusing, the axial position of the first objective lens was adjusted for the clearest image in the



camera. The field lens camera distance was not particularly sensitive and could be varied up to 25% greater than the calculated distance shown in Fig. 33.

The optical window into the vacuum was placed at a  $30^{\circ}$  angle to keep its reflection of the light source from interfering with the image of the projectile. This angle caused the reflection to intercept the bottom of the mirror instead of the center, but was less than Brewster's angle, which would have caused total reflection. This would have prevented illumination of the projectile.

## VI. EXPERIMENTS

During the first 12 months of this contract, explosive experiments were conducted by Stanford Research Institute, under subcontract. In addition to the use of their facilities, SRI also provided scientific and engineering support. By the end of this period, AGN's explosive facility was operational. Thus the experimental work was done there during the last six months.

In addition to the regular magnetic gradient accelerator experiments, many peripheral tests were performed. Peripheral tests were defined as those which did not involve detonation of the MGA main explosive charge.

### A. PERIPHERAL TESTS

In order to conduct the full-scale MGA experiments it was necessary to develop and test certain sub-systems and components. These peripheral tests were both explosive and non-explosive and totaled 77 in number. Almost all were concerned with problems unique to the design and testing of the magnetic gradient accelerator configuration and its instrumentation. A few tests involved standard techniques, applied in the MGA experimental system. This section lists only those utilizing explosives. Other "bench tests" are described in Section IV.

#### 1. End Plate Confinement

This investigation tested the effect of explosive tamper density on armature axial curvature for the purpose of minimizing this effect. Details are given in Section IV.A.3. The individual shots are listed in Table V.

TABLE V  
EXPLOSIVE END CONFINEMENT TESTS

<u>Shot Number</u>	<u>Description</u>
SRI 9,977	X-ray observation of flying plate constrained by stainless steel plates
10,031	Streak camera observation of detonation breakout of Comp B pad confined between end plates of stainless steel and phenolic
10,032	Same as Shot 10,031 except confinement was by stainless steel and air

2. Detonator Firing Simultaneity

The detonator simultaneity tests were run for two purposes: to test jitter performance of different types of detonators, and to relate this performance to the design of the three different firing systems which were tried. The results of these tests are given in Section IV.A.1. The individual tests are listed in Table VI.

3. Shaped Charge Jets

An economical method of simulating the effusion observed in early MGA experiments was needed to develop required optical techniques. Shaped charge jets possess the necessary characteristics, thus tests were conducted to find a suitable design. Figure 34 shows the typical shaped charge jet construction. A cardboard tube packed with C-3 explosive was fitted around the metal cone and detonated at a single point on the axis. Inhibited shaped charge jets contained a lucite insert, as shown, which limited the mass of metal extruded in the jet; uninhibited charges had no insert. The tests conducted are listed in Table VII.

TABLE VI  
MULTIPLE DETONATOR SIMULTANEITY TESTS

Shot Number	Description
SRI 10,715	Streak camera measurement of detonation simultaneity of PL-2 detonators fired from standard 200-joule firing unit
10,716	Same as Shot 10,715 except SE-1 detonators used
10,743	Streak camera measurement of PL-2 detonation simultaneity; parallel connected to 200-joule firing unit
10,744	Repeat of Shot 10,743
10,745	Same as Shot 10,743 except with SE-1 detonators
11,051	Streak camera observation of detonation simultaneity. PL-2's and modified firing unit
11,052	Same as Shot 11,051 except 24 SE-1's fired with modified firing unit
11,054	Repeat of Shot 11,052
AGN 50	Streak camera measurement of detonation simultaneity. 24 PR-500 detonators and non-expendable low inductance slave unit firing system
51	Repeat of Shot 50 except with 12 SE-1 detonators
53	Repeat of Shot 51
54	Repeat of Shot 53

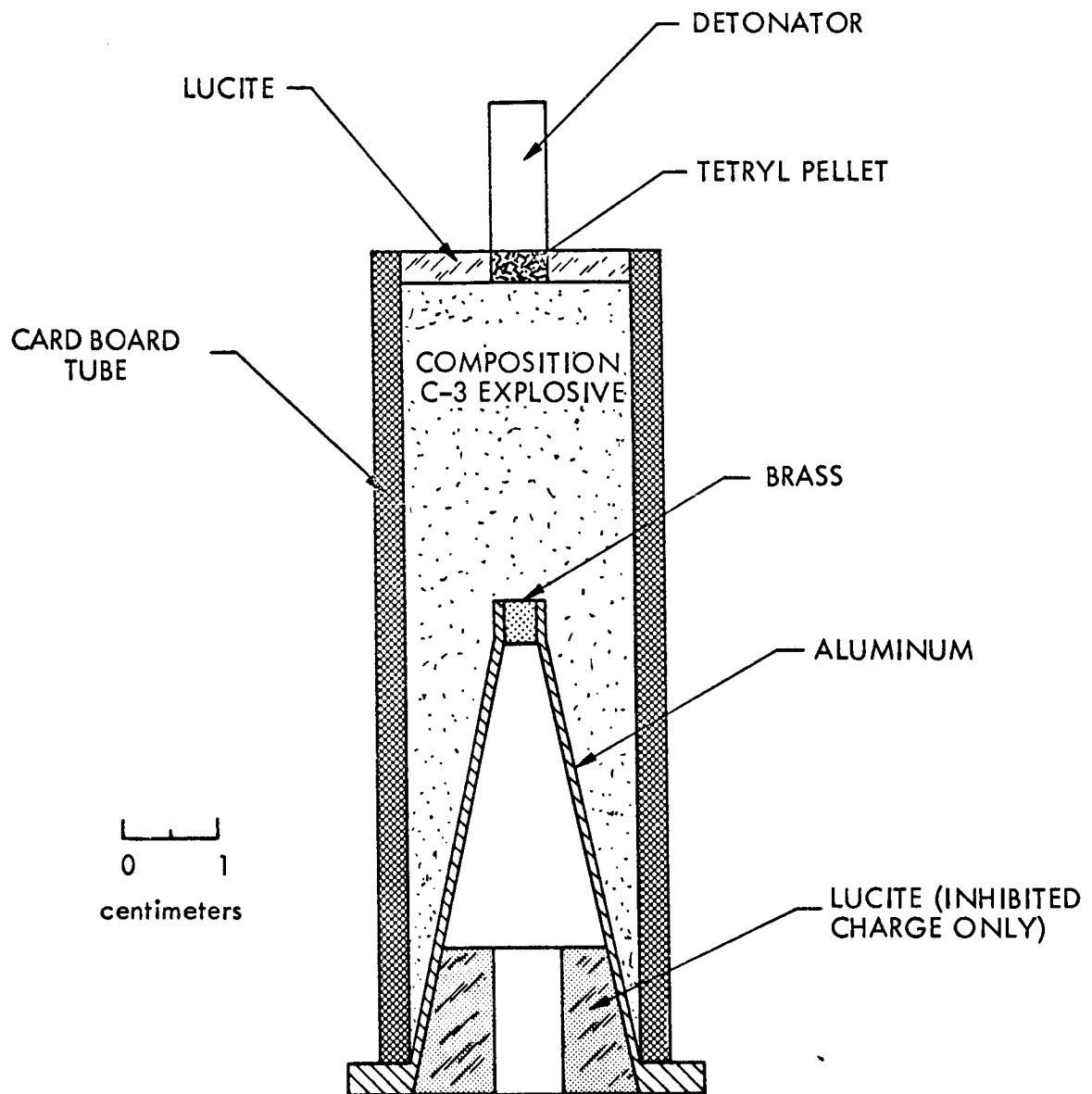


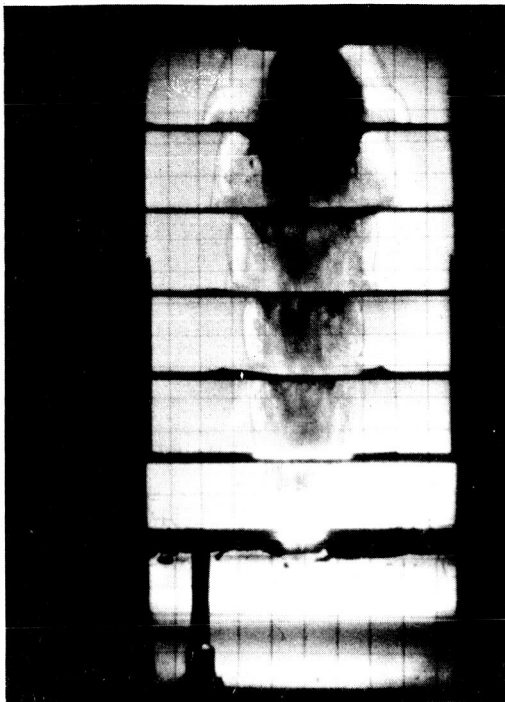
FIGURE 34. SHAPED CHARGE CONSTRUCTION

TABLE VII  
SHAPED CHARGE JET TESTS

<u>Shot Number</u>	<u>Description</u>
SRI 10,720	X-ray observation of shaped charge jet. 20° aluminum cone
10,721	X-ray observation of shaped charge jet. 30° aluminum cone
10,722	X-ray observation of shaped charge jet. 25° aluminum cone
10,723	X-ray observation of shaped charge jet. 30° aluminum cone--lucite inhibited
10,747	Framing camera observation of shock wave in lucite from impact of shaped charge jet
10,748	Repeat of Shot 10,747
10,776	Development of framing camera optical technique for observing shaped charge jets
10,871	Development of framing camera optical technique with projectile flight chamber
11,172	Test of framing camera optical technique with final design of projectile flight chamber

The x-ray observations (Shot 10,720 to 10,723) showed that the uninhibited shaped charges produced diffuse jets. The 30° aluminum-insert inhibited charge produced a pellet about 5-cm long at a velocity of 7.63 mm/ $\mu$ sec.

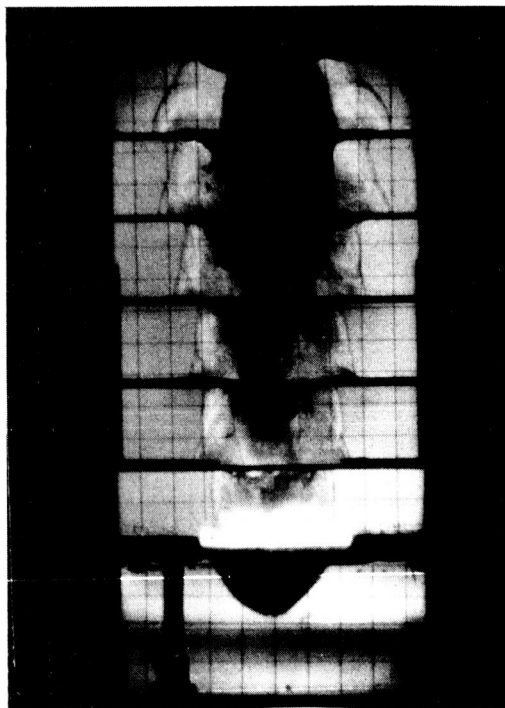
Figure 35 shows selected frames from Shot 11,172. This demonstrates the ability of the technique to resolve the presence of a compact mass such as the MGA projectile.



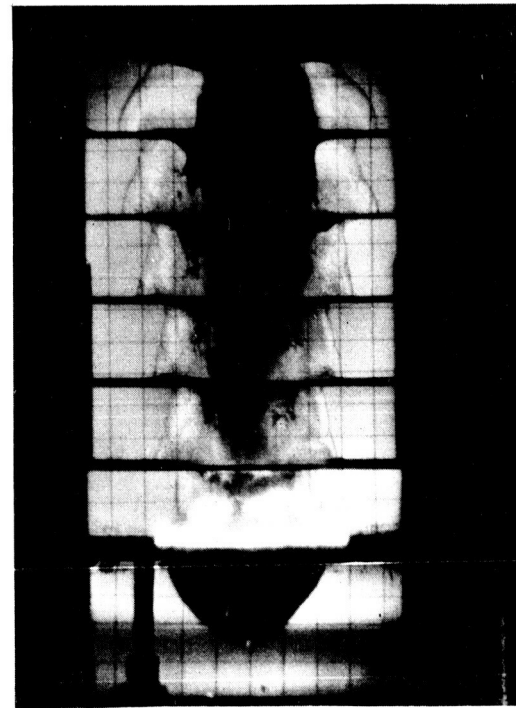
FRAME 19



FRAME 21



FRAME 23



FRAME 25

FIGURE 35. SELECTED FRAMES FROM SHAPED CHARGE JET TEST OF PROJECTILE FLIGHT CHAMBER AND LUCITE TARGET BLOCK. ( $1\mu$  sec/frame)

39.1-66-105

#### 4. Fast-Acting Shutter

High speed rotating mirror framing cameras, such as were used in the projectile experiments, contain a mechanical capping shutter which is opened briefly during the shot. This shutter prevents exposure of the film in the camera from stray light. Since the capping shutter is a mechanical device, however, the rotating mirror in the camera can make many revolutions during the time the shutter is open. Thus any bright light (such as from the explosion) which is generated after the desired data sequence can expose the film on subsequent revolutions. This is particularly true at very high camera speeds when the dead time between sweeps across the film is very short (film exposure time is typically  $1/10$  of 1 revolution). It is therefore necessary on some experiments to provide a rapid means of shutting off the light path to the camera.

Experiments conducted at SRI utilized their standard smoke shutter technique. Most of the framing camera work done at AGN, however, was at very high speeds and with low event illumination. The typical time for one revolution of the mirror was  $125 \mu\text{sec}$ , and film sensitivity equivalent to ASA 4000 was used. It was necessary, therefore, to conduct tests to insure the prevention of rewrite. These are listed in Table VIII.



TABLE VIII  
FAST ACTING SHUTTER TESTS

<u>Shot Number</u>	<u>Description</u>
AGN 67	20-cm diameter smoke shutter. X-cord light source
68	5-cm diameter smoke shutter. Argon candle light source
69	5-cm diameter lucite and sheet explosive blast shutter. Argon candle light source
70	5-cm diameter double detonator glass blast shutter. Argon candle light source

The smoke shutters were constructed by surrounding a hole in a plywood board with sheet explosive. Detonation produced sufficient smoke to appreciably attenuate light passing through the hole. These shutters proved to be too slow for reliable operation at camera speeds of 2 to 3 million frames per second, the speed required for the direct projectile observation experiments. The lucite blast shutter took over 50  $\mu$ sec to operate. The glass blast shutter using 2 SE-1 detonators shut off the light from the argon candle in about 20  $\mu$ sec. The pulverized glass also proved to be the best light attenuator. Details of this shutter appear in Fig. 36.

#### B. MGA DEVICE DEVELOPMENT

As described in Section IV, there was considerable redesign of the magnetic gradient accelerator at the beginning of this contract. After individual component development, it was necessary to test the operation of the complete new MGA system. Performance measurements were made of the explosive system and the peak magnetic field obtained.

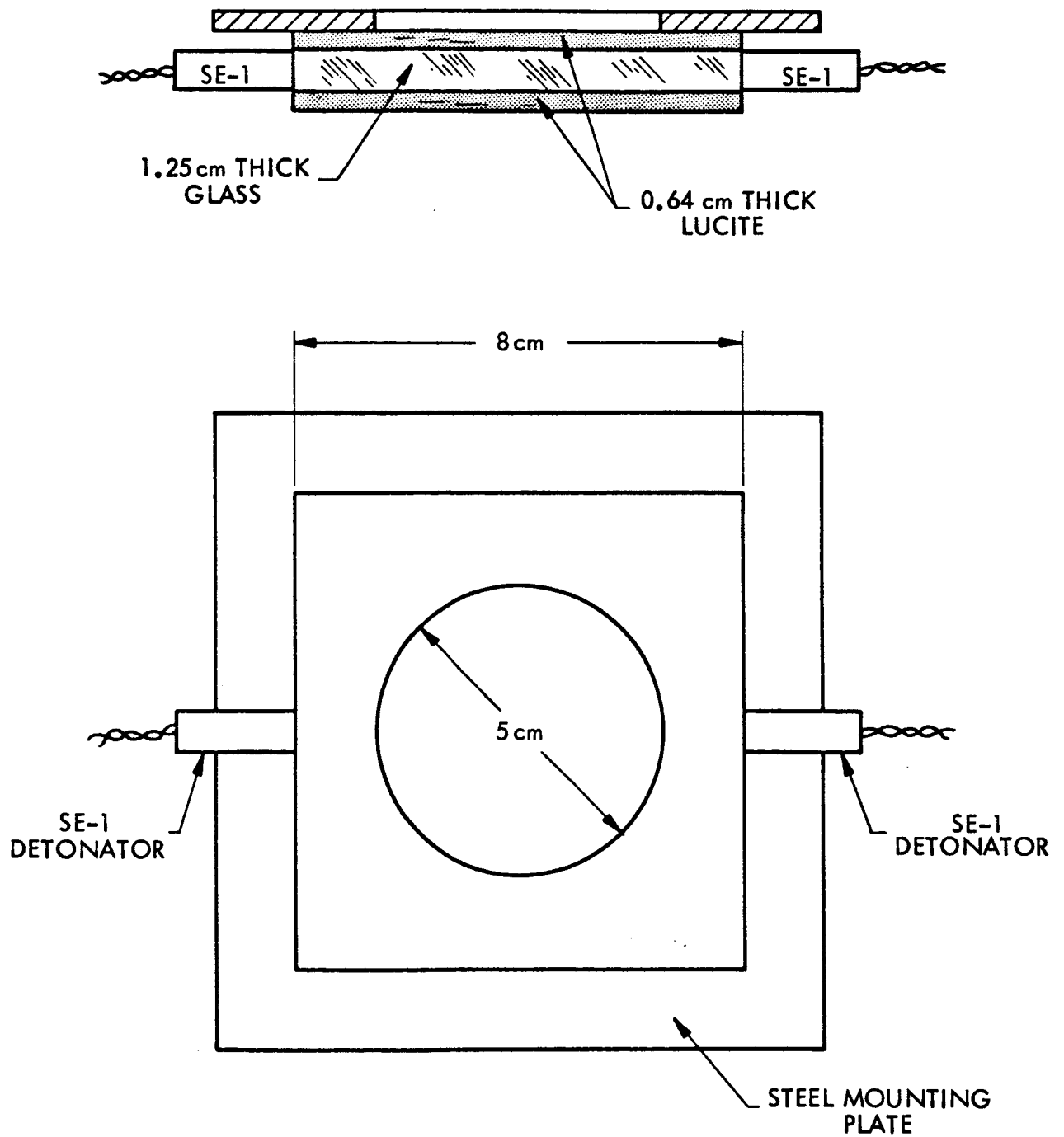


FIGURE 36. FAST ACTING BLAST SHUTTER

## 1. Description of Test Device

General details of the device design used in the development experiments are illustrated in Fig. 37. There were, of course, variations depending upon the purpose of each experiment. Shot 24, for example, required modification of one end plate and a spider mounting arrangement for the flux concentrator to allow for evacuation of the armature. Both long throat and short throat flux concentrators were used. These are described in Section VI.C below. The long throat design has shown a higher peak magnetic field capability than the short throat.

## 2. Description of Experiments

Details of the ten development experiments appear in Table IX. The shot numbers used in this table are from the MGA program sequence, not test facility shot numbers. Shots 1 through 6 were fired during Contract NAS8-5266. Shots 7 through 14 were fired at the SRI test site and were for the purpose of confirming the redesign of the MGA at the beginning of this contract. Shots 22, 23 and 24 were fired at AGN. Their purpose was to test the Aerojet-fabricated explosive and the special equipment installed in the AGN facility for MGA experiments.

As can be seen in the table, all experiments had hydrodynamic instrumentation. In all cases, this was with the fiber optic streak camera technique.<sup>10,11</sup> Shots 10, 11 and 22 were exclusively hydrodynamic. All the others had magnetic instrumentation for measuring the timed history of the magnetic field compression.

---

<sup>10</sup> Chapman, AN-1098, op. cit.

<sup>11</sup> R. C. Goettelman and J. K. Crosby, Optical Probe Techniques, RSI, November 1964.

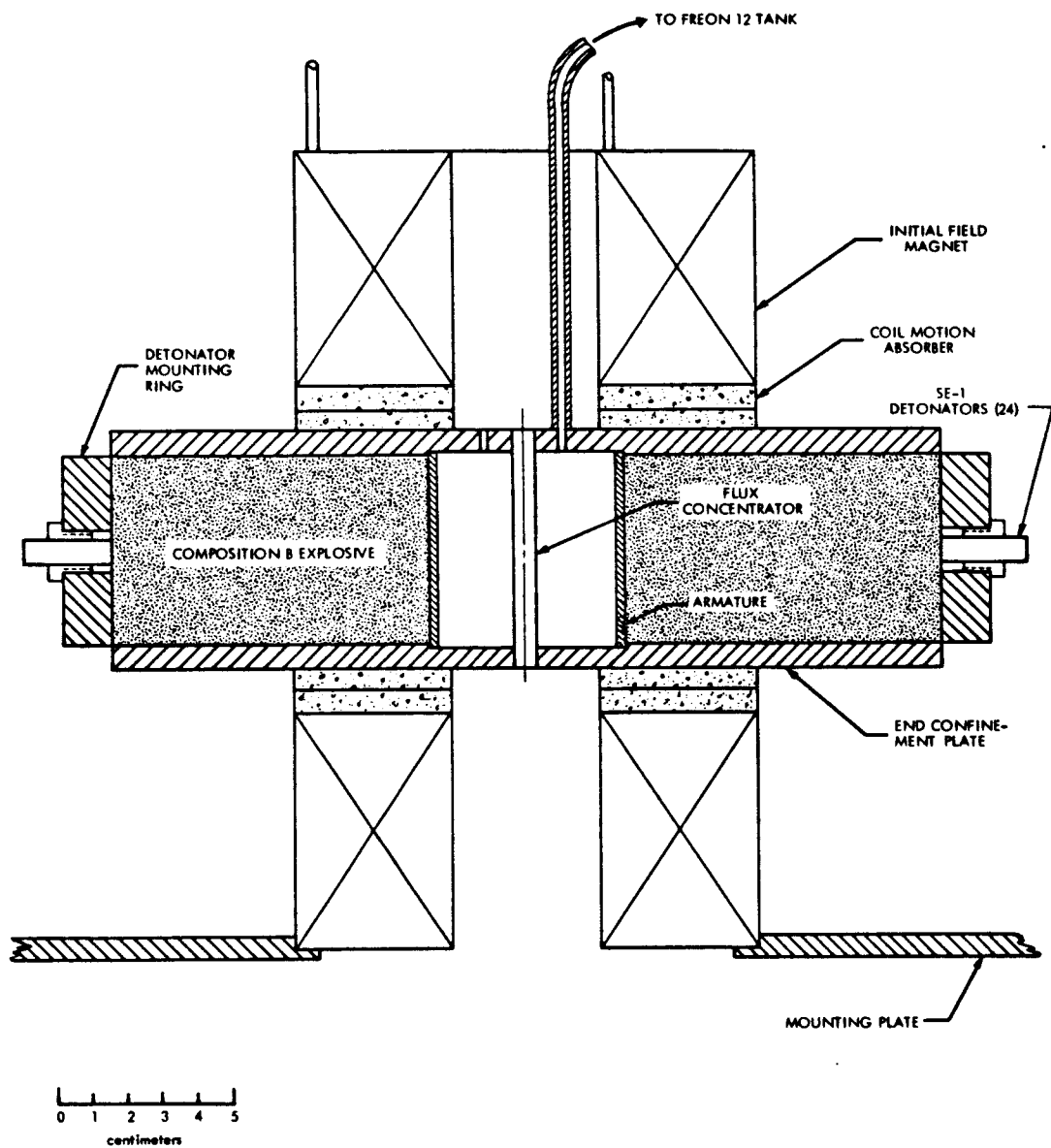


FIGURE 37. GENERAL DETAILS OF TEST DEVICE FOR DEVELOPMENT EXPERIMENTS

TABLE IX  
MGA DEVICE DEVELOPMENT EXPERIMENTS

MGA Shot	Purpose	Instrumentation	Flux Concentrator	Peak Field	H.E. Symmetry	Remarks
7	Hydrodynamic, magnetic test multiple detonators and capacitor-driven magnets	24 fiber optic bundles equally spaced on 7-cm radius	5-cm Long Throat	~ 3.4 Mgauss	Mean Variation 0.2 $\mu$ sec	Performance comparable to cylindrical wave initiator.
8	Same as 7	Same as 7	Same as 7	~ 2.5 Mgauss	Mean Variation 0.18 $\mu$ sec	Same as 7
10	Hydrodynamic, multiple detonators with modified firing system	24 fiber optic bundles on 6.6-cm radius, and 12 bundles on 2.9-cm radius	N/A	N/A	Poor	Skewing of detonation front due to machining errors in detonator mounting ring.
11	Same as 10	24 fiber optic bundles equally spaced on 6.6-cm radius	N/A	N/A	Mean Variation 0.03 $\mu$ sec	Good results. See Fig. 39 which shows typical performance.
12	Hydrodynamic, magnetic test without flux concentrator	Same as 11	None	1.6 Mgauss	No data	Loss of hydrodynamic data probably due to misalignment of fibers by magnet coil motion.
13	Repeat of 12	Same as 11	None	2.7 Mgauss	Mean Variation 0.03 to 0.04 $\mu$ sec	12 fibers obscured by smoke. Good results.
14	Repeat of 12	Same as 11	None	---	Mean Variation 0.02 to 0.03 $\mu$ sec	Initial field coil failed. Data from 11 fibers not usable because of excessive separation from H.E. Good results.
22	Hydrodynamic, multiple detonators with AGN systems and facility.	24 fiber optic bundles at o.d. of explosive, 24 fiber optic bundles at i.d. of explosive (all equally spaced)	N/A	N/A	Mean Variation 0.08 $\mu$ sec	Adequate performance.
23	Hydrodynamic, magnetic	24 fiber optic bundles on 6.8-cm radius	5-cm Short Throat	---	Mean Variation 0.02 to 0.03 $\mu$ sec	Timing failure lost magnetic data but initial B traces show compression occurred. Good results.
24	Same as 23, but with armature evacuated to $10^{-4}$ mm Hg	Same as 23	Same as 23	2 Mgauss	Mean Variation 0.12 $\mu$ sec	Poor performance. Most probably caused by a flaw in the main explosive charge.

This was accomplished with small search coils and 50- $\mu$ sec integrators. All magnetic data was normalized to the peak value in the 0.2-mm hole formed by the assembly of the three flux concentrator segments.

The initial magnetic field strength within the armature was about 40 kgauss (in the magnetic shots). Initial field values measured inside the flux concentrator have been consistently lower (25 to 35 kgauss). This was first noted on Shots 7 and 8. Bench tests were run after Shot 8 in which the initial magnetic field was simultaneously measured inside and outside the flux concentrator. These tests showed that the flux density outside the flux concentrator, but within the armature, was comparable to that measured during the development of the magnet system (Section IV). The flux density inside the concentrator was not only lower than that outside, but also had an axial gradient within the throat, decreasing in value from the end to the center. As yet, there has been no satisfactory explanation of this phenomenon. The flux concentrator slots should allow free passage of flux lines to the interior.

Shot 11 was the first to achieve really good explosive system symmetry performance. It is fairly typical, however, of subsequent performance. A photograph of this shot before firing is shown in Fig. 38. The streak camera record of this shot and a polar plot of the data are shown in Fig. 39. The radial dimension is exaggerated for clarity. The explosive symmetry data shown in Table IX for Shots 13 and 14 are only for those fibers giving usable signals.

### 3. Conclusions

These experiments have shown that the redesigned MGA has much better performance potential than the flying cone cylindrical wave initiator, battery-driven liquid nitrogen cooled coil system. This increased performance was necessary for meaningful experiments with projectiles.

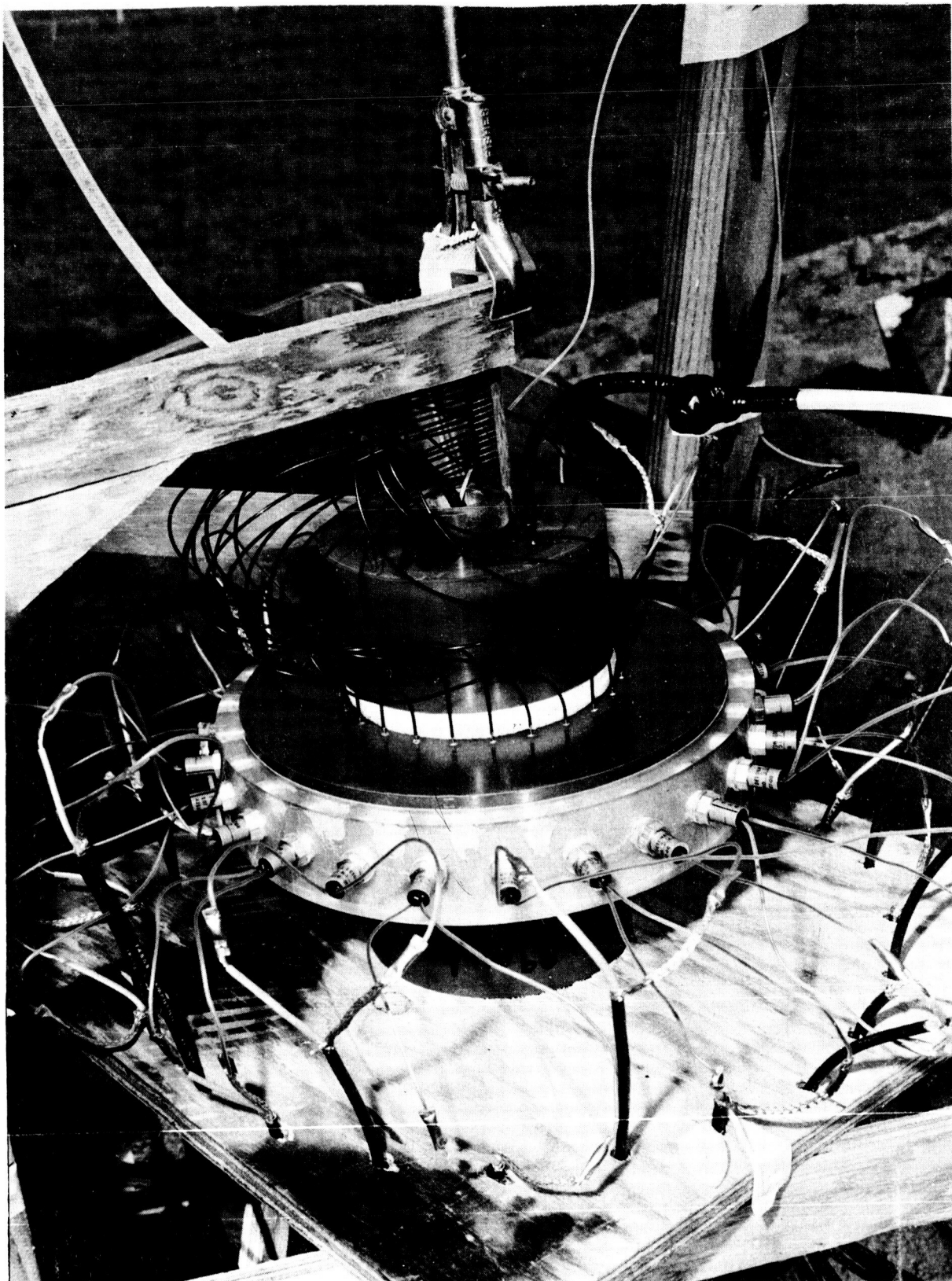


FIGURE 38. MGA INSTRUMENTED FOR DESIGN PERFORMANCE EXPERIMENT

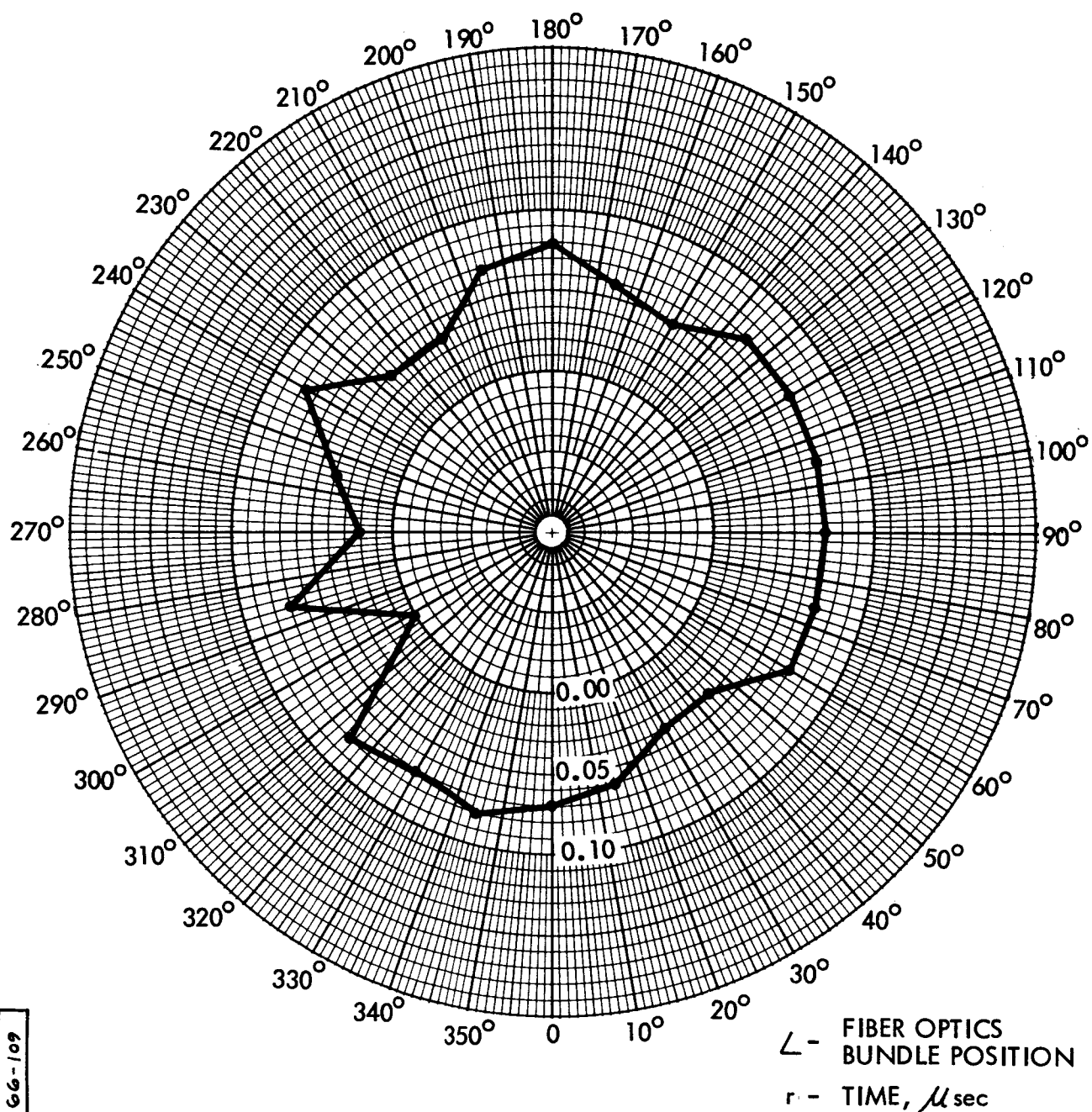
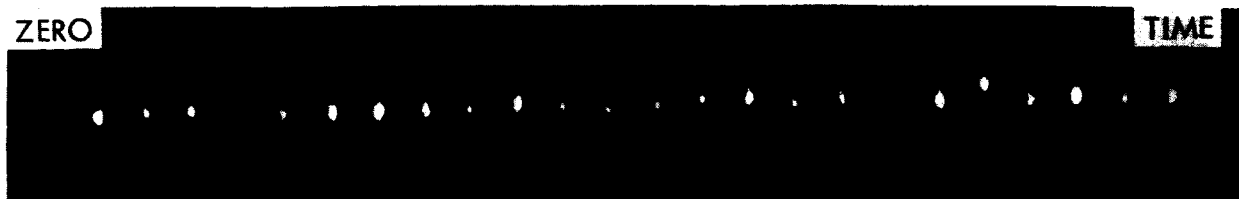


FIGURE 39. CIRCULAR SYMMETRY OF DETONATION, MGA-11

35.1-66-109



### C. PROJECTILE EXPERIMENTS

Once satisfactory test device performance was achieved, the program was directed to its primary purpose: projectile experiments. Many techniques were considered for making meaningful measurements and observations. The small projectile size, the high velocities expected, and the severe environment precluded most standard and straightforward approaches. The transient and destructive nature of the experiments also imposed limitations on the application and types of equipment which could be used. The design of the experiments reflects the most practical, yet useful, methods which could be employed within the financial structure of the contract.

The purposes of the experiments varied. The first two were of standard design, with aluminum projectiles, and instrumented to detect projectile impact. When the framing camera records showed a high velocity luminous cloud but no evidence of solid impact, the decision was made to fire shots designed to isolate the reason or reasons. These included shots to determine if the observed luminous cloud came from the projectile, flux concentrator wall, or the gas-filled space between flux concentrator and armature. Possible trapping of the projectile by an inward motion of the flux concentrator wall was investigated. The last four shots were especially instrumented for direct observation of the sphere.

#### 1. Description of Test Devices

The basic hydrodynamic and magnetic design of the test devices used for the projectile experiments was unchanged from that described in Section VI.B above. Certain variations of detail were required, however, depending on the particular experiment design. For example, in the projectile flight chamber shots the flux concentrator interior had to be evacuated when the chamber was evacuated, as a

vacuum barrier across the MGA outlet pipe was undesirable. The flux concentrator, therefore, had to have a vacuum seal around its outer surface; also, it was vacuum sealed into the lower explosive tamping plate. Flanges were also required for assembly since the projectile viewing chamber was fabricated separately. When it was decided to evacuate the armature also, another design variation was required. The armature had to be vacuum sealed to the end plates, but this had to be done on the firing table, since the explosive charge had to be installed first. Ultimately, some changes were made which permitted more vacuum assembly work to be done in the shop. Figure 40 shows the design details as they existed at the end of the contract.

Several different flux concentrator designs were tested. These are illustrated in Fig. 41. All flux concentrators were fabricated from oxygen-free copper and insulated with 0.1-mm thick teflon adhesive tape. Shots 19 through 21 are shown to have 2.5-cm long flux concentrators. These were all of the short taper type. The ends of these flux concentrators were identical to those 5 cm long. The effect was to move the projectile closer to the center plane of the system. Shots 18 through 21 used the shortened flux concentrator. The explosive thickness and armature length were also reduced accordingly. A photograph of the three unassembled segments of a 5-cm double-ended short inside taper flux concentrator is shown in Fig. 42. The double-ended design permitted taking internal magnetic field strength measurements without the search coils interfering with the projectile. After segment assembly, the flux concentrators were wrapped with about 500 turns of fine silk thread, and spray-coated with plastic. This made a rigid, vacuum-tight unit.

All projectiles used in these experiments were spheres. The aluminum projectiles were solid and of chemically pure material.

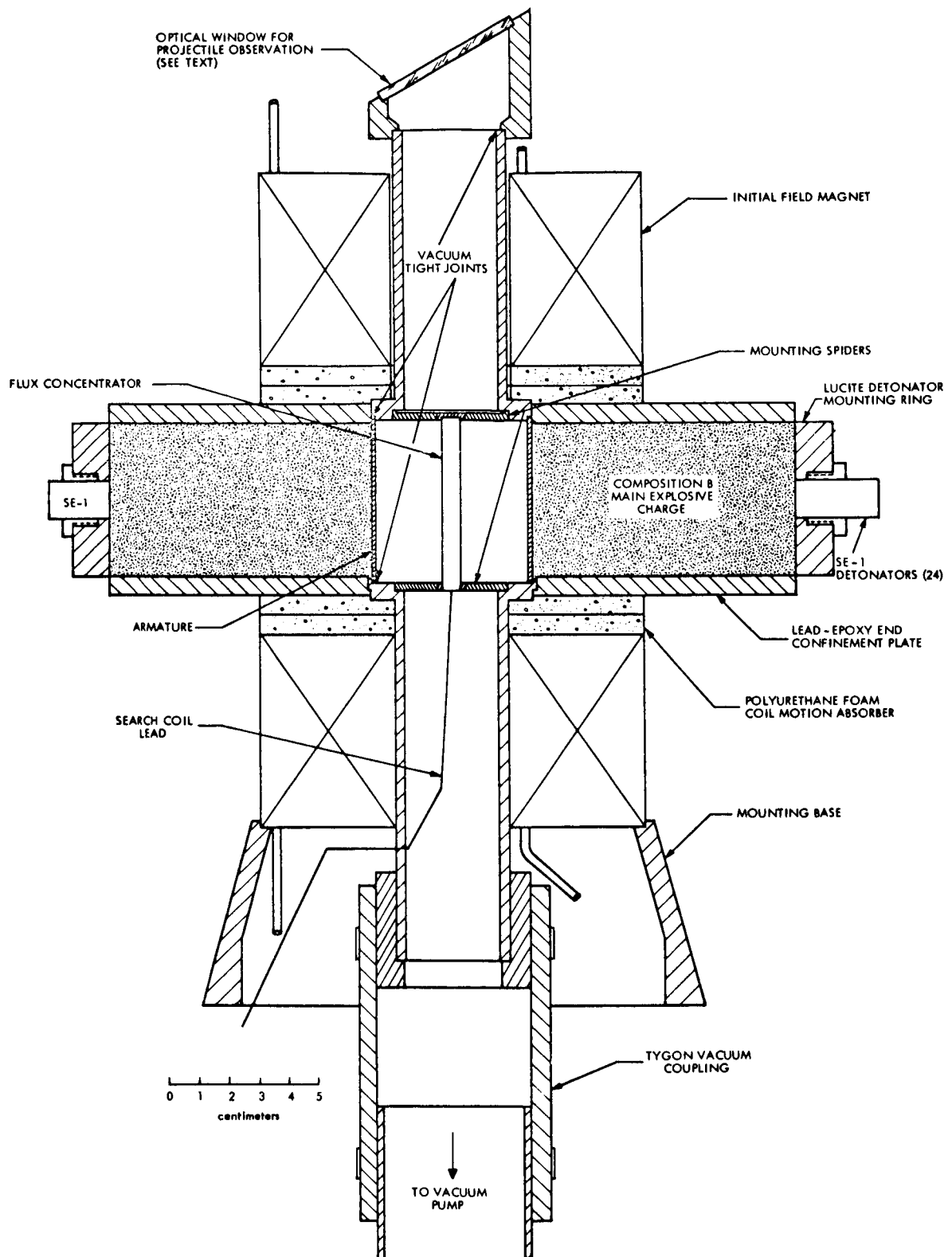


FIGURE 40. FINAL DESIGN OF MGA AS USED IN DIRECT PROJECTILE OBSERVATION EXPERIMENTS

EXCESS LENGTH FOR MOUNTING  
 0.2mm HOLE FORMED BY ASSEMBLY OF 3 SEGMENTS. ALL OD 6.35mm

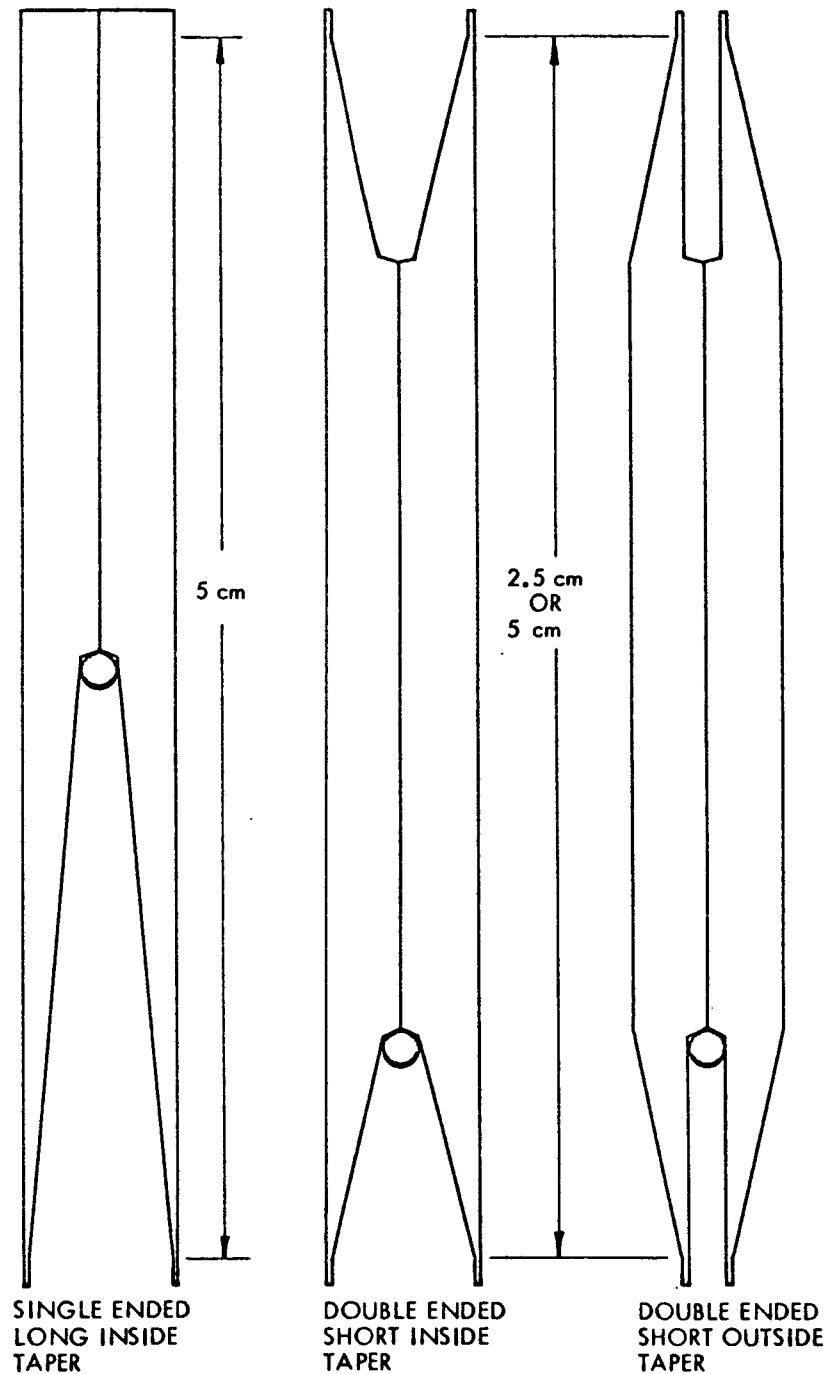


FIGURE 41. DETAILS OF FLUX CONCENTRATORS

351-66-111

35.1-65-2064

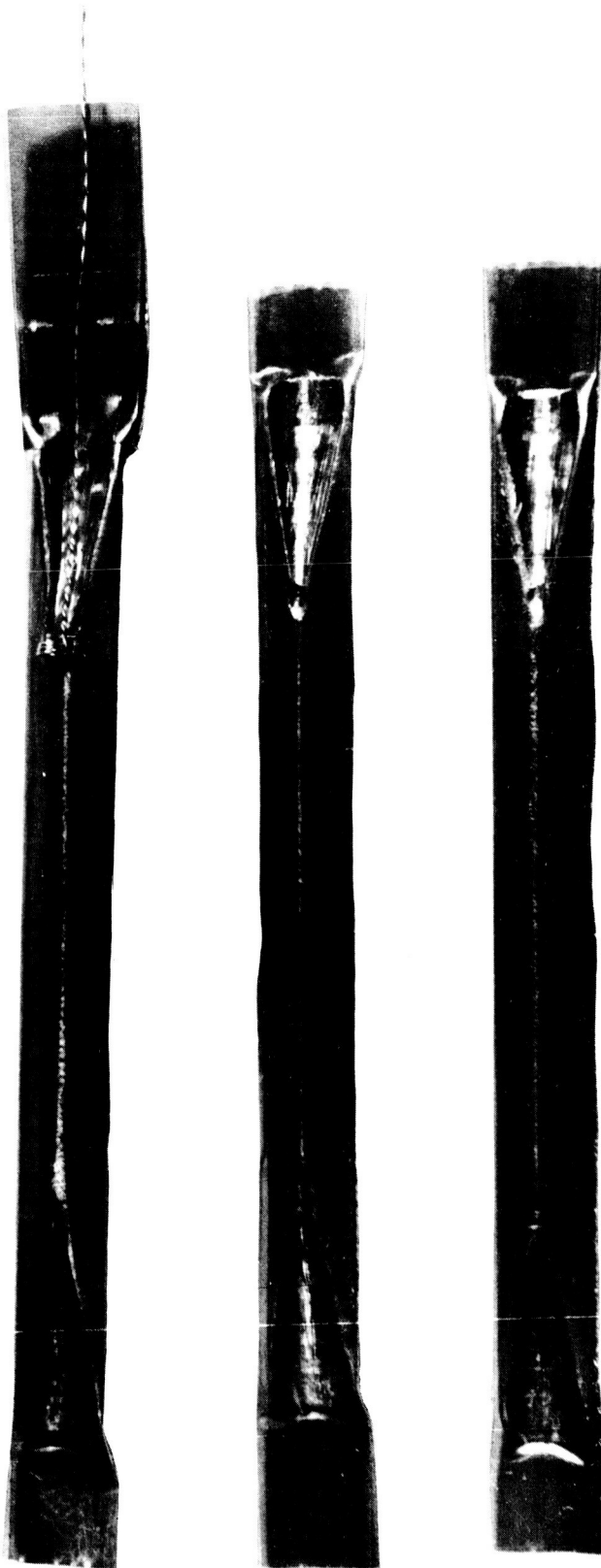


FIGURE 42. COMPLETED SEGMENTS OF 5 cm LONG, DOUBLE ENDED SHORT  
INSIDE TAPER FLUX CONCENTRATOR, AND SEARCH COIL

Shot No. MGA	Purpose	Instrumentation	Vacuum
6	Detect projectile	Framing camera viewing outlet pipe piezo-electric crystal	None
9	Detect projectile	Framing camera and projectile flight chamber	Flux concentrator flight chamber 500 $\mu$ Hg
15	Study effusion with no projectile	Framing camera and improved projectile flight chamber	Flux concentrator and chamber 150 $\mu$ Hg
16	Test short throat flux concentrator	Same as Shot 15	None
17	Test outside taper flux concentrator	Same as Shot 15	None
18	Test 2.5-cm thick MGA system	Same as Shot 15	None
19	Test copper-coated dielectric projectile	Same as Shot 15	None
20	Test outside taper flux concentrator in 2.5-cm thick MGA	Same as Shot 15	Flux concentrator and flight chamber, 100 $\mu$ Hg
21	Test copper-coated dielectric projectile with outside taper concentrator and 2.5-cm thick MGA	Same as Shot 15	Flux concentrator and flight chamber 60 $\mu$ Hg
25	Test for source of luminous cloud	Same as Shot 15	Armature, flux concentrator and flight chamber, $10^{-3}$ mm Hg
26	Observe effects on projectile during magnetic compression	Framing camera and magnifying optical system (see Sec. V.B)	Armature, flux concentrator, $6.4 \times 10^{-4}$ mm Hg
27	Same as Shot 26	Same as Shot 26	Armature, flux concentrator, $9 \times 10^{-5}$ mm Hg
28	Same as Shot 26	Same as Shot 26	Armature, flux concentrator, $5 \times 10^{-5}$ mm Hg
29	Same as Shot 26	Same as Shot 26	Armature, flux concentrator, $3 \times 10^{-4}$ mm Hg
30	Check for radial projectile motion, confirmation of Shot 29	Same as Shot 26	Armature, flux concentrator, $3 \times 10^{-5}$ mm Hg
31	Same as Shot 30	Same as Shot 26	Armature, flux concentrator, $1 \times 10^{-4}$ mm Hg

TABLE X  
MGA PROJECTILE EXPERIMENTS

Flux Concentrator	Projectile	Peak B	Cloud Velocity	Target Shock	Cloud Characteristics	Remarks
5-cm single-ended long inside taper	Aluminum 0.8-mm diameter	5 Mgauss	10.5 km/sec	N/A	Bright, coherent, spherical front	Piezoelectric crystal recorded sharp impact. > 20 kilobars.
Same as Shot 6	Aluminum 2-mm	5.8	11	10 kilobars	-----	Cloud velocity higher than predicted. Reached target before frame 1.
Same as Shot 6	Glass 2-mm	7.1	9.4 average	2	Bright, coherent, but tenuous. Easily slowed by mylar films.	Highest Peak B of program.
5-cm double-ended short inside taper	Aluminum 1.5-mm	3.4	5.4	---	Initially bright, coherent. Cooled and spread rapidly.	Cloud slower than predicted. No target impact recorded.
5-cm double-ended short outside taper	Aluminum 1.5-mm	2.6	6.6	--	Bright, coherent. Similar in appearance to MGA-6.	Same as Shot 16. One magnet coil failed.
2.5-cm double-ended short inside taper	Aluminum 1.5-mm	3.6	7.2	20	Bright, coherent, irregular front	Shots 18 and 19 show identical clouds, with and without magnetic field.
Same as Shot 18	copper-coated quartz, 1.5-mm, $\rho = 6.1 \text{ gm/cm}^3$	0	9.5	9-10	Same as Shot 18	Initial field magnet failed.
2.5-cm double-ended short outside taper	Aluminum 1.5-mm	3.4	10.2	2	Dark, very diffuse jagged front	Most diffuse and irregular of all clouds observed.
Same as Shot 20	copper-coated quartz, 1.5-mm, $\rho = 5.2 \text{ gm/cm}^3$	~ 3.5	--	4	-----	Camera late, timing error caused by electronic failure.
5-cm double-ended short inside taper	Aluminum 1.5-mm	---	5.6	--	Bright, relatively coherent	Cloud originates in flux concentrator, not armature.
Results						
Same as Shot 25	Aluminum 1.5-mm	---	N/A	N/A	---	Timing system failure caused by spurious pulses from faulty capacitor.
Same as Shot 25	Aluminum 1.5-mm	3.2	N/A	N/A	Projectile barely visible until ~ 1 $\mu\text{sec}$ before strong light blackens film.	Data obscured by stray light.
Same as Shot 25	Aluminum 1.5-mm	5.4	N/A	N/A	Projectile intact until just before peak B, when obscured by luminous flux concn. material.	Luminous plasma sheath swept in by armature at ~ 8.8 mm/ $\mu\text{sec}$
Same as Shot 25	Aluminum 1.5-mm	2.5+	N/A	N/A	Projectile intact during acceleration. Moves in front of flux concentrator material.	Magnetic data erratic due to hash ground loop.
Same as Shot 25	Aluminum 1.5 mm	5+	N/A	N/A	High voltage breakdown in capacitor bank upset timing.	Shield included to eliminate light from armature plasma.
Same as Shot 25	Aluminum 1.5 mm	2.8	N/A	N/A	Inconclusive, but evidence indicates no radial motion.	Same as Shot 30

122(2)

Those of copper-coated quartz contained a 1-mm diameter pure quartz core, and outer skin of copper 0.25 mm thick. The copper was applied by vapor-depositing a fine layer on the projectile surface, and the remainder by electroplating.

## 2. Discussion of Experiments

Thirteen MGA projectile experiments were fired during this contract. Pertinent details of these appear in Table X, using MGA shot sequence numbering. Shot MGA-6 from Contract NAS8-5266 is also shown. Shots 9 through 21 were fired at the SRI test site. Shots 25 through 29 were fired at AGN.

All shots, with the exception of 6, 17 and 19, had initial magnetic field strengths in the vicinity of 40 kgauss. Shot 6 from the previous contract in this program used the flying cone cylindrical wave initiator and liquid nitrogen cooled dc magnetic coils. The initial field was 14 kgauss. Shot 17 suffered failure of one magnet coil. Its initial magnetic field was less than 20 kgauss and must have had a strong axial gradient through the armature. The value of its data is therefore questionable. In Shot 19 an arc-over occurred at the transmission line junction block, thus short-circuiting the magnet system. Its initial magnetic field was zero.

Measurement of the initial magnetic field, which had a rise time of about 1.8 msec, was accomplished with oscilloscopes and 20-msec integrators. Amplification was required of these signals, since they were taken from the small search coils. The time history of the magnetic compression was measured with oscilloscopes using 50- $\mu$ sec integrators. Direct display of the coil output voltage also gave dB/dt measurements, which could be graphically integrated to check the



electronically integrated data. These measurements also were sensitive to perturbations which might occur during the experiment. In general, there was good agreement between electronic and graphically integrated information.

In Shot 6 the flux concentrator interior and projectile flight path were open to the atmosphere. The inside of the armature, however, contained sulfur hexafluoride gas at one atmosphere pressure. This was to inhibit electrical breakdown during the magnetic compression. Shots 9 through 21 used freon for the same purpose. Shots 25 through 29 had the armature evacuated along with the flux concentrator. This considerably simplified the vacuum problem, as it was considered necessary to have the projectile in vacuum for these experiments.

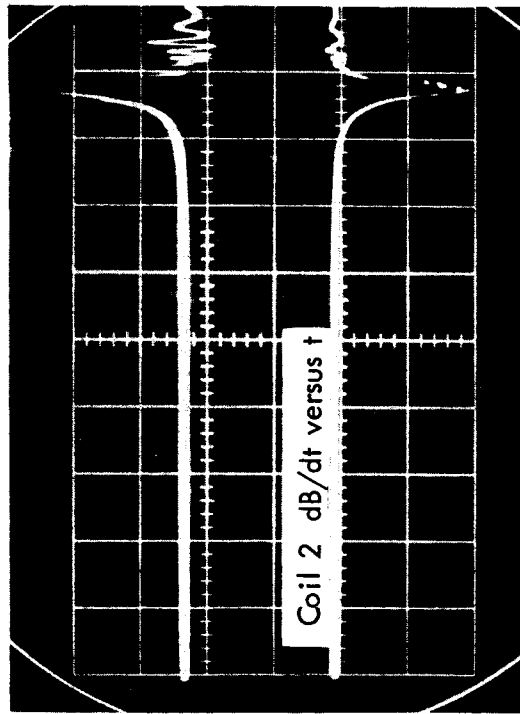
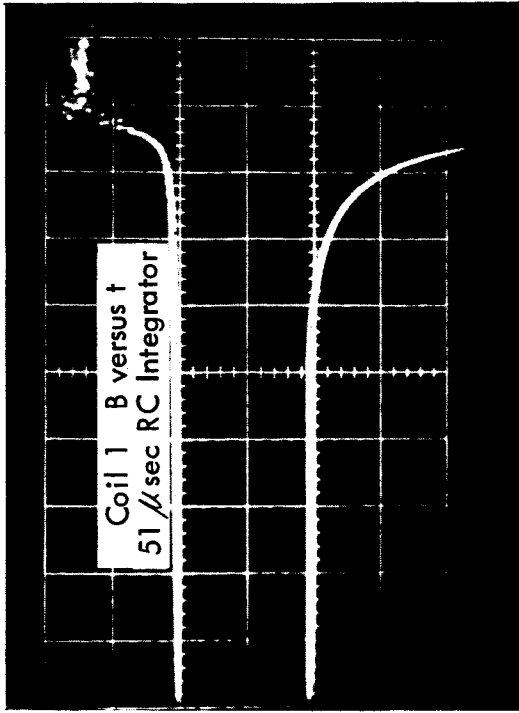
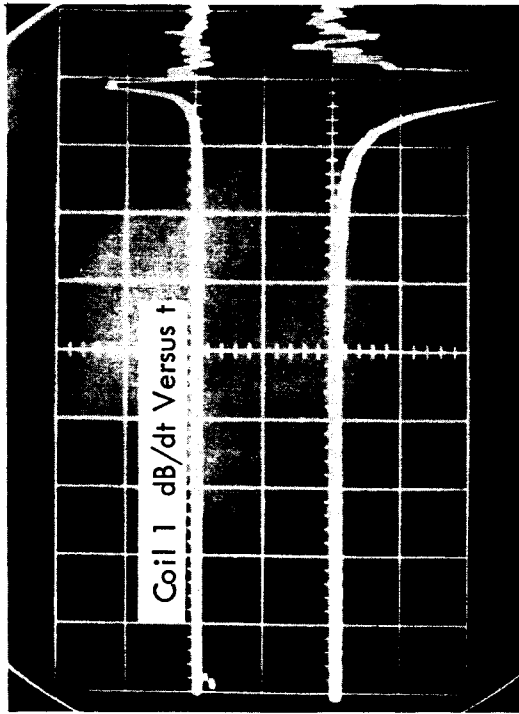
#### a. Flight Chamber Experiments

Taking the experiments chronologically, in Experiment 6 it was uncertain whether or not a solid projectile had been accelerated out of the device. Experiment 9 was essentially a repeat of Experiment 6, but with different instrumentation. The flight chamber and lucite target block provided a vacuum environment; screening of some of the gaseous material, and the capability of making quantitative measurements on shock waves induced in the target. A strong, small-radius shock would indicate the presence of a solid particle. This type of shock wave was not observed in Experiment 9.

Experiment 15 was prepared as a control to try to determine if projectile material was being magnetically accelerated. The projectile was simulated with a glass sphere so that the hydrodynamics would not be perturbed. This sphere had the same density as the aluminum projectiles. High temperature but tenuous material was observed in this

experiment but the target shock was relatively weak. Since the cloud velocity was comparable to that in Experiment 9, the cloud density must have been much lower. This would tend to indicate that Experiments 6 and 9 magnetically accelerated some projectile material. The cloud velocities in Experiments 6 and 9 also agreed well with the theoretical projectile velocities for those experiments. Experiment 15 also produced the highest peak magnetic field strength observed during the MGA program. The oscilloscope records from this shot are shown in Fig. 43.

At this point in the work, concern arose about the possibility of a high-speed shock phase velocity being generated along the tapered throat of the flux concentrator. This could be due to radial converging shock waves in the flux concentrator segments induced by armature impact at the end of the magnetic compression. It was believed that this might cause collapse of the flux concentrator before the projectile could get out, particularly if the projectile velocity was lower than had been theoretically predicted. The possibility also existed of metal jetting from the flux concentrator interior, although none had been observed. To avoid this, Shot 16 used a flux concentrator with a shortened throat. This moved the projectile closer to the outlet end of the MGA and also doubled the throat taper angle, thus reducing the velocity of any phase shock which might be generated. The cloud velocity in this shot was about half that previously observed, implying that the cloud material was coming from the inside surface of the flux concentrator, possibly from the teflon insulation. Shot 17, therefore, had the flux concentrator taper on the outside. This would definitely generate a phase velocity but the lead-epoxy end plate would inhibit the ejection of material. This shot gave low magnetic performance, but this was due to partial failure of the initial magnetic field system. The luminous cloud observed in the flight



Measurement	Signal Peak	Integrated Value	Peak Field in Flux Concentrator
Coil 1 B	2.4 Mgauss	2.4 Mgauss	7.0 Mgauss
Coil 1 dB/dt	8.8 $\frac{\text{Mgauss}}{\text{sec}}$	2.4 Mgauss	7.1 Mgauss 25.9 Mgauss/ $\mu$ sec
Coil 2 dB/dt	3.9 $\frac{\text{Mgauss}}{\text{sec}}$	1.3 Mgauss	8.1 Mgauss 24.0 Mgauss/ $\mu$ sec

The values of B from the dB/dt measurements were obtained by scaling the signals to graph paper and hand integrating.

FIGURE 43. MAGNETIC FIELD MEASUREMENTS FROM FLUX COMPRESSION EXPERIMENT

chamber was similar in appearance to that in Experiment 16, but at higher velocity. The data from Shot 17 is open to question, however.

Since no solid projectile was observed, more magnetic field strength was desired to increase the probability of the projectile being ejected from the flux concentrator before complete collapse occurred. In Shots 18 through 21 the explosive magnetic compression system was shortened to 2.5 cm to move the projectile closer to the center of the system. As can be seen from the data, however, this did not result in an increase of peak magnetic field strength. It was therefore assumed that the reduced performance was due to the sharper taper angle and not to displacement away from the system center. This implies a relatively uniform magnetic field strength throughout the armature interior.

Shots 18 and 19, with the inside taper, produced clouds similar to those previously observed. In Shot 19, however, the absence of magnetic field provided a means of checking for magnetically accelerated material in other experiments. Although the cloud in MGA-19 had the same general appearance as in 18, it caused only half the target shock strength even though its velocity was 30% higher. This result tends to substantiate the previous observation that projectile material was being magnetically accelerated. MGA-19, however, had a copper-coated quartz projectile. As will be seen, this does not correlate with target shock.

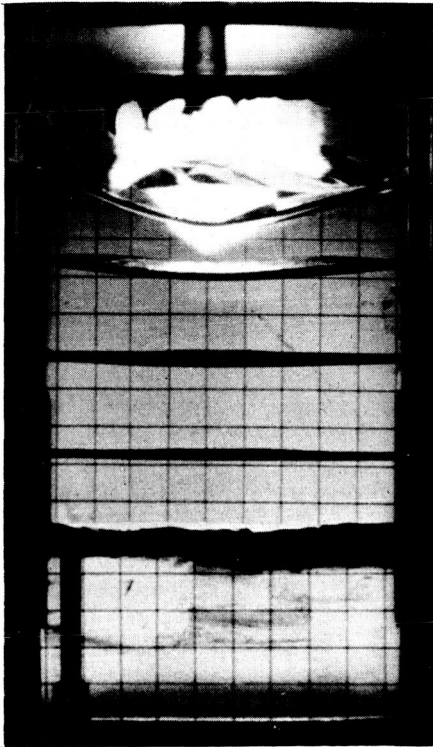
Experiments 20 and 21 essentially repeated 18 and 19 except with the outside tapered flux concentrator. The peak magnetic field strength was about the same for these two shots and Experiment 18. MGA-20 and 21 produced dark, poorly defined clouds completely unlike any previously observed, including Shot 17 (5-cm outside taper). The target shock induced by these clouds was quite low,

but the one with the copper-coated quartz projectile had twice the shock strength as the one using the aluminum projectile.

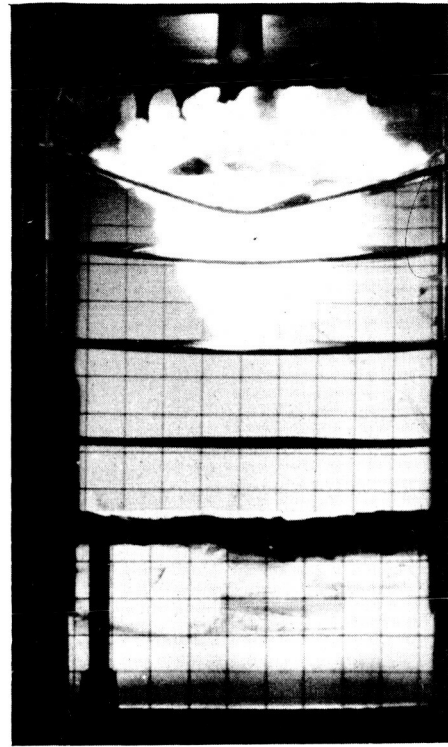
The low shock strength compared to inside taper flux concentrator shots suggests that inside taper experiments eject both projectile and flux concentrator material due to phase shocks along the taper. Phase shock generated material could not escape from MGA-20 and 21. If no significant flux concentrator material was ejected in MGA-20 and 21, then the relationship between the target shocks further substantiates the belief that at least some projectile material was being magnetically accelerated. Also, it would tend to substantiate the magnetic field diffusion and heating calculations which show only skin vaporization of the projectile. This conclusion is drawn because the copper skin of the copper-coated quartz projectile is, of course, more dense than aluminum. Since the target shock strength was twice that for the aluminum projectile, this implies a quantity of aluminum present in the cloud roughly comparable to the quantity of copper which may have been present in the cloud in Shot 21, meaning that only a thin layer of aluminum was vaporized.

These results also indicate that the remainder of the aluminum projectile and the quartz core of the copper-coated quartz projectile were slower than the vapor and were trapped. For comparison, selected frames from the framing camera sequences of Shot MGA-18 and MGA-20 are shown in Figs. 44 and 45, respectively. The cloud appearance in Fig. 44 is similar to that in Shots 15, 16, 17, 19 and 25. The broad target shock waves are also similar.

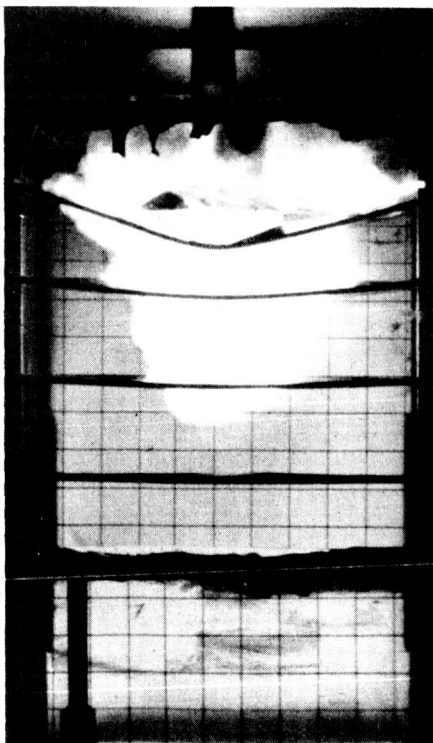
At this point in the experimental work there was still one factor that had not been positively checked. That was the possibility that some of the luminous material was coming from the annulus between the armature and flux concentrator. Shot MGA-25



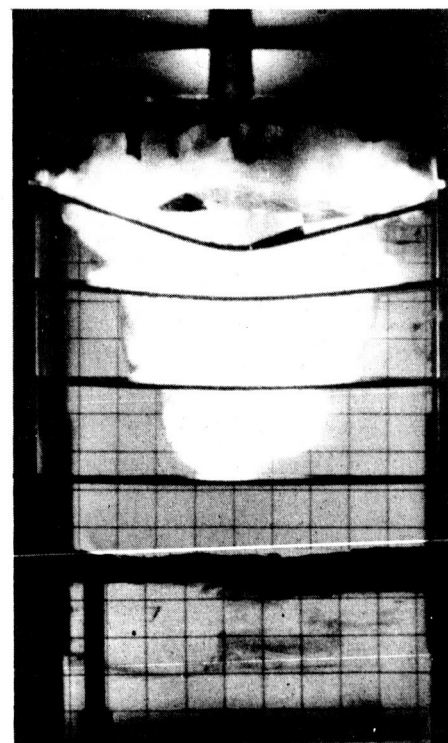
FRAME 10



FRAME 13



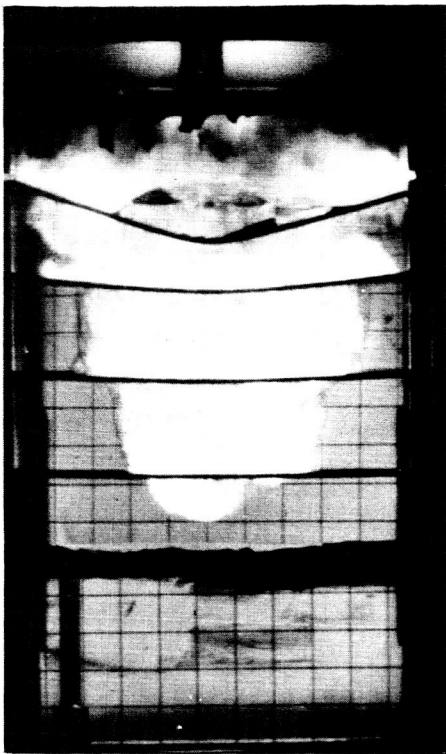
FRAME 15



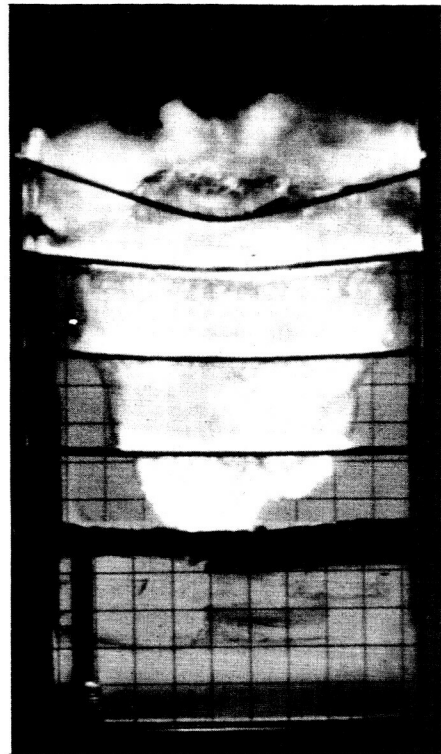
FRAME 17

FIGURE 44. SELECTED FRAMES FROM SHOT MGA-18, INTERFRAME TIME  $1\mu\text{sec}$

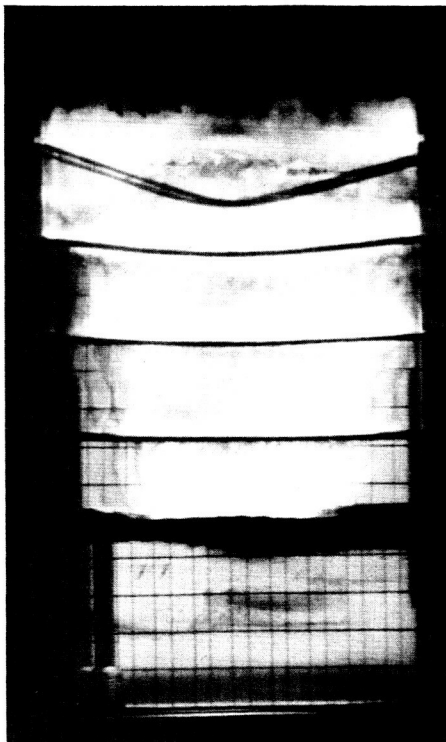
35.1-66-114



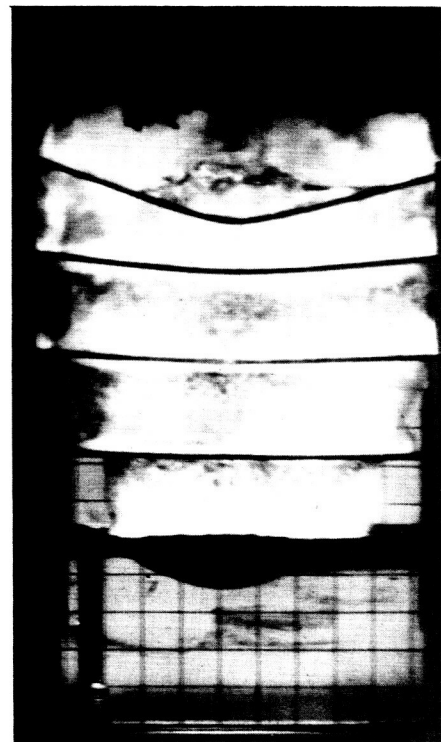
FRAME 19



FRAME 21

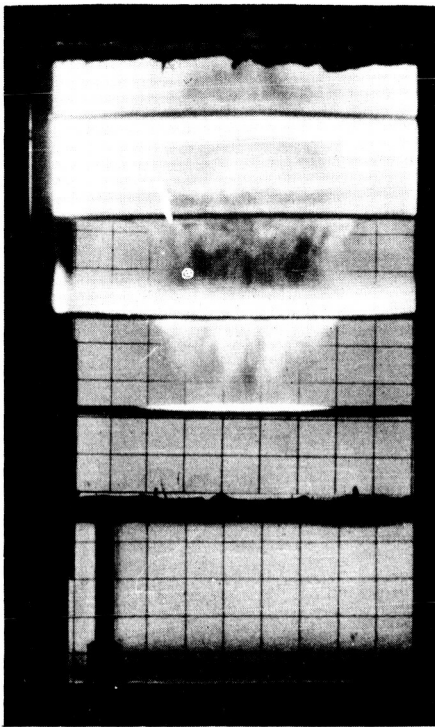


FRAME 23

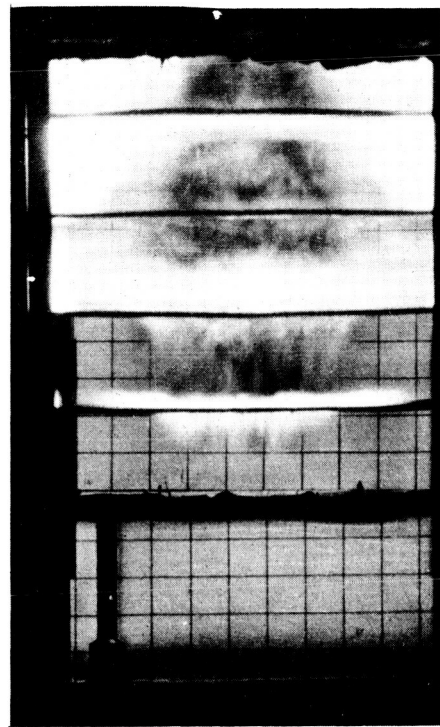


FRAME 25

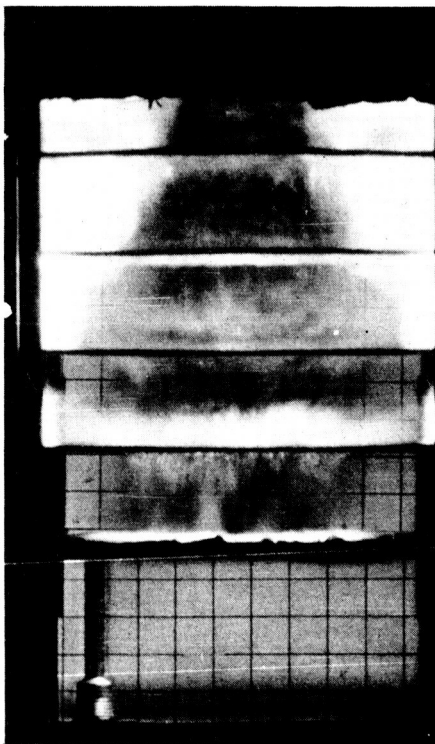
FIGURE 44. (Continued)



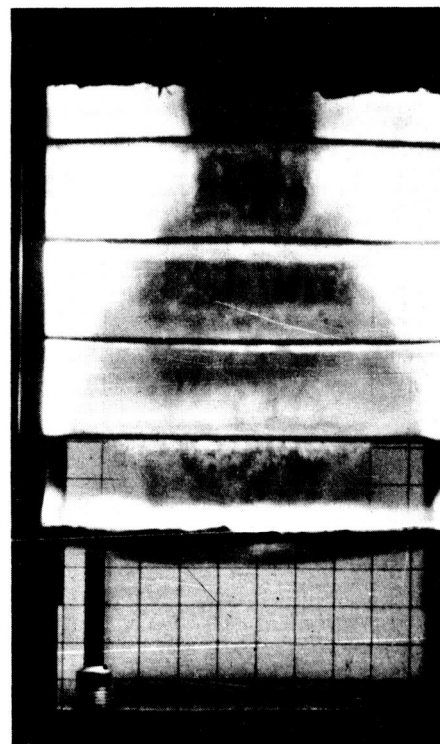
FRAME 2



FRAME 4



FRAME 6



FRAME 8

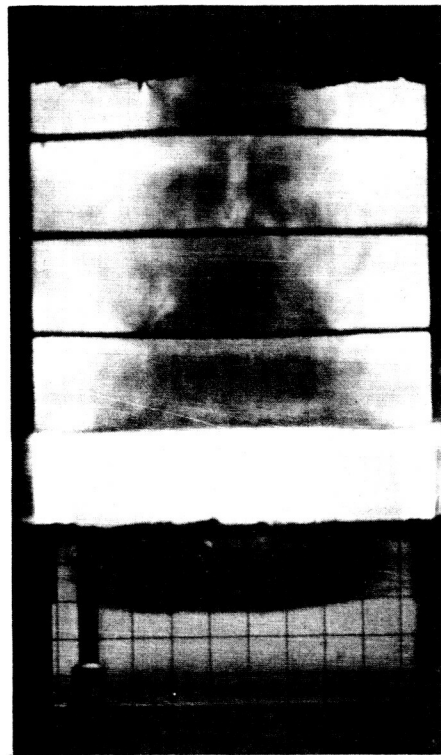
FIGURE 45. SELECTED FRAMES FROM SHOT MGA-20, INTERFRAME TIME  $1/\mu\text{sec}$

35.1-66-115

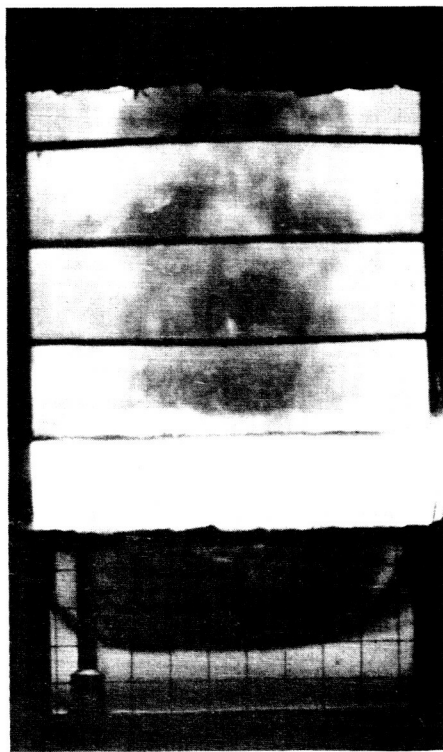




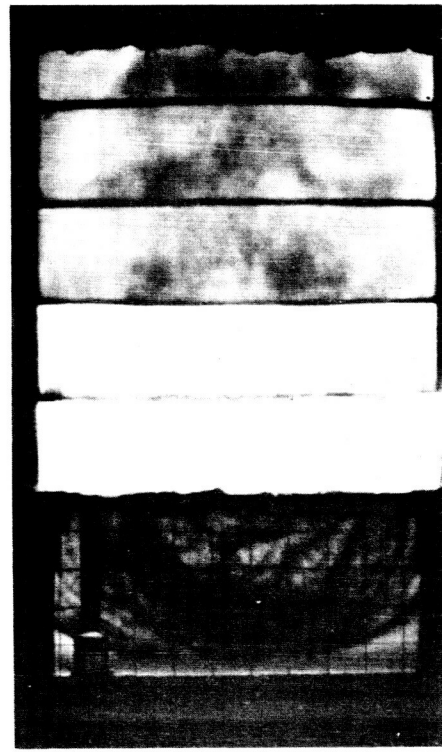
FRAME 10



FRAME 13



FRAME 16



FRAME 20

FIGURE 45. (Continued)

was fired to test for this. This experiment was essentially identical to MGA-16. The only difference was that instead of containing freon gas at 1 atm pressure, the armature was evacuated. The pressure was made low enough to avoid the formation of Paschen discharge paths. As can be seen from the table, the cloud appearance and velocity were virtually identical to that in MGA-16. This result shows that the luminous clouds were coming from within the flux concentrator throat.

b. Discussion of Internal Projectile  
Observation Experiments

The internal projectile observation experiments were conducted to try to determine what was happening to the projectile. This entailed photographing the projectile and flux concentrator throat during the magnetic compression. The optical arrangement for these experiments is described in Section V.B. The complete experimental system is illustrated in Fig. 46 (timing as in Shot MGA-29).

There were many electronic problems, particularly with timing. Since the event to be observed lasted only about 3  $\mu\text{sec}$ , a high camera framing rate was required. The interframe times used were 0.5 and 0.3  $\mu\text{sec}$  (Shots 26-28 and 29, respectively). These speeds gave data acquisition windows of 12.5 and 7.5  $\mu\text{sec}$  for the 25 frames available. This allowed for some timing error (the camera is capable of 0.2  $\mu\text{sec}$  /frame). The camera initiated the shot events, starting with the capacitor discharge that generated the initial magnetic field. The rise time of the discharge was about 1600  $\mu\text{sec}$ , thus the rotating mirror in the camera had to make 12 or 20 revolutions before the explosive was detonated. The problem of accumulated mirror speed errors was alleviated, however, by the use of a multi-revolution synchronizing gate circuit designed and built for the experiments. This device limited camera speed error to that of only one revolution. This normally was about 0.1 to 0.2  $\mu\text{sec}$ .

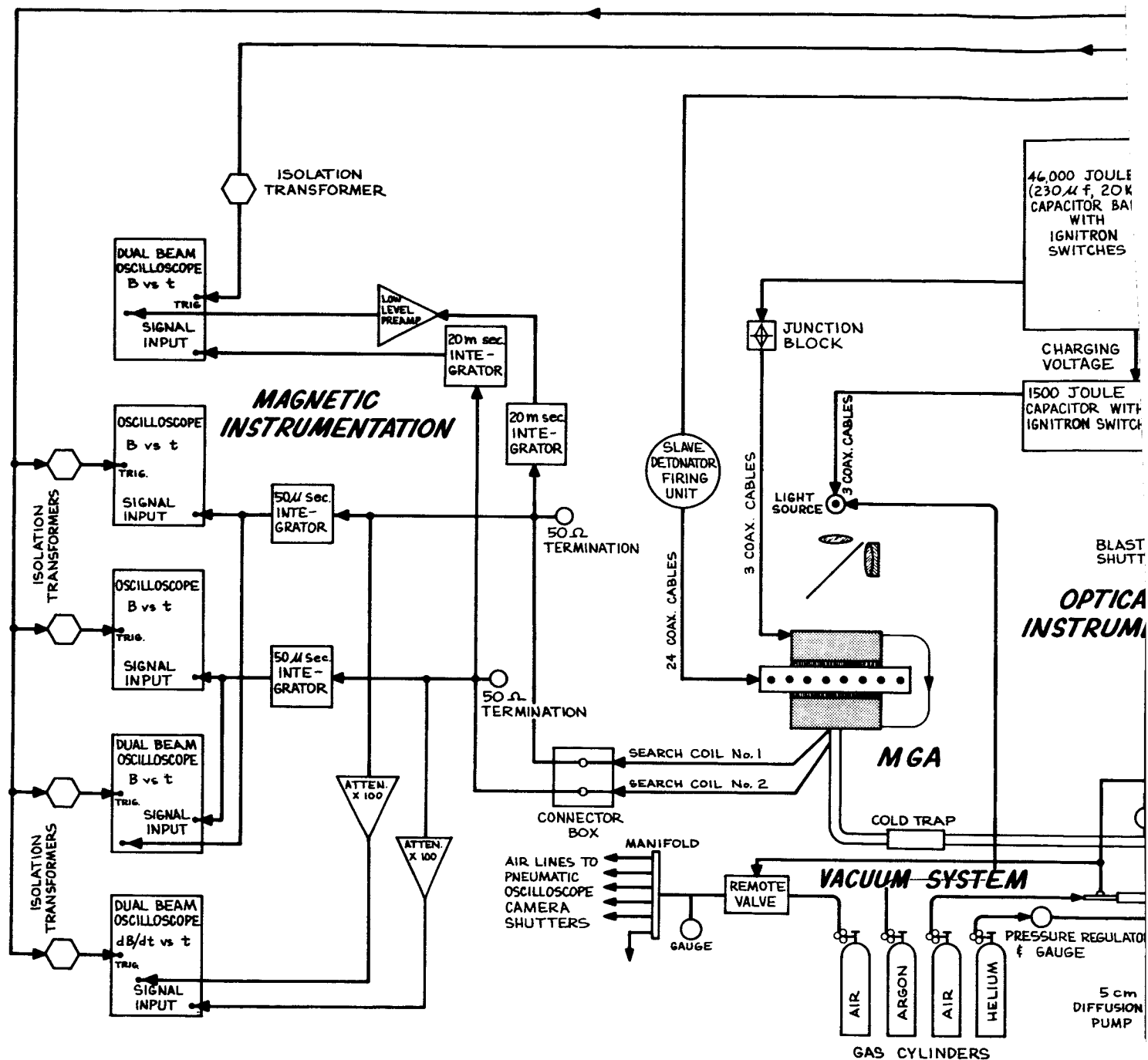
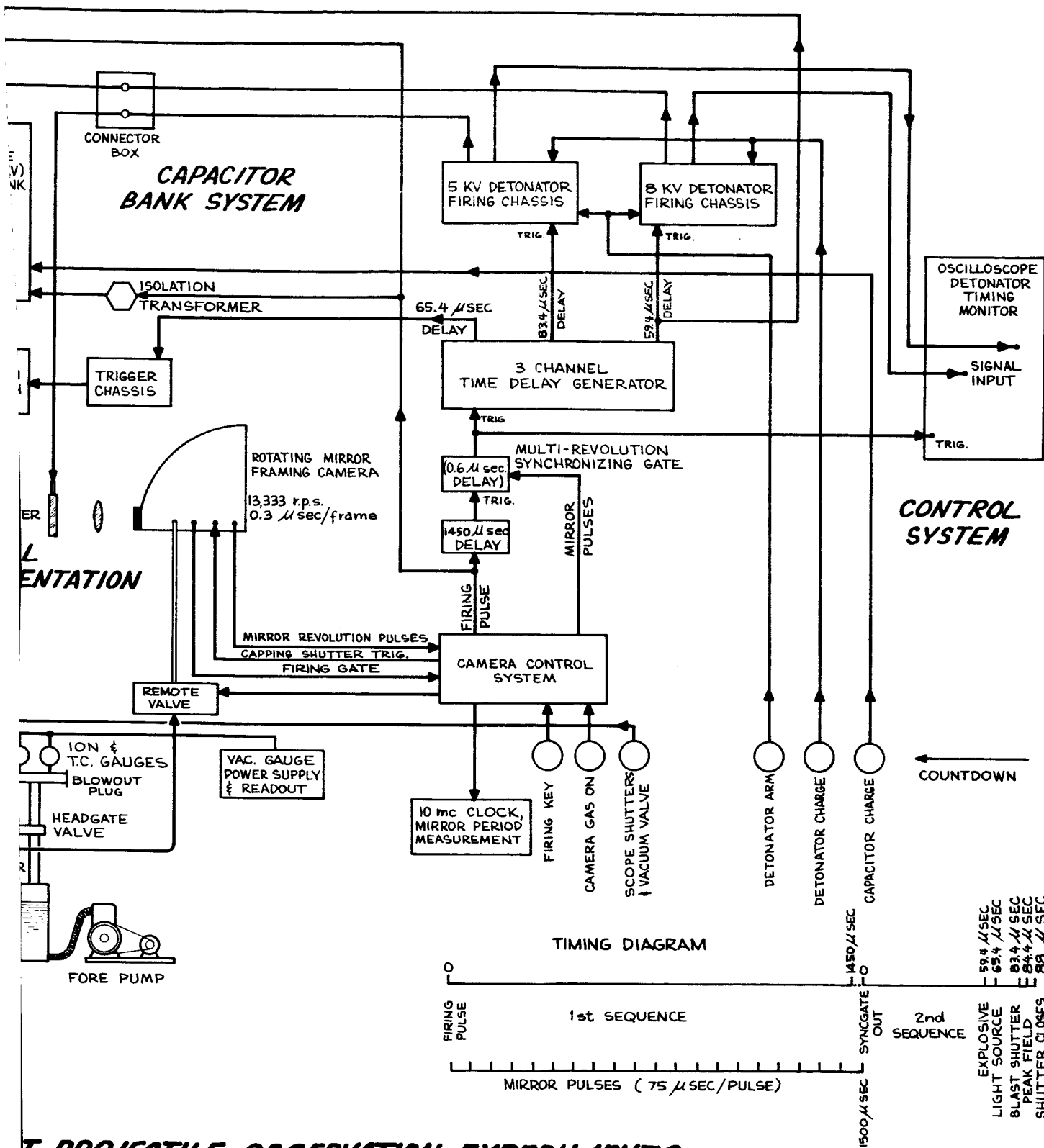


FIGURE 46. SCHEMATIC DIAGRAM OF DIRECT

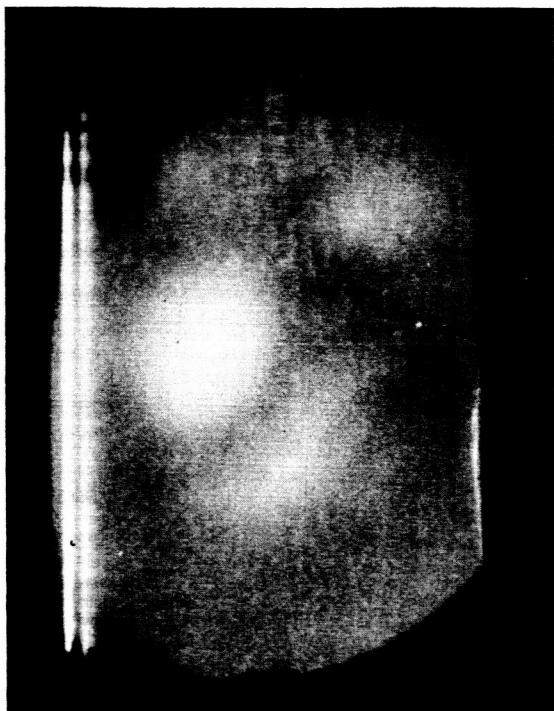


**PROJECTILE OBSERVATION EXPERIMENTS**

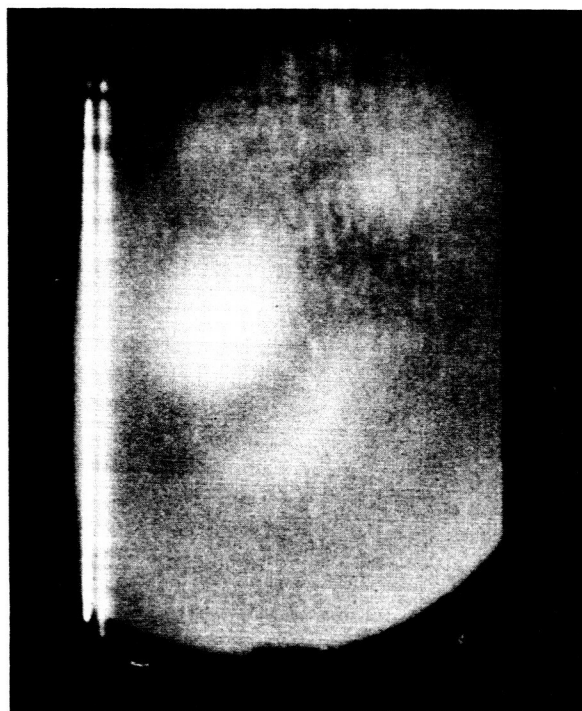


As indicated in Table X, Shots 26 and 27 had camera rewrite due to improper operation of the fast-acting shutter. Some information was obtained in Shot 27, however. It was essentially the same as Shot 28. Before discussing the results, it should be emphasized that they are but a first step to probing the interior of the MGA. Methods of screening out obscuring material have been conceived, and it should also be possible to modify the optical system to give a greater depth of field, thus putting axially displaced regions into better focus.

Figure 47 shows the framing camera photographs from Shot MGA-28 during which the field compression occurred. The poor focus was unfortunately caused by curling of the film in the camera so that it did not lie flat on the image plane. The interframe time was  $0.5 \mu\text{sec}$ . The circular object on the left is the projectile. Light areas surrounding it are reflections from the flux concentrator throat. Although it cannot be seen, the outer edge of the flux concentrator is between the arc of light (inside of flux concentrator) below and to the right of the projectile, and the lower right corner of the picture. The armature starts to collapse about frame 10. One microsecond later (frame 12) material can be clearly seen which could only be coming from the flux concentrator. Since it seems to expose the film to about the same density as the projectile, it can be assumed that it is reflecting light from the light source and is not self-luminous at that time. The quantity of this material increases, and at frame 15 shows evidence of becoming self-luminous. At frame 16 it very definitely appears self-luminous. Also, in the lower right portion of frame 15 a luminous band can be seen. This apparently was a plasma sheath within the imploding armature. On frame 16 its position can be seen to have advanced. A rough velocity measurement can be made from these two frames, which shows this luminous region



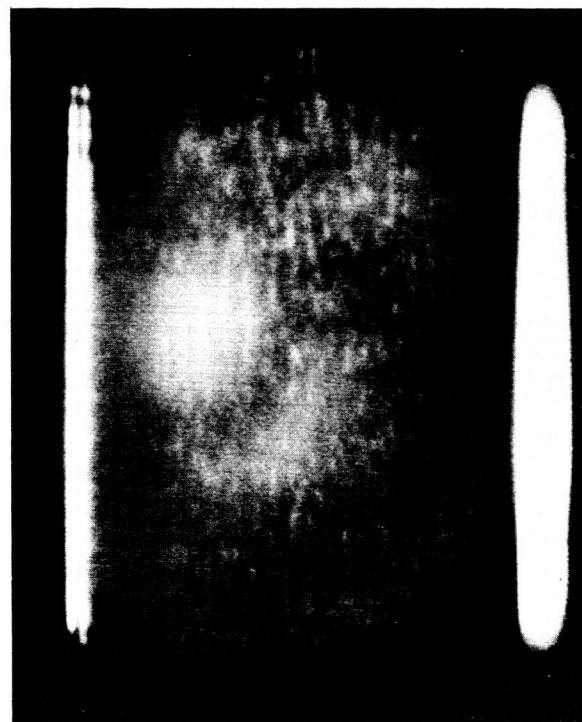
FRAME 10



FRAME 11



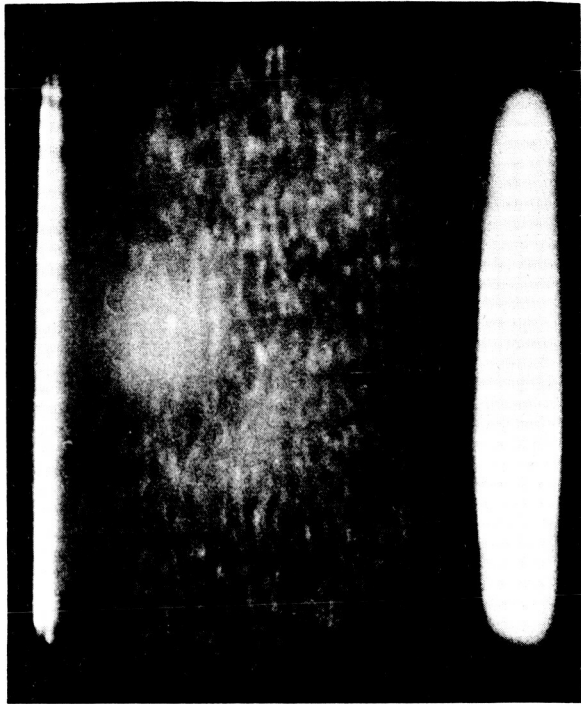
FRAME 12



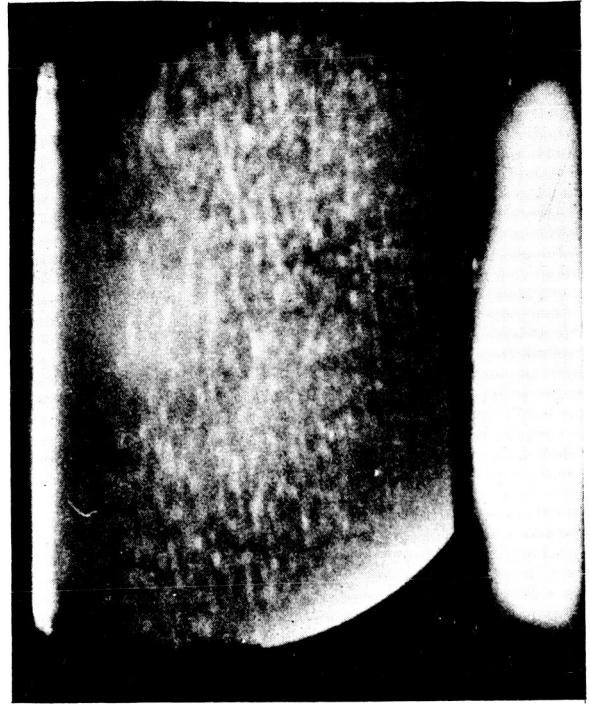
FRAME 13

FIGURE 47. SELECTED FRAMES FROM INTERNAL PROJECTILE OBSERVATION  
EXPERIMENT, MGA-28, INTERFRAME TIME  $0.5 \mu$  sec

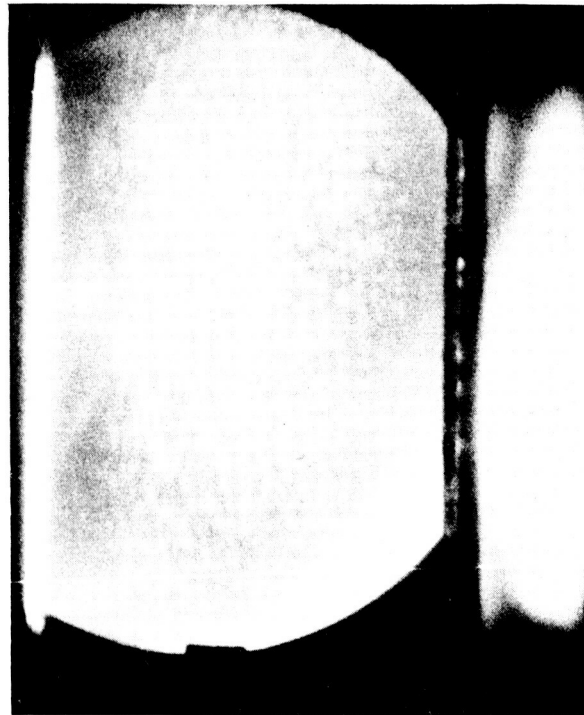
351-66-125-A



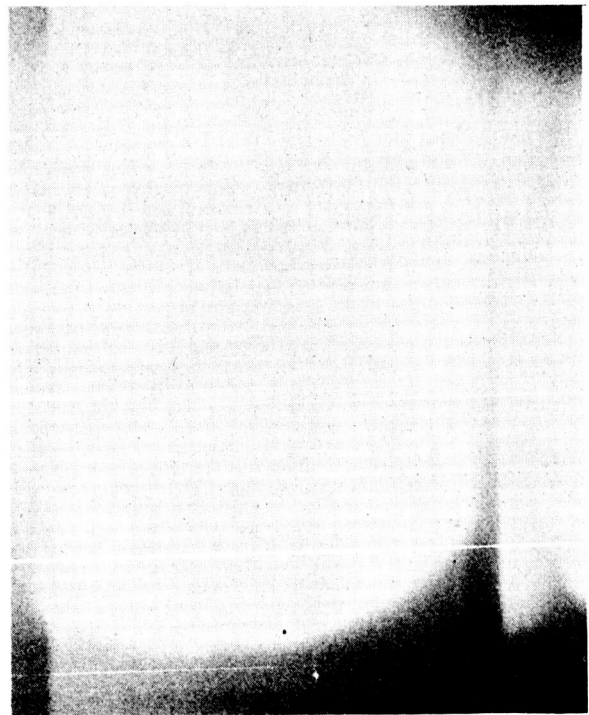
FRAME 14



FRAME 15



FRAME 16



FRAME 17

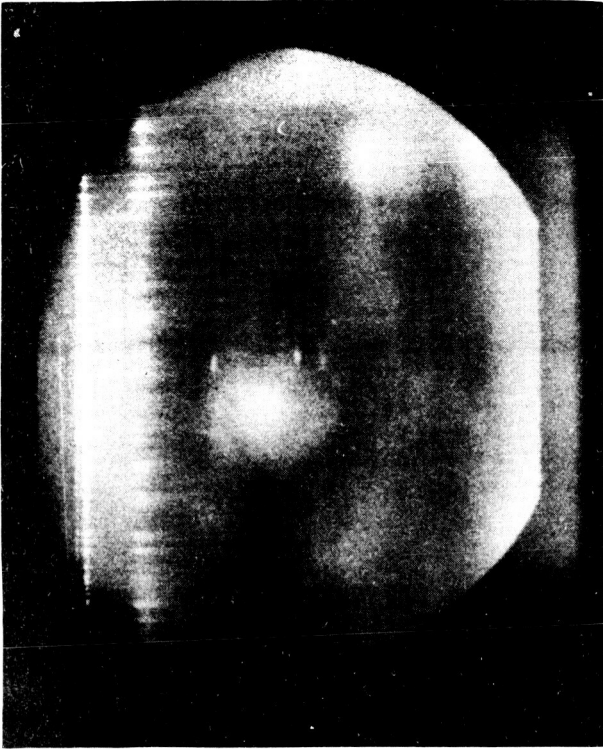
FIGURE 47. (Continued)

moving at  $8.8 \text{ mm}/\mu\text{sec}$ . This agrees well with estimates of the final armature velocity made from time-of-flight measurements done under Contract NAS8-5266. Armature contact with the flux concentrator, and thus peak magnetic field strength, occurs at or shortly after frame 16. At frame 17 the entire camera field of view is brilliantly illuminated. The intensity of this light increases during the  $1 \mu\text{sec}$  following frame 17, but at  $1.5 \mu\text{sec}$  shows decreasing intensity, returning to the frame 17 level at  $3 \mu\text{sec}$ .

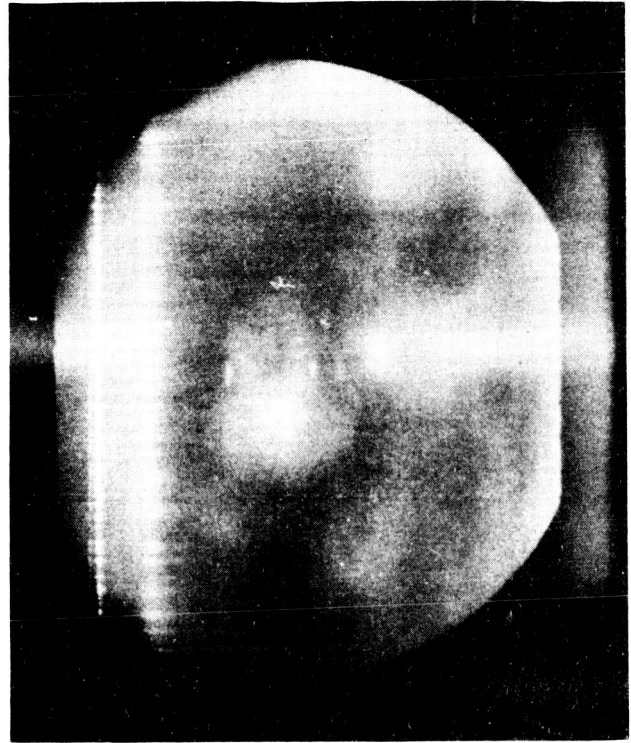
The material seen on frame 15 and later is probably the formation of the brilliant luminous cloud of material observed emerging from the MGA in the projectile flight chamber experiments. The projectile appears to be unperturbed up to frame 15, but no conclusions regarding it can be drawn after that time. At that frame the magnetic field is undergoing its most rapid increase, an event which usually takes roughly  $0.4 \mu\text{sec}$  (less than the interframe time). Thus, the greatest effects on the projectile would occur during the interval bracketed by frames 15 and 16.

Shot MGA-29, in which projectile motion was observed, used a higher camera speed. This provided better data resolution during the time centering around the peak magnetic field strength. The results are shown in Fig. 48. The armature begins to move about frame 1 (frame 3 is the first one shown). No change is observed until frame 9 ( $2.4 \mu\text{sec}$  later) when flux concentrator material begins to appear in front of the projectile. As in Shot MGA-28, the quantity of this material increases with time, but it never completely obscures the projectile (note that the exposure time per frame was half that of Shot 28 and that contrast is improved). At frame 12 ( $3.3 \mu\text{sec}$ ) the luminous armature plasma sheath is first seen, extending  $0.82 \text{ mm}$  down from the top edge of the field of view. Its position is unchanged in frame 13.

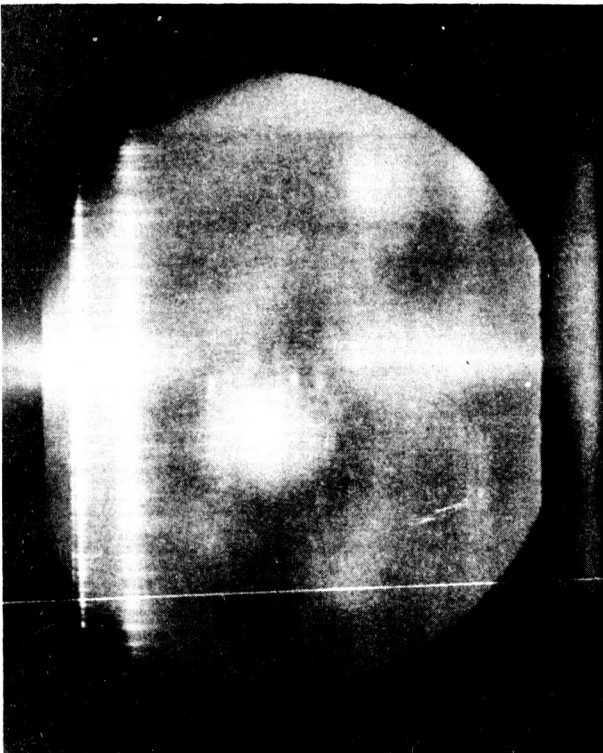




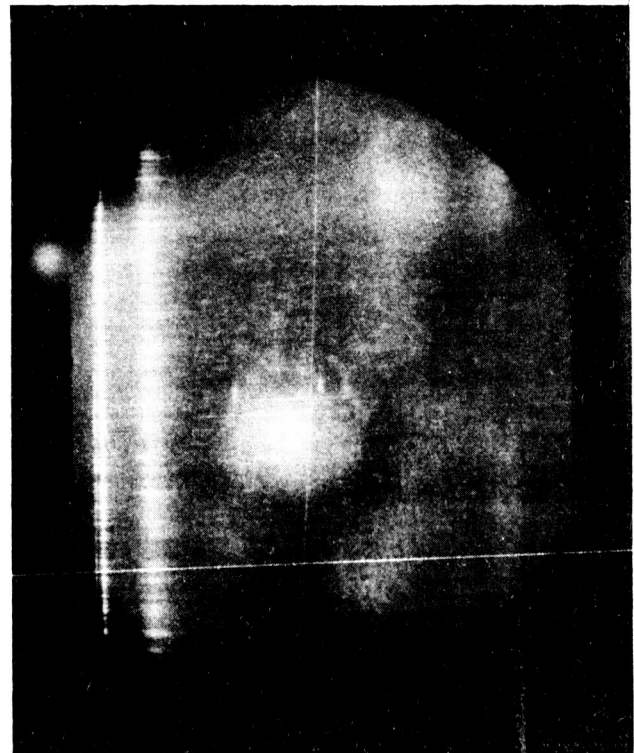
FRAME 3



FRAME 4

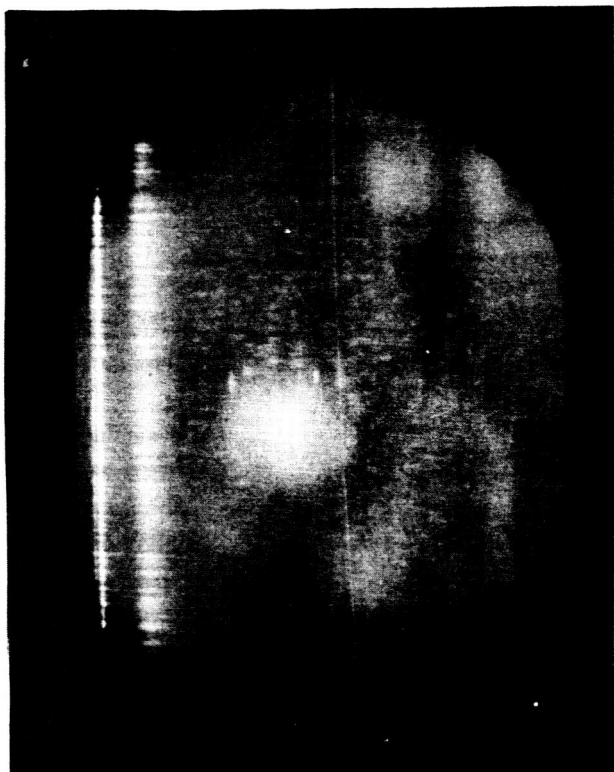


FRAME 5

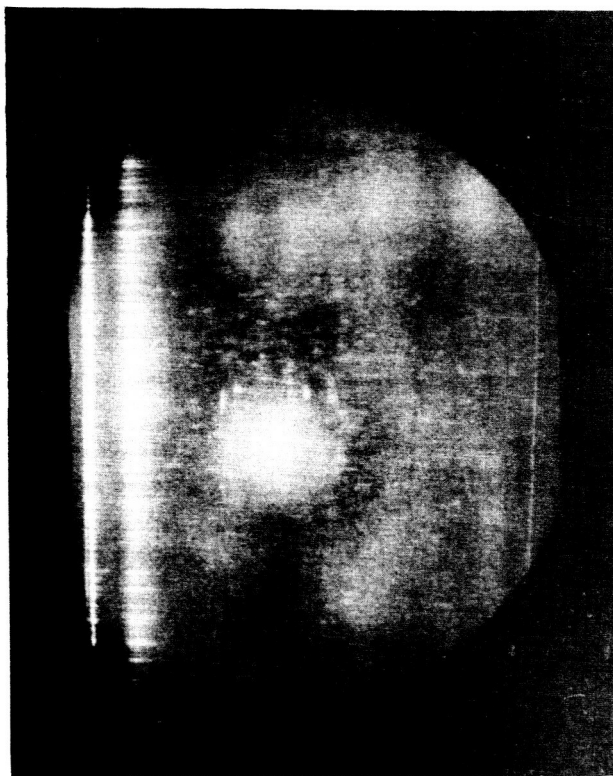


FRAME 6

FIGURE 48. FRAMING CAMERA SEQUENCE FROM SHOT MGA-29,  
INTERFRAME TIME  $0.3 \mu \text{ sec}$



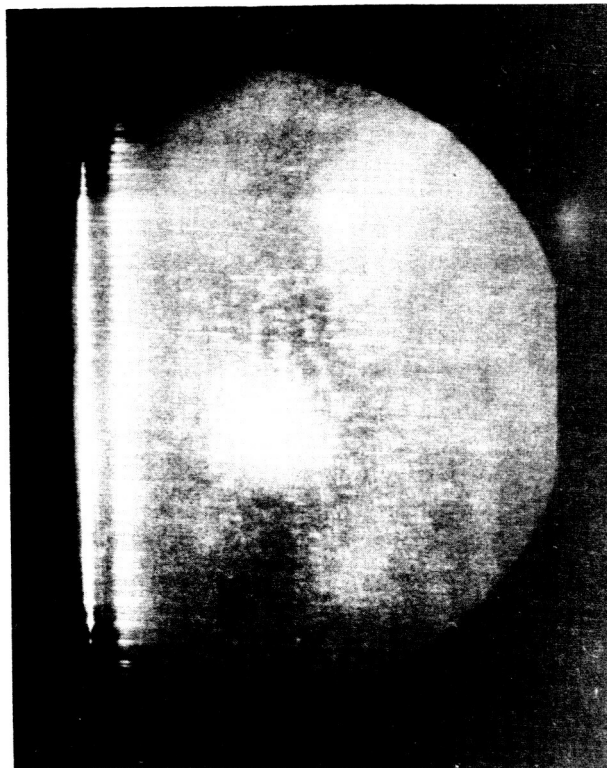
FRAME 7



FRAME 8

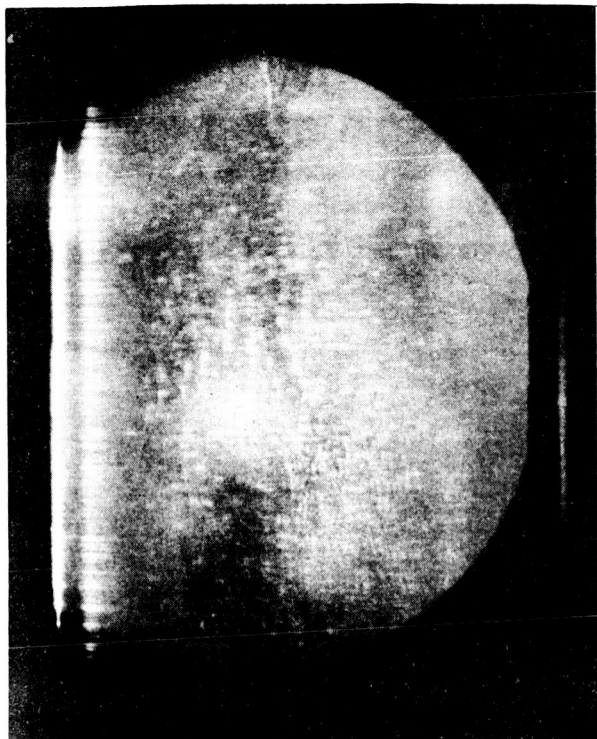


FRAME 9

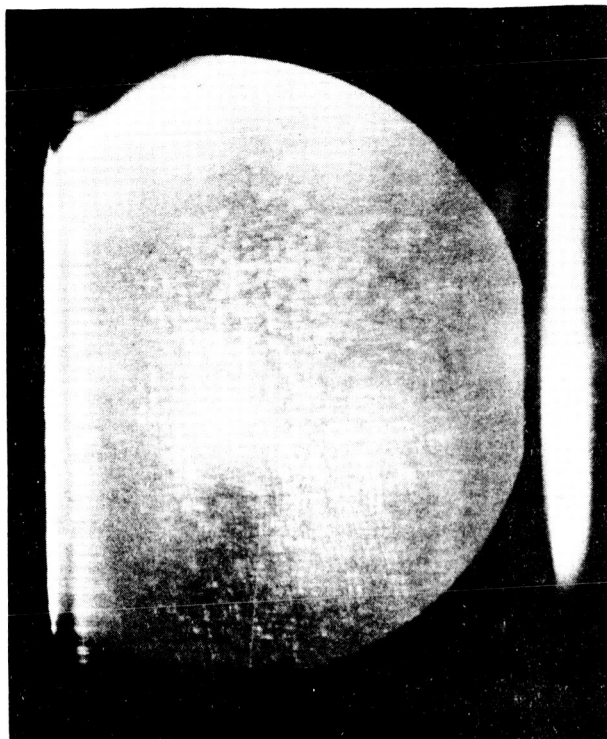


FRAME 10

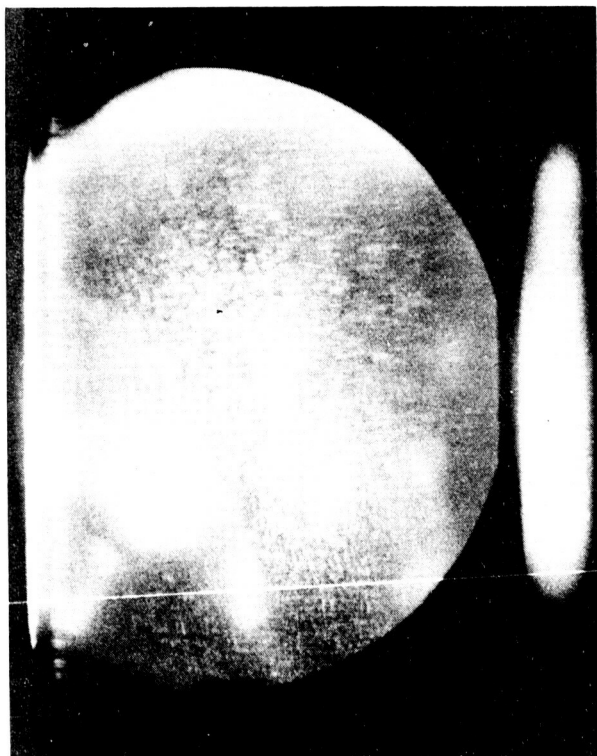
FIGURE 48. (Continued)



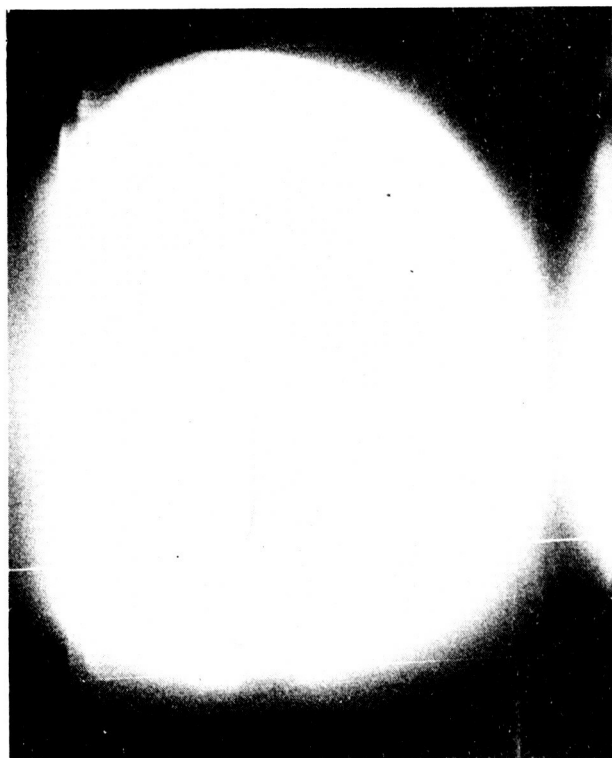
FRAME 11



FRAME 12



FRAME 13



FRAME 14

FIGURE 48. (Continued)

Thus the plasma sheath reached the flux concentrator at or before frame 12. Using the armature velocity measured in Shot MGA-28, the distance from frame edge to plasma edge in frame 12 is 31% of the distance of travel between frames 11 and 12. Since the armature would have been behind the plasma, full armature closure about the flux concentrator, and thus peak magnetic field strength, would occur at or slightly before frame 12.

In frame 13 the projectile is clearly seen to have passed through the flux concentrator material to the foreground. Measurement of the image shows it to be slightly larger, because of perspective and de-focusing, indicating axial motion. A distinct lateral displacement of the projectile occurred between frames 12 and 13. Since the optical axis was at an angle to the MGA axis, acceleration of the projectile, which should occur about frame 12, would cause a lateral shift of its image. This angle is not accurately known, but must have been between  $3^{\circ}$  and  $5^{\circ}$ . The outlet tube geometry would not permit an angle greater than  $10^{\circ}$ . The actual lateral displacement of the projectile could not be determined with precision in this experiment. Lateral movement of an object not in the focal plane of this highly critical optical system would be exaggerated on the film because of non-linearity.

If the assumption is made that the actual shift was half that on the film, the lateral position would have changed about 0.5 mm. A  $5^{\circ}$  angle between optical and MGA axes is considered conservative. Using these numbers, the axial projectile motion would be  $0.5/\sin 5^{\circ}$ , or 5.8 mm (60% of the distance to the end of the flux concentrator). At  $0.3 \mu\text{sec/frame}$ , the velocity would be 19 km/sec. This velocity is high, but is consistent with the magnetic field strength which is estimated to exist between the projectile and the flux concentrator surface. This field could be greater than the normalized small hole field by as much as a factor of 3 since the projectile itself excludes

flux lines, thus increasing the flux density between it and the flux concentrator. In addition, peak rates of rise as high as 26 Mgauss/ $\mu$ sec have been measured in that region without the projectile present.

In frame 13, the projectile is apparently luminous, indicating surface vaporization. This could have started around frame 12 which appears to show some increase in projectile brightness over frame 11. At frame 14, the field of view is filled with luminous material. It is significant that this occurs 0.6  $\mu$ sec after peak field strength is reached. A fraction of this luminosity must be due to axial jetting of the armature plasma, and some certainly comes from the projectile. However, its sudden appearance in frame 14, equally covering the entire field of view, strongly suggests that it was formed by shock wave arrival at the inner flux concentrator surface due to armature impact on the outer surface. Shocking of the teflon tape insulation or of the thin layer of air trapped under the tape could generate this light.

The analysis of the results of Shot MGA-29 is based on the assumption that the projectile moved along the axis of the MGA system. This is reasonable because the flux concentrator throat shape creates a magnetic cusp of revolution with a minimum field path co-linear with the MGA axis. To test this assumption experimentally, Shots MGA-30 and MGA-31 were built identically to MGA-29, except that the axis of the optical instrumentation was adjusted to be co-linear with the MGA axis. Thus, pure axial motion would not result in lateral shifting of the image on the film. Any radial motion would be detected.

Unfortunately, no clearly defined results were obtained from these experiments. Shot MGA-30 suffered a high voltage breakdown in the capacitor bank which upset, by a few microseconds, the synchronization of the explosive firing with the camera. This was sufficient to prevent photography of the projectile during the occurrence

of peak magnetic field strength. More than 5 Mgauss were generated, however.

Shot MGA-31, which generated 2.8 Mgauss, had inconclusive optical data. The still pictures of the projectile taken before the shot was fired showed a good quality image. Inexplicably, the image was smeared out in the framing camera sequence during the experiment. The luminous flux concentrator material can be seen, and the brilliant light, which comes on after the peak field strength is reached, expands and contracts in the same oscillatory manner as in the other projectile observation experiments. Instead of the round projectile, however, there is just a smear of light, which is identical on all frames up to the time the brilliant light appears. The only correlation that can be made is that the center of the light smear is in the same position as the center of the projectile image in the still picture.

If the smear is the projectile image, however, the results of Shot MGA-29 are confirmed because no radial motion can be observed. It is quite possible that the experiment was accidentally jarred between the time the stills were taken and the shot was fired. This could have knocked the optics out of focus and caused the projectile to appear the way it did. This result must properly be considered inconclusive, however, pending future verification.

#### c. Conclusions

Although the flight chamber tests did not conclusively demonstrate that a solid projectile was accelerated out of the MGA, they did show that projectile surface material is being ejected. They also indicate that flux concentrator material is coming out of the device. With the exception of Shot 16, all the metallic projectile flight chamber experiments in which both peak magnetic field and gas cloud velocity data were recorded (MGA-6, 9, 16, 17, 18 and 20) had luminous

cloud velocities equal to or greater than the theoretical projectile velocities for those experiments. Shot 16 showed lower velocity than theoretical; however, it is the only shot in which rapid loss of cloud luminosity was observed, indicating some possible anomaly in the experiment. Shot 15, with no metal projectile (glass), and Shot 19, with zero magnetic field, had almost identical cloud velocities (9.4 and 9.5 km/sec). That velocity is much lower than theoretical for magnetic acceleration of metal in Shot 15. This result substantiates the previously discussed flight chamber data, which indicates that magnetic gradient acceleration of projectile material does take place.

The direct observation experiments showed the projectile during acceleration. The technique can be used for further study of the MGA interior, and data quality can be improved. The projectile was observed to be intact and moving after the peak magnetic field strength (maximum heating and acceleration) occurred. No accurate measurement of projectile velocity can be made from its lateral displacement. However, the data indicate that the velocity was in the range of a few tens of km/sec. It appears that a major fraction of the luminous cloud is due to shock breakout of the inner flux concentrator surface. This shock would be quite intense because of the high armature impact velocity ( $\sim 9$  km/sec) on the flux concentrator. The shock phase velocity along the flux concentrator's taper is of the order of 30 km/sec. Thus, it is possible that projectiles have been trapped by jetting material or flux concentrator collapse, even though gas escaped from the MGA.

## VII. CONCLUSION

The work reported here strongly indicates potential feasibility of the magnetic gradient accelerator. It has been shown experimentally that projectile surface material has been accelerated to velocities corresponding to the theoretical projectile velocities. No discrete projectile was observed to come out of the MGA, but it is possible that cloud-induced shock waves in the lucite flight chamber targets obscured shocks from projectile impact.

The magnetic field diffusion calculations show that only the projectile surface should be vaporized. If the increase in projectile brilliance in frames 16 of Shot 28 and 13 of Shot 29 is surface vaporization, the theory would have experimental verification since the computations predict vaporization at about that time. The projectile flight chamber experiments do give evidence which supports the surface vaporization theory.

Based on experimental observations, it is quite probable that the projectile remains intact after the peak magnetic field strength, which is also after armature contact with the flux concentrator. The projectile becomes obscured at this time, and subsequent events cannot be seen. It appears to move at high velocity, but it may be trapped by the imploding system.

It is recommended that this program be carried on to determine what happens to the projectile. A technique now exists for examining the projectile and flux concentrator. Methods have been conceived which should permit longer viewing of the projectile, and it should be possible



to reduce shock breakout effects inside the flux concentrator. Further investigation along these lines could point the way to remedial action which would result in a useful meteoroid simulation tool.